

Multiscale modelling of de Vries type ferroelectric
liquid crystals

Jonathan H Murray

Department of Mathematics & Statistics

University of Strathclyde

Glasgow, UK

2011

This thesis is submitted to the University of Strathclyde for the
degree of Doctor of Philosophy in the Faculty of Science.

The copyright of this thesis belongs to the author under the terms of the United Kingdom Copyright Acts as qualified by University of Strathclyde Regulation 3.50. Due acknowledgement must always be made of the use of any material in, or derived from, this thesis.

Acknowledgements

I would like to thank my supervisor, Professor Nigel Mottram, for all of his help throughout the course of the research. I would also like to thank Professor Mikhail Osipov for the discussions which helped guide me on this subject.

I must also thank Dr Maxim Gorkunov for his helpful discussions, and Dr Matthew Neilson for his constant support.

Many thanks to EPSRC and Dow Corning for funding through a CASE award.

Finally, I am indebted to my family and friends for their continued support and encouragement throughout my PhD.

Abstract

In this thesis, we have modelled de Vries type ferroelectric liquid crystals at various length-scales and various degrees of complexity, hoping to map physical molecular properties to the existence and optical characteristics of various states of the liquid crystals. At the smallest length-scale we considered interaction potentials that account for short and long range forces between two rod-like molecules. Using Fourier decomposition we found that the simplified Maier-Saupe pair potential, which depends only on the relative molecular orientation, was capable of approximating these potentials.

At the mesoscopic level the free energy was then calculated using the Maier-Saupe pair potential and a mean-field approach was taken. The phase behaviour of the system is then described by two order parameters, representing tilt and biaxiality, from which the optical axis and birefringence can be calculated.

Next we used a simple phenomenological model to model the phase transition of smectic A to smectic C at the macroscopic scale. We were able to calculate the optic axis and birefringence of the model as a function of temperature and applied electric field. These optical quantities were then fitted to the corresponding functions calculated using the Maier-Saupe free energy.

Finally, using this phenomenological model, we examined the switching characteristics of a de Vries material whilst varying molecular parameters. We solved the dynamic equations using a simple numerical method and employed an adaptive time-stepping algorithm. The results were visualised using standard τV curves, which display regions of switching for various applied voltages and pulse lengths.

In this way we have managed to link across length scales allowing us to alter the molecular properties of our molecules and examine the effect on the physical observables, the optic axis and birefringence, of the bulk material. Such an approach could be used to optimise device performance by tailoring molecular parameters.

Contents

1	Introduction	1
1.1	History	1
1.2	Types of liquid crystal	2
1.2.1	The nematic phase	3
1.2.2	The smectic phases	4
1.3	Chirality effects	5
1.4	de Vries type smectics	8
1.5	Outline of thesis	12
2	Modelling intermolecular interactions	13
2.1	Introduction to molecular potentials	13
2.1.1	Gay-Berne potential	19
2.1.2	Electrostatic dipole-dipole interaction	22
2.1.3	Further investigation of the Gay-Berne and dipole-dipole interaction potentials	24

2.2	An analytic form of the averaged Gay-Berne and dipole-dipole potentials	31
2.2.1	Fourier Analysis	33
2.2.2	A glimpse at the Maier-Saupe interaction potential	38
2.3	Summary	43
3	The Maier-Saupe approach	45
3.1	Introduction to the mean-field theory	45
3.1.1	The intermolecular interaction potential	45
3.1.2	The mean-field approximation and the free energy	47
3.2	Construction of a mean-field model for de Vries Sm C	49
3.2.1	Calculating the Maier-Saupe pair potential	50
3.2.2	Analysis of U_{MS}	52
3.2.3	Mean-field interaction potential U_{MF} without an external electric field	54
3.2.4	Model with external electric field	57
3.3	Free energy	58
3.3.1	Approximating the mean-field free energy	58

3.3.2	Analysis of approximated free energy	61
3.4	Phase diagrams with order parameters	65
3.4.1	Optic axis and Birefringence	71
3.5	Investigation of molecular model parameters	71
3.6	Summary	76
4	Phenomenological model for switching in de Vries FLCs	77
4.1	Landau-de Gennes Theory	77
4.2	Free Energy	78
4.2.1	The thermotropic terms	78
4.2.2	Analysis of the thermodynamic terms	80
4.2.3	The dielectric terms	83
4.2.4	The thermotropic and dielectric free energy	85
4.2.5	Analysis of the energy including the thermodynamic and polar components	88
4.3	Fitting the model parameters	90
4.3.1	Systematic method	92

4.3.2	Brute force method	100
4.3.3	Investigation of molecular model parameters	103
4.4	Dynamic analysis of a liquid crystal cell switching	105
4.4.1	Forward Euler time discretisation	107
4.4.2	Adaptive time	108
4.4.3	Rotational viscosity	112
4.4.4	τV -plot generation	116
4.5	Summary	118
5	Conclusions	120
A	Calculating the Maier-Saupe pair potential	124

1 Introduction

1.1 History

The commonly known states of matter are solid, liquid and gas. The degree to which the molecules are packed differs greatly across the temperature range. In the solid crystal state the molecules are closely packed together in rigid patterns. In the liquid and gas states the molecules are mobile and diffuse, differing in the degree to which the molecules are spread, see Figure 1.1. The random distribution of molecules in the gas and liquid states is described as being isotropic, no matter the viewing angle the molecules' orientation with respect to one another looks the same. It is at the transition from liquid to solid that the molecular structure gains a great deal of order. This ordering breaks the isotropy and we say that the solid is anisotropic, the molecular orientation and translational order will now differ depending on the viewing angle.

A fourth state of matter was first discovered in 1888 by Reinitzer and Lehman.

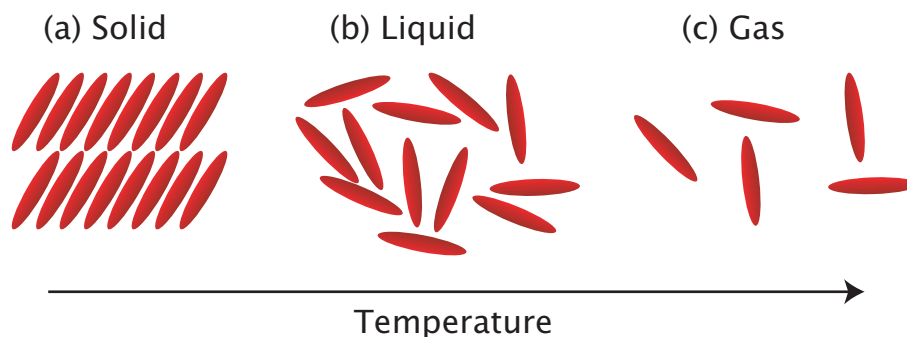


Figure 1.1: The commonly known states of matter: (a) crystalline solid, (b) isotropic liquid, (c) isotropic gas. The degree of order, positional and orientational, decreases as temperature increases.

On heating a cholesterol related substance Reinitzer observed what appeared to be two melting points that resulted in first a cloudy liquid and then a clear liquid [1]. It was the further analysis and experimental design of Lehman that confirmed the discovery [2]. The cloudy liquid stage was later named the liquid crystal state as the molecules had the ability to flow whilst maintaining some order.

1.2 Types of liquid crystal

Within the liquid crystal state there are many mesophases, meaning phases between the solid crystal and the isotropic liquid phase, which are thermodynamically stable, see Figure 1.2. It is from the anisotropic structure of the molecules that these mesophases are possible, hence we name the liquid crystal molecules ‘mesogenic’. Liquid crystals can be induced in two ways given the mesogens, thermotropically and lyotropically. Thermotropic liquid crystals are pure or mixed compounds of mesogenic molecules where any existing mesophases are temperature

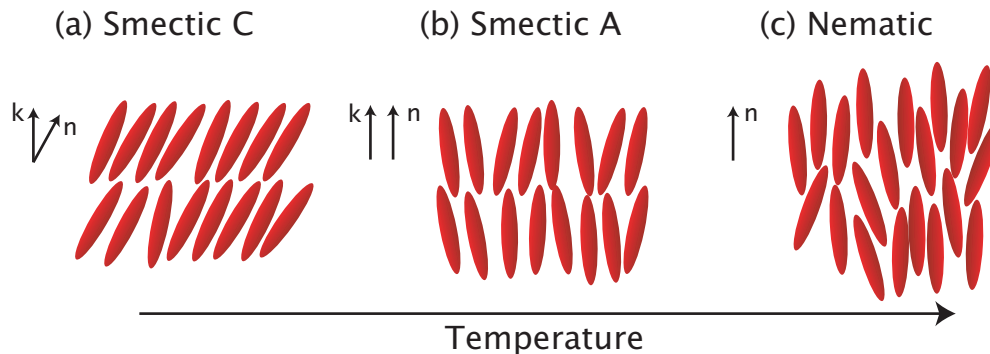


Figure 1.2: The (a) smectic C, (b) smectic A, and (c) nematic liquid crystal phases. The degree of order, positional and orientational decreases as temperature increases, here \mathbf{k} and \mathbf{n} are the unit vectors of the smectic layer normal and director respectively.

dependent. Lyotropic liquid crystals are created by mixing mesogenic molecules with a nonmesogenic solvent, hence the concentration of mesogens as well as the temperature is a factor in the creation of a mesophase. In this thesis we only concern ourselves with a few smectic and nematic thermotropic mesophases formed with rodlike molecules.

When we talk about these mesophases we invariably discuss the order that exists. When the rod-like molecules are packed together the long-axis of the molecules have an average direction named the director, a unit vector \mathbf{n} . The two types of order are positional and orientational which we describe in terms of the director. Orientational order describes to what degree all the molecules align with the director. Positional order describes whether the translational symmetry of the director is short or long range, see Figure 1.2. For example, an isotropic liquid of rod-like molecules would have no average direction for the director, the molecules would be pointed in every direction with a uniform distribution of centres of mass, hence the lack of orientational or translational order.

1.2.1 The nematic phase

The least ordered mesophase we consider is the nematic phase where only orientational order is present. The molecules are fully rotationally symmetric around the director with no translational order, creating a uniaxial phase. A measure of the orientational order present in the nematic phase is given by the order parameter S ,

$$S = \int \left(\frac{3}{2} \cos^2(\theta) - \frac{1}{2} \right) f(\theta) d\theta = \left\langle \frac{3}{2} \cos^2(\theta) - \frac{1}{2} \right\rangle,$$

where $f(\theta)$ is the distribution of molecules with tilt angle θ about the director \mathbf{n} . When the molecules are perfectly aligned with the director $S = 1$ and when the molecules are isotropically, i.e. not, aligned $S = 0$. So when the temperature of the liquid crystal is decreased the orientational order increases and S increases.

1.2.2 The smectic phases

The smectic phases break the full translational symmetry that is present in the nematic and isotropic states. The translational order is realised in the formation of layers with constant layer thickness. In each layer the orientational order is long range. The least ordered smectic phase, called the smectic A phase, is basically a layered nematic, the director of each layer is parallel with the layer normal, \mathbf{k} . Ordinary smectic A materials are uniaxial because of the full rotational symmetry about the director \mathbf{n} and the layer normal \mathbf{k} . The order parameter S will then be dependent on the temperature and number density of molecules in the layer.

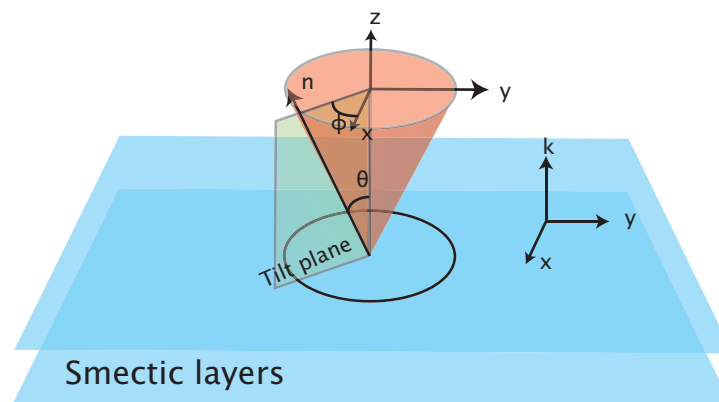


Figure 1.3: The cone of Sm C. Director \mathbf{n} depends on the azimuthal angle ϕ and the cone tilt angle θ around the smectic cone. The tilt plane contains the director vector and the smectic layer normal \mathbf{k} , parallel with z in the layer frame.

The smectic C phase breaks the rotational symmetry of the smectic A phase when the director differs from the smectic layer normal. The plane containing the director and layer normal is named the tilt plane, see Figure 1.3. When viewing the director from within the tilt plane it appears aligned with the layer normal, but when viewed above the tilt plane we can see that the director is tilted away from the layer normal. Hence, the director is biaxial. The tilt angle is stable for a given temperature and density, but the azimuthal angle, the tilt direction, is independent of energy. A suitable order parameter for the smectic C to smectic A transition would be dependent on the tilt angle, θ , of the director to the layer normal.

1.3 Chirality effects

When a molecule loses mirror symmetry it is said to be chiral. Chiral phases can be found for all of the liquid crystal phases discussed above. A consequence of chirality is the formation of left or right handed helical structures, see Figure 1.4. In smectic C* (chirality is denoted by an asterix,*) the tilt direction of each layer follows a helical path around the layer normal. Another consequence of chirality

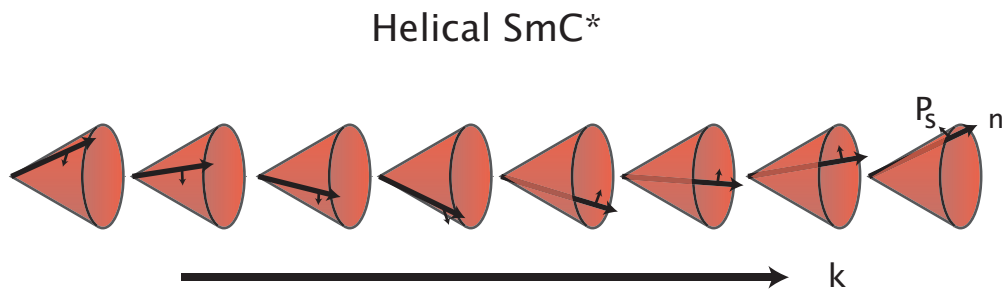


Figure 1.4: Director \mathbf{n} moves around cone as we progress in the direction of \mathbf{k} , the layer normal. The spontaneous polarization P_s averages to zero over one period.

is the existence of a spontaneous electrical polarization perpendicular to the tilt plane of the smectic cone [3]. Therefore each layer has a spontaneous polarization but the helical structure of the layers denies any macroscopic polarization.

The presence of a spontaneous polarization linked to the tilt of each smectic layer means that the molecular orientation of the material can be forced into a configuration of our choosing by applying an electric field. By varying the polarity and direction of the applied field the layers can be made to orient how we wish. When the electric field is removed the liquid crystal will revert to the original helical structure. Meyer suggested a method for removing the helical property by using surface effects and bulk elasticity [4], which was proven experimentally by Clark and Lagerwall [5]. Placing the liquid crystal between two closely spaced plates that have been treated to encourage molecular alignment on the plate plane, the surface effect will overpower the bulk helical structure. Due to the planar alignment restricting the director to the two orientations possible from the intersection of the surface plane and the smectic cone, $\phi = 0, \pi$, the material will be bistable

Surface stabilized ferroelectric liquid crystal

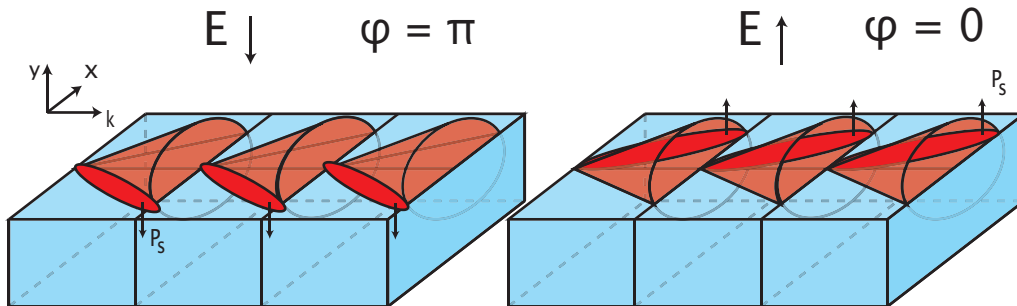


Figure 1.5: The surface effect of the plate plane limits the director to two possible orientations. As such an applied electric field can affect the direction of the spontaneous polarization, P_s , and azimuthal angle, ϕ .

with a macroscopic spontaneous polarization, see Figure 1.5.

Either molecular configuration can be chosen by applying a large enough electric field with the necessary polarity. The electric field will have to be strong enough so that the interaction with the spontaneous polarization overcomes the torque arising from the surface alignment. Such a device configuration is referred to as a surface stabilised ferroelectric liquid crystal (SSFLC). SSFLCs have the properties of fast switching between the bistable states, which when combined with cross polarizers make an effective electro-optic device.

Ferroelectric liquid crystals (FLC) can also have a chiral smectic A* phase at higher temperatures than the smectic C* phase. However, the spontaneous polarization that exists in the layers of smectic C* is nonexistent in smectic A*. The zero tilt of smectic A* means that the rotational symmetry that is present averages the spontaneous polarization to zero. Garoff and Meyer showed that in the presence of an applied electric field the molecules polarization will change the molecular configuration of the FLC to align with the field [6]. This field-induced spontaneous polarization will induce a tilt perpendicular to the field. This is called the electroclinic effect.

The surface anchoring present in the SSFLC allows the bistability that is most useful for the electro-optic switch but it also leads to a major problem. The majority of ferroelectric liquid crystals experience layer shrinkage at the transition from Sm A* to Sm C* transition which can cause defects to occur.

In Sm A* devices the smectic layers are often described as being bookshelf structured, the smectic layers are the books while the bounding plates are the shelves.

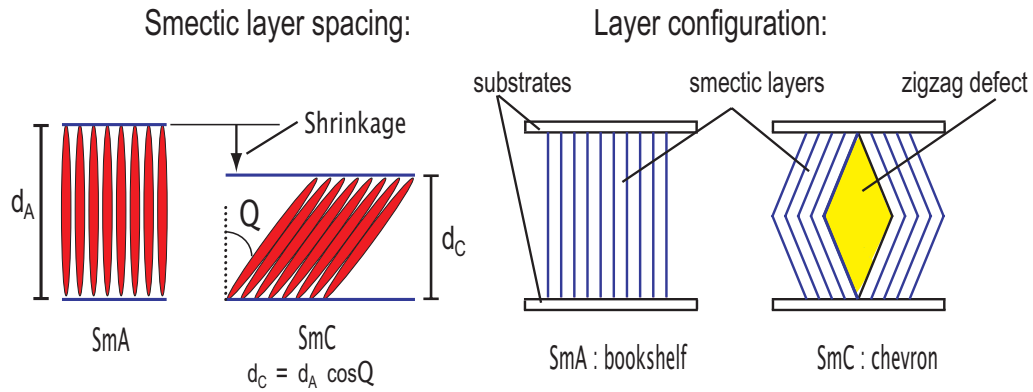


Figure 1.6: Chevron defects from layer shrinkage. d_A is the layer spacing in Sm A, and d_C is the layer spacing in Sm C.

The molecules, spaced with period d_A , are anchored by the surface alignment. Reducing the temperature and transitioning from Sm A* to Sm C*, we generally cause layer shrinkage, but given the surface layer spacing d_A the bulk must collapse into chevrons to accommodate the Sm C* layer spacing d_C , Figure 1.6. The chevron structure was found by Rieker et al. [7] using X-ray scattering techniques. Zigzag defects, named because of the distinctive lines observed optically, form between chevrons of opposing fold direction. These defects have severely hampered the widespread use of SSFLCs as electro-optic devices.

1.4 de Vries type smectics

Materials without substantial smectic layer shrinkage were first discovered by Diele et al. in 1972 [8]. X-ray experiments found that the layer spacing of the smectic A phase was the same as the non-chiral smectic C phase. It was noticed that the Sm A layer thickness was 5-10% smaller than the calculated length of the molecule. More cases of materials exhibiting tilt without layer contraction have been reported

and not a structural transition like conventional smectic materials. Both types of transition are extreme cases and in real smectics C both transition mechanisms could be present in varying degrees.

In recent work theoretical models capable of describing both de Vries type and conventional tilting transitions have been developed. Using the Landau theory with order parameters derived from the \mathbf{Q} orientational order tensor and the smectic layer wave vector, Saunders modeled the transition behaviour of uniaxial material near the tricritical point with first and second order transitions [19, 20]. The optic tilt, specific and latent heat near tricriticality was calculated with the expected behaviour. The model also related the layer contraction with the tilting of the optic axis to produce de Vries type transitions when the nematic order in Sm A was below a critical value, and conventional transitions otherwise. The transition type was dependent on the temperature dependence of the nematic order of the material.

Another theory which models both de Vries type and conventional tilting transitions has been developed by Osipov and Gorkunov [21, 22]. This molecular theory is built from a general intermolecular interaction pair potential with a mean field approach. It assumes that the uniaxial molecules have perfect positional order within the layer so that the potential only depends on the orientations of the molecule pairs. They also discard any interlayer interactions as being negligible. The model has order parameters which are readily measured experimentally, but they can be transformed into the more conventional order parameters of nematic order, nematic tensor biaxiality and optic axis tilt angle. The theory can model both types of transition depending on the model parameters of the pair potential.

In this way the orientational distribution function in Sm A is qualitatively the same for both transitions. The factors for determining the type of transition are the degree of increase in the nematic order parameter and the tilt. As the nematic order increases the layer spacing will increase, while the layer spacing will decrease as the tilt increases. The change in layer spacing will depend on the balance between these two actions. This result mirrors that of Saunders [19, 20]. If the nematic order is high in Sm A, the increase in tilt will cause the layer to contract. If the nematic order is low in Sm A, the contraction due to the tilt will be compensated by the increase in the nematic order.

Osipov and Gorkunov also investigated using the Gay-Berne, electrostatic dipole-dipole, and induction dipole-dipole potentials finding that the Gay-Berne potential alone was insufficient to allow a Sm C phase. They used the same method to investigate chiral molecules [23, 24] and biaxial molecules [25]. This resulted in a greater number of order parameters needed to describe the phase behaviour of the molecules. The assumption of perfect layer positioning meant that the smectic layer spacing was approximated by the average projection of the molecular long axes on the layer normal. This single layer approach was corroborated by a multilayer approach [26]. The layer spacing was calculated by minimization of the free energy and was qualitatively similar to the variation of the average molecular projection. The correlation of the average molecular projection with the actual smectic layer period has also been supported experimentally.

Further work looking at smectic phases over multiple layers was carried out by Emelyanenko [27, 28]. The molecular-statistical theory used a uniaxial molecule with a quadrupole at the core and a transverse dipole at a terminal. Given

this molecular model, the dispersion and electrostatic interactions between pairs of molecules were approximated using a mean-field. It was found that when the quadrupole was small only the tilted uniaxial phases were seen. When the quadrupole was large the tilted biaxial subphases were found.

1.5 Outline of thesis

In each chapter of this thesis we introduce a new way of modelling a de Vries liquid crystal material. In Chapter 2 we concern ourselves with the intermolecular interactions of a pair of molecules. The potentials we look at model the short and long range forces of: steric packing, van der Waals attraction, and dipole-dipole interaction. We will also link these potentials to the Maier-Saupe potential used in Chapter 3. In Chapter 3 we describe a molecular-statistical theory of the Sm A*-Sm C*, order-disorder, phase transition. This density-functional approach will use the mean-field theory to model the interactions of many molecules. In Chapter 4 we will use a simple phenomenological model to investigate device applications. The optoelectric properties of the phenomenological model will be linked to the molecular-statistical theory of the third chapter. Introductions to each of these approaches will be given in each chapter. The overall goal of this thesis is to link the models together, and in this way investigate the effect of the molecular parameters on the optoelectric characteristics of a real device.

2 Modelling intermolecular interactions

2.1 Introduction to molecular potentials

Modelling liquid crystals at the molecular level, we hope to map molecular properties, such as size, shape, dipole location and strength, to the existence of the various states of the liquid crystal. The ability to understand the creation of these mesophases (nematic, smectic, etc.), the optoelectric performance, and their transitions will be of interest to chemists and device engineers.

With the computing power available today it is possible to create molecular models that deal with the interactions of each atom in the molecule. We could then model how these molecules interact with each other. However, looking at systems with the number of molecules needed to simulate these mesophases is computationally demanding. Choosing lower resolution, less detailed, simple models over complex atomistic models will help in the understanding of trends relating molecular properties to creation of mesophases, which could allow chemists to construct liquid crystal molecules which exhibit preferable mesophase behaviour. Therefore, a good model will use simple mathematical functions, to portray the desired physical characteristics. Some accessible reviews of molecular modelling which discuss the creation of the potentials in this Chapter are those by Luckhurst, Rull and Zannoni [29, 30, 31].

The models in this Chapter describe the interaction of two typical molecules dependent on various molecular properties. A molecule is modeled by a point in space and the interaction force it feels from another molecule is specified by a po-

tential energy function. How the system of molecules organises will then depend on how the system attempts to minimise its free energy. We will introduce the free energy in Chapter 3.

There have been many potential models to describe interactions between molecules in fluids. One such potential, which models fluids of spherical atoms, is the Lennard-Jones (L-J) potential [32], Figure 2.1. Describing the interaction of a pair of neutral atoms, it uses two distinct forces for short and long range interactions: a repulsive force akin to the steric effect of the space the atom inhabits at short separations, and an attractive force at long separations describing the van der Waals dispersion force. The potential, $U(\mathbf{r})$, has the form

$$U(r) = 4\epsilon \left[\left(\frac{\sigma}{r} \right)^{12} - \left(\frac{\sigma}{r} \right)^6 \right],$$

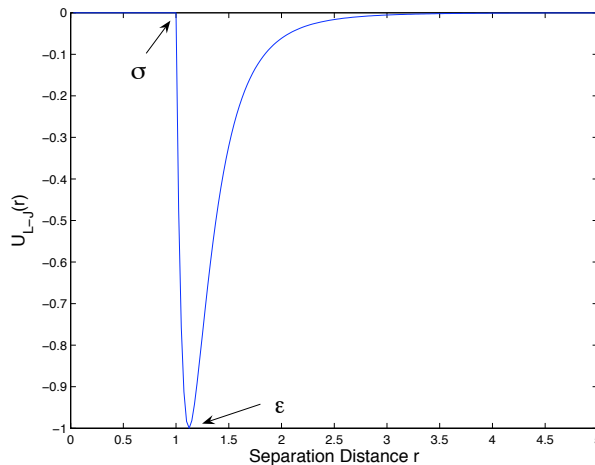


Figure 2.1: The Lennard-Jones potential. r is the distance between two molecules. σ is the contact distance, the minimum separation distance. ϵ is the well-depth of the potential. For this figure, the parameter values are $\epsilon = 1$, $\sigma = 1$.

where ϵ is the depth of the potential well, representing the strength of the attraction between the two atoms, and σ is the (finite) distance at which the interparticle potential is zero, which represents the contact distance of two hard atoms. The potential depends on the distance r between two points, i.e. the centres of mass, in each of the atoms. The r^{-6} term describes attraction and the r^{-12} term describes repulsion; the repulsion term should depend exponentially on the distance but this form was chosen solely for efficiency in analytical calculations, as it is the square of the attractive term.

The Lennard-Jones potential is an effective representation of the repulsive and attractive forces in a fluid consisting of spherical atoms, but it would be insufficient to model the non-spherical molecules commonly associated with liquid crystals. Berne and Pechukas [33] sought to model the shape of roughly ellipsoidal molecules, using a suitably flexible function such as a Gaussian. In this way it was hoped that a potential would be found which allowed the contact distance and well-depth to depend on the orientations of the molecules with respect to each other and on the intermolecular vector, \mathbf{r}_{12} .

The Gaussian to be used is a function of a three dimensional vector \mathbf{x} ,

$$G(\mathbf{x}) = \exp(\mathbf{x} \cdot \boldsymbol{\gamma}^{-1} \cdot \mathbf{x}) \quad , \quad \boldsymbol{\gamma} = (\sigma_{\parallel}^2 - \sigma_{\perp}^2)\mathbf{u}\mathbf{u} + \sigma_{\perp}^2\mathbf{I},$$

where \mathbf{u} is a unit vector along the principal molecular axis and \mathbf{I} is the identity matrix. G represents the distribution of matter in the ellipsoid whose dimensions are $2\sigma_{\parallel}$ and $2\sigma_{\perp}$.

Two molecules interacting will have a pair potential which is the sum of pairwise

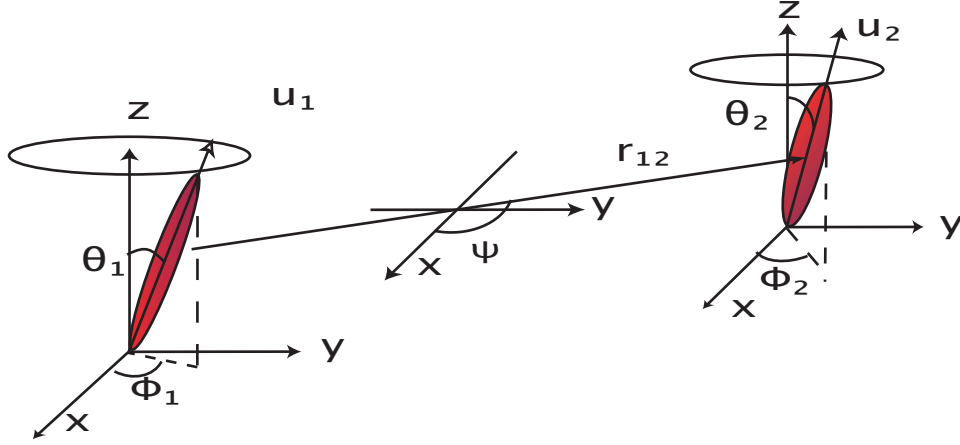


Figure 2.2: Geometry of the model. Two molecules, \mathbf{u}_1 and \mathbf{u}_2 , described by the cone tilt angles $\theta_{1,2}$ and azimuthal angles $\phi_{1,2}$, and the intermolecular vector \mathbf{r}_{12} between the molecular centres of mass, at an angle ψ from the x-axis. We assume $\theta_1 = \theta_2$ for de Vries smectics and use $\phi = \phi_2 - \phi_1$ to describe the relative orientation of the molecules.

interactions of their respective ellipsoids. This is the Gaussian overlap model (GO), the model depends on the short range repulsive force which the shape of the molecule invokes. The interaction of two Gaussian functions will give a potential of interaction between two ellipsoids of revolution as a function of the relative orientations of their axial unit vectors $\mathbf{u}_1, \mathbf{u}_2$ and the vector \mathbf{r}_{12} joining their centres,

$$V(\mathbf{u}_1, \mathbf{u}_2, \mathbf{r}_{12}) = \epsilon(\mathbf{u}_1, \mathbf{u}_2) \exp \left[-\frac{|\mathbf{r}_{12}|^2}{\sigma^2(\mathbf{u}_1, \mathbf{u}_2, \hat{\mathbf{r}}_{12})} \right],$$

where $\epsilon(\mathbf{u}_1, \mathbf{u}_2)$ and $\sigma(\mathbf{u}_1, \mathbf{u}_2, \hat{\mathbf{r}}_{12})$ are angle dependent strength and range parameters, and $\hat{\mathbf{r}}_{12}$ is the unit vector in the direction of \mathbf{r}_{12} . The strength and range parameters have the form

$$\sigma(\mathbf{u}_i, \mathbf{u}_j, \hat{\mathbf{r}}_{ij}) = \sigma_0 \left[1 - \frac{\chi}{2} \left(\frac{(\mathbf{u}_i \cdot \hat{\mathbf{r}}_{ij} + \mathbf{u}_j \cdot \hat{\mathbf{r}}_{ij})^2}{1 + \chi(\mathbf{u}_i \cdot \mathbf{u}_j)} + \frac{(\mathbf{u}_i \cdot \hat{\mathbf{r}}_{ij} - \mathbf{u}_j \cdot \hat{\mathbf{r}}_{ij})^2}{1 - \chi(\mathbf{u}_i \cdot \mathbf{u}_j)} \right) \right]^{-\frac{1}{2}}, \quad (2.1)$$

$$\epsilon(\mathbf{u}_i, \mathbf{u}_j) = \epsilon_0 (1 - \chi^2(\mathbf{u}_i \cdot \mathbf{u}_j)^2)^{-\frac{1}{2}}, \quad (2.2)$$

where $\chi = \frac{(\kappa^2-1)}{(\kappa^2+1)}$, $\kappa = \frac{\sigma_{\parallel}}{\sigma_{\perp}}$ is the length to breadth ratio of both identical ellipsoids, σ_0 and ϵ_0 are scaling constants for the contact distance and the well-depth when the molecules are in the cross configuration. To first order in anisotropy χ , V depends on $(\mathbf{u}_i \cdot \hat{\mathbf{r}}_{ij})$, for $i = 1, 2$, but not on $(\mathbf{u}_i \cdot \mathbf{u}_j)$. This means that we now have an expression for the range parameter that depends on how each molecule is orientated with respect to the intermolecular vector.

Berne and Pechukas [33] devised this Gaussian model to provide simple expressions for the orientation dependence of molecular interactions. They suggested that the orientation dependent strength and range parameters calculated from the interaction of two Gaussian functions could be used in the Lennard-Jones potential. Thus, the Gaussian overlap potential (GO) would have orientational and distance dependence,

$$U_{GO}(\mathbf{u}_1, \mathbf{u}_2, \hat{\mathbf{r}}_{12}) = 4\epsilon(\mathbf{u}_1, \mathbf{u}_2) \left[\left(\frac{\sigma(\mathbf{u}_1, \mathbf{u}_2, \hat{\mathbf{r}}_{12})}{r} \right)^{12} - \left(\frac{\sigma(\mathbf{u}_1, \mathbf{u}_2, \hat{\mathbf{r}}_{12})}{r} \right)^6 \right]. \quad (2.3)$$

The distance at which the two ellipsoids will touch is $r = \sigma(\mathbf{u}_1, \mathbf{u}_2, \hat{\mathbf{r}}_{12})$. This minimum separation distance will depend on \mathbf{u}_1 , \mathbf{u}_2 and $\hat{\mathbf{r}}_{12}$ and is the separation at which the repulsive and attractive components exactly balance.

Although this potential has amended the Lennard-Jones potential to take into account the shape of the molecules being modeled it is not a completely satisfactory model, it has some unrealistic properties. Firstly the potential well-width increases with the contact distance σ . Secondly, the potential well-depth depends only on the angle between the long axes of the respective molecules and not on the angle they make with the intermolecular vector. This means that the well-depths are the same for side-side, SS, and end-end, EE, molecular configurations when we would expect

a stronger interaction for the SS configuration. These unrealistic properties of the Gaussian overlap potential are evident in Figure 2.3, where various orientations of two molecules have been plotted.

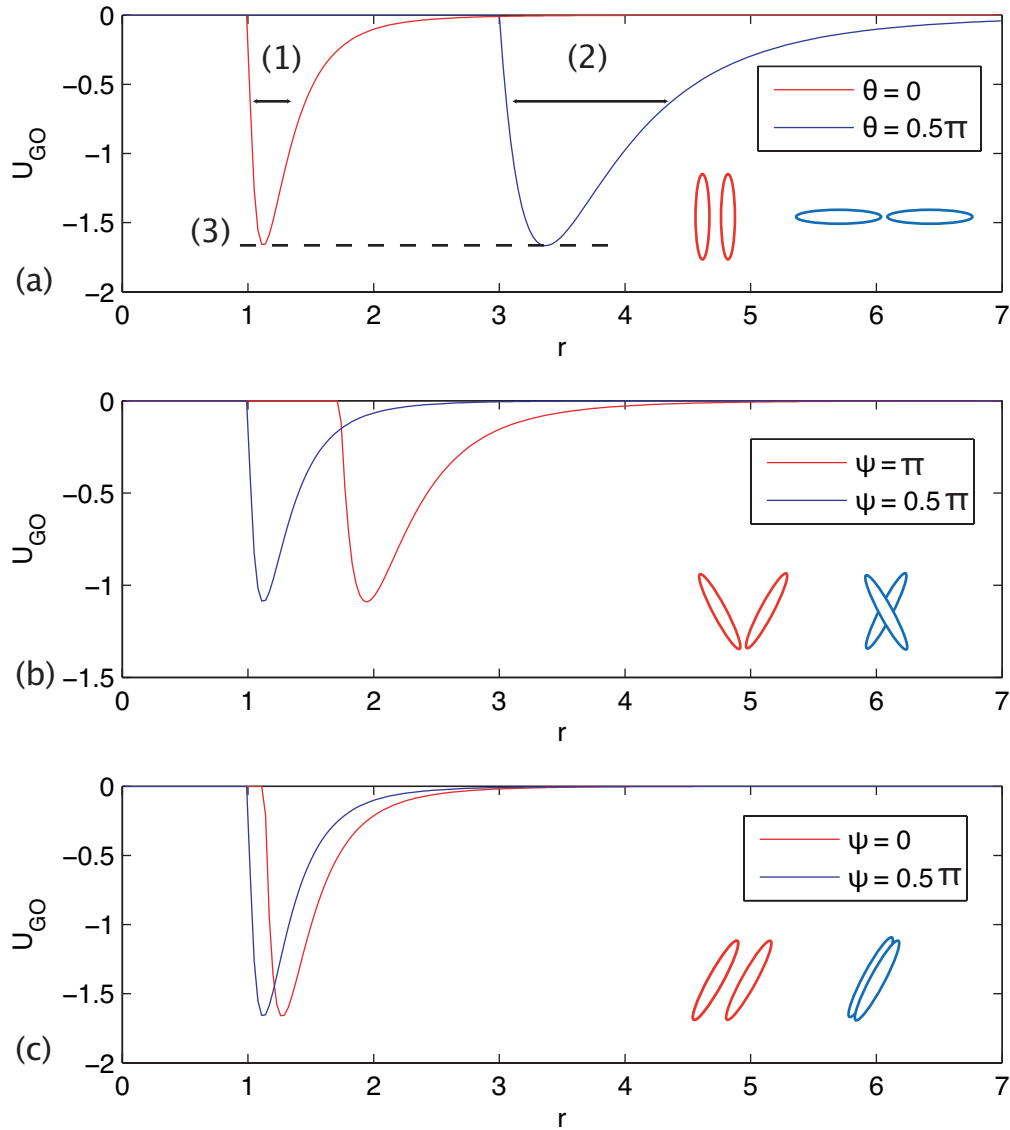


Figure 2.3: Gaussian Overlap potential (2.3) for various orientations of two molecules: (a) side by side orientation $\theta = 0, \psi = 0, \phi = 0$ (red) and end to end orientation $\theta = \frac{\pi}{2}, \psi = 0, \phi = 0$ (blue), (b) $\theta = \frac{\pi}{6}, \psi = \pi, \phi = \pi$ (red) and $\theta = \frac{\pi}{6}, \psi = \frac{\pi}{2}, \phi = \pi$ (blue), (c) $\theta = \frac{\pi}{6}, \phi = 0, \psi = 0$ (red) and $\theta = \frac{\pi}{6}, \phi = 0, \psi = \frac{\pi}{2}$ (blue). The well-width varies with the contact distance, (1) and (2). The well-depth is the same for side-side and end-end configurations (3).

Gay and Berne [34] attempted to overcome these drawbacks in the Gaussian overlap model by comparing the GO potential to a site-site Lennard-Jones (SSLJ) potential. The site-site interaction model has the form

$$U_{ss} = \sum_{\alpha,\beta} \epsilon_{\alpha\beta} f\left(\frac{r_{\alpha\beta}}{\sigma_{\alpha\beta}}\right), \quad (2.4)$$

where $\epsilon_{\alpha\beta}$ and $\sigma_{\alpha\beta}$ are energy and distance parameters for interactions between sites α on molecule 1 and β on molecule 2 and f is the Lennard-Jones potential; this is the n site-site Lennard-Jones potential (nSSLJ). The short range attractive and repulsive interactions can be effectively represented by designating several sites in each molecule between which Lennard-Jones potentials act. However, larger molecules require many sites to adequately represent them which would lead to inefficiencies in computing.

2.1.1 Gay-Berne potential

Gay and Berne [34] avoid the problem of modelling large molecules with many LJ sites by modelling the site-site potential with a single-site potential. They compared a GO potential for molecules with axial ratio 3:1 with a 4SSLJ potential. The behaviour of the 4SSLJ potential does not have the same drawbacks as the GO model. The SS well-depth is deeper than the EE well-depth which is more realistic. The SS-EE well-depth ratio is approximately 5:1. Also, the well-width is approximately independent of orientations. From this analysis Gay and Berne used two modifications to remedy the faults of the GO model. The first modification, which had been suggested by Stone [35], was to use the shifted distance rather than the scaled separation. This meant that rather than dilate the Lennard-Jones

potential, the overlap range parameter displaces it. The new form of the potential would then be

$$U_{GB}(\mathbf{u}_i, \mathbf{u}_j, \hat{\mathbf{r}}_{ij}) = 4\epsilon(\mathbf{u}_i, \mathbf{u}_j, \hat{\mathbf{r}}_{ij})(R^{12} - R^6), \quad (2.5)$$

$$\text{where} \quad R = \frac{\sigma_0}{r - \sigma(\mathbf{u}_i, \mathbf{u}_j, \hat{\mathbf{r}}_{ij}) + \sigma_0}.$$

The repulsive and attractive terms still cancel at $r = \sigma$ so the ellipsoidal core is retained, but the well-width is independent of orientation. The second modification remedies the lack of dependence of the strength parameter ϵ on the molecules' orientation with respect to the intermolecular vector by introducing a new form for the parameter

$$\epsilon(\mathbf{u}_i, \mathbf{u}_j, \hat{\mathbf{r}}_{ij}) = \epsilon_0[\epsilon(\mathbf{u}_i, \mathbf{u}_j)]^\nu[\epsilon'(\mathbf{u}_i, \mathbf{u}_j, \hat{\mathbf{r}}_{ij})]^\mu, \quad (2.6)$$

where $\epsilon(\mathbf{u}_i, \mathbf{u}_j)$ is (2.2) and

$$\epsilon'(\mathbf{u}_i, \mathbf{u}_j, \hat{\mathbf{r}}_{ij}) = 1 - \frac{\chi'}{2} \left(\frac{(\mathbf{u}_i \cdot \hat{\mathbf{r}}_{ij} + \mathbf{u}_j \cdot \hat{\mathbf{r}}_{ij})^2}{1 + \chi'(\mathbf{u}_i \cdot \mathbf{u}_j)} + \frac{(\mathbf{u}_i \cdot \hat{\mathbf{r}}_{ij} - \mathbf{u}_j \cdot \hat{\mathbf{r}}_{ij})^2}{1 - \chi'(\mathbf{u}_i \cdot \mathbf{u}_j)} \right), \quad (2.7)$$

$$\chi' = \frac{(\kappa'^{\frac{1}{\mu}} - 1)}{(\kappa'^{\frac{1}{\mu}} + 1)}. \quad (2.8)$$

Here κ' is the ratio of side-side to end-end well-depths. Gay and Berne found a satisfactory fit to the site-site potential with parameter values $\kappa = 3$, $\kappa' = 5$, $\nu = 1$ and $\mu = 2$. The single site potential reproduces the behaviour of the site-site potential rather well. Increasing the number of sites in the SSLJ potential will only increase the faithfulness of the modified overlap potential as the unoccupied space

around the sites will reduce, becoming more ellipsoidal as a whole. The Gay-Berne potential (GB) should not be taken as a mere fit to the SSLJ potential, as evidence of nematic ordering in a GB fluid has been found in situations where the 4SSLJ

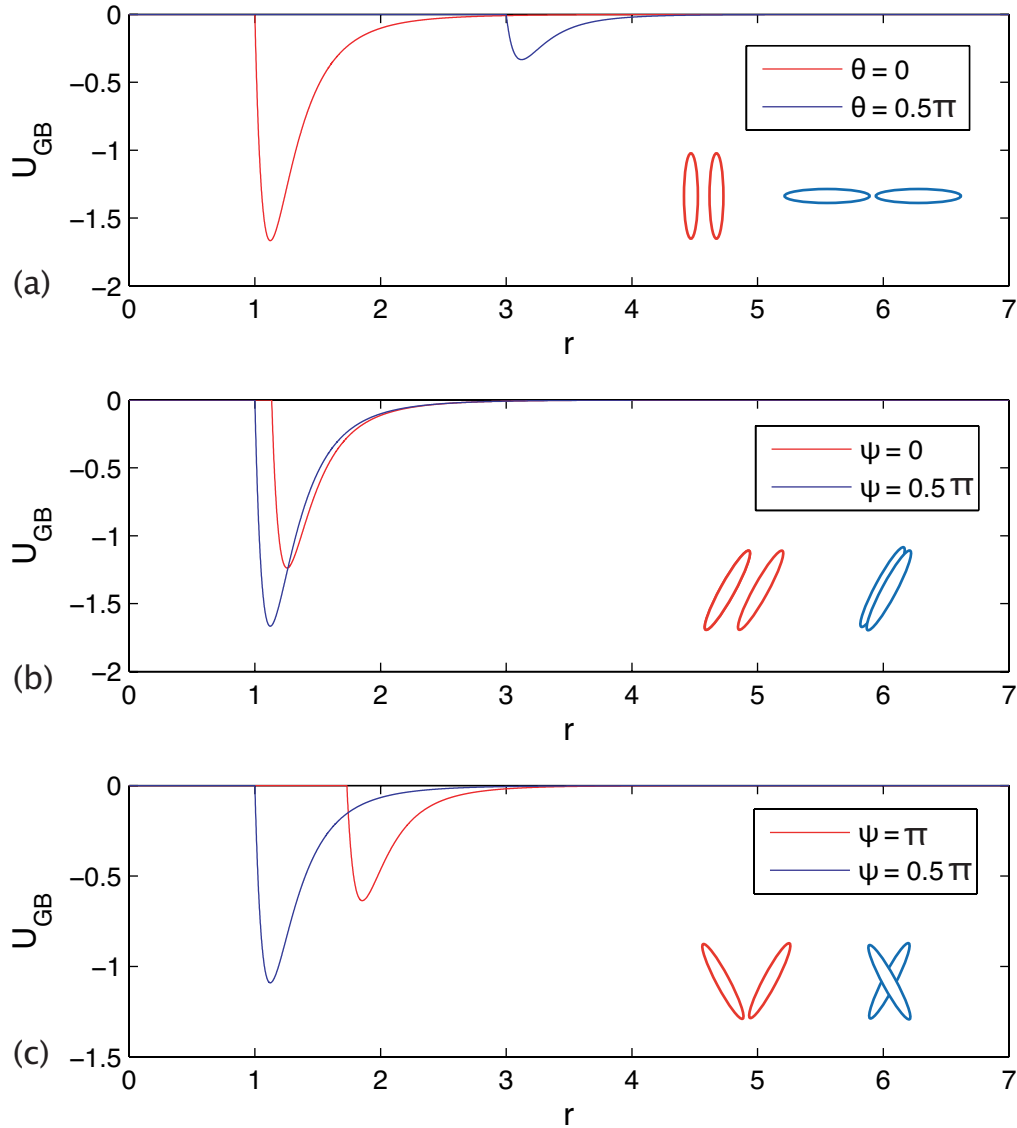


Figure 2.4: Gay-Berne potential (2.5). The well-depths for various orientations of two molecules: (a) $\kappa' = 5$, side by side orientation $\theta = 0, \psi = 0$ (red) and end to end orientation $\theta = \frac{\pi}{2}, \psi = 0$ (blue), (b) $\theta = \frac{\pi}{6}, \psi = 0, \phi = 0$ (red) and $\theta = \frac{\pi}{6}, \psi = \frac{\pi}{2}, \phi = 0$ (blue), (c) $\theta = \frac{\pi}{6}, \phi = \pi, \psi = \pi$ (red) and $\theta = \frac{\pi}{6}, \phi = \pi, \psi = \frac{\pi}{2}$ (blue). The interaction potential has lower minimum when the molecular centres are closest and the space between molecules is reduced.

potential leads to no nematic ordering. Figure 2.4 shows the U_{GB} as a function of r for various orientations of the molecules; when the molecular centres are closest the potential has minimum energy. We can see that the potential has corrected the faults of the GO potential. The SS well-depth is lower than the EE and the well-width does not vary with the separation distance. We can also see that, where the GO potential had the same well-depths for the molecular orientations in (b) and (c), the GB potential now depends on the intermolecular vector.

The Gay-Berne model mesogen has four parameters $(\kappa, \kappa', \mu, \nu)$ which control the molecular interaction energy and allow investigation of the liquid crystal behaviour of different mesogenic molecules. Bates and Luckhurst [36] suggested the mnemonic GB($\kappa, \kappa', \mu, \nu$) to describe the different Gay-Berne mesogens. Adams and Luckhurst [37] demonstrated using molecular dynamics simulations that for the mesogen suggested by Gay and Berne, GB(3,5,2,1), isotropic and nematic phases formed. Coincidentally Luckhurst and Stephens [38] investigated GB(3,5,1,2) and discovered the formation of smectic A and smectic B phases also. The change to the mesogen parameters resulted in increases in well-depth for both side-side and end-end configurations. Since then many other GB mesogens have been investigated [29].

2.1.2 Electrostatic dipole-dipole interaction

The Gay-Berne potential models the forces of repulsion and attraction of a simple ellipsoid shaped molecule only, which means that another potential will need to be added if the model is to include dipole-dipole interactions. A dipole exists when there is an inhomogeneous charge density within the molecule, meaning that the

electrons within the overall neutrally charged atoms of the molecule redistribute causing localised poles. Dipole interactions have long range effects and are expected to have a significant contribution to the potential. A chiral smectic C material will have a spontaneous polarisation component parallel with the short axis of the molecule \mathbf{b}_i , which is perpendicular to the plane containing the smectic layer normal and the long axis (\mathbf{u}_i) of the molecule, (see Fig 2.5). The resulting dipole-dipole interaction potential of two molecules each containing a dipole is

$$U_{DD}(\mathbf{u}_1, \mathbf{r}_{12}, \mathbf{u}_2) = -r^{-5} d_{\perp}^2 [3(\mathbf{r} \cdot \mathbf{b}_1)(\mathbf{r} \cdot \mathbf{b}_2) - r^2 \mathbf{b}_1 \cdot \mathbf{b}_2], \quad (2.9)$$

where the interacting dipoles are orientated along the axes, $\mathbf{d}_i = d_{\perp} \mathbf{b}_i$, $\mathbf{r} = \mathbf{r}_{12} + \nu(\mathbf{u}_2 - \mathbf{u}_1)$, ν is the dipole location from the centre-of-mass (c.o.m) of both molecules and \mathbf{r}_{12} is the vector from the c.o.m. of molecule 1 to the c.o.m. of molecule 2 [22].

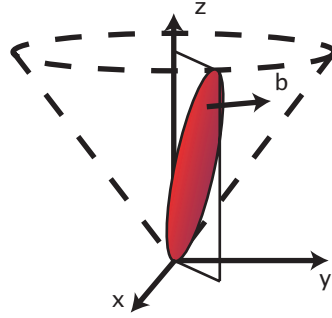


Figure 2.5: Dipole model. The dipole, parallel to short axis \mathbf{b} , is perpendicular to the plane containing the layer normal, z , and the long axis of the molecule.

2.1.3 Further investigation of the Gay-Berne and dipole-dipole interaction potentials

So far we have introduced the Gay-Berne (2.5) and the electrostatic dipole-dipole (2.9) interaction potentials. These potentials model the steric effect of the shape of the molecules, the van der Waals dispersion force, and the dipole-dipole interactions. Let us now illustrate the behaviour of these two potentials. Initially, we will investigate how the orientation of each molecule relative to each other will affect the energies of the standard GB(3, 5, 2,1) potential and an arbitrary dipole-dipole potential ($\nu = 0.6$, $d_{\perp} = 0.5$). Then, we will vary the model parameters: molecular length-breadth ratio κ , well-depth ratio side-side/end-end κ' , dipole location ν and strength d_{\perp} , and show how they affect the potential. Next, we will integrate the potentials over the molecular displacement vector \mathbf{r} assuming a uniform distribution of molecules in \mathbf{r} . This will result in a pair potential depending only on the respective orientations of the molecules, the tilt and azimuth angles $[(\phi_1, \theta_1), (\phi_2, \theta_2)]$. We will then analyse the behaviour of the potential by varying the model parameters. Fully understanding the behaviour of our model potential will be useful for later Chapters. We will see in the next Chapter how a potential describing the interaction of two molecules depending only on (ϕ_i, θ_i) can then be used to model the phase transition from smectic A to smectic C.

In Figure 2.4 the Gay-Berne potential, GB(3,5,2,1), was plotted for three different molecular configurations. The orientation variables varied were; θ , the tilt angle, ϕ , the difference in azimuth angles, and ψ , the intermolecular angle. From these plots we can see that the potential well-depths and the separation distance at which these occur can vary drastically depending on the molecular configuration.

The potential energy is minimised when the molecular centres are closest and when the unoccupied space between the two molecules is minimised. In Figure 2.6 the Gay-Berne (GB) and dipole-dipole (DD) potentials are calculated for a circular region with radius four at the origin for two different molecular orientations. The colormap represents the energy of the potential when the first molecules c.o.m. is located at the origin with orientation $\phi = 0$ and $\theta_1 = \theta$, and the c.o.m. of a second molecule, with $\phi_2 = \phi$ and $\theta_2 = \theta$, is positioned at that point in the space. Each radial from the origin is representative of Figure 2.4 with angle ψ from the x axis. The empty centre of the colormap shows where the two molecules would overlap. In Figure 2.6 (a) and (c) the U_{GB} is minimum when $\psi = \frac{\pi}{2}$, low when

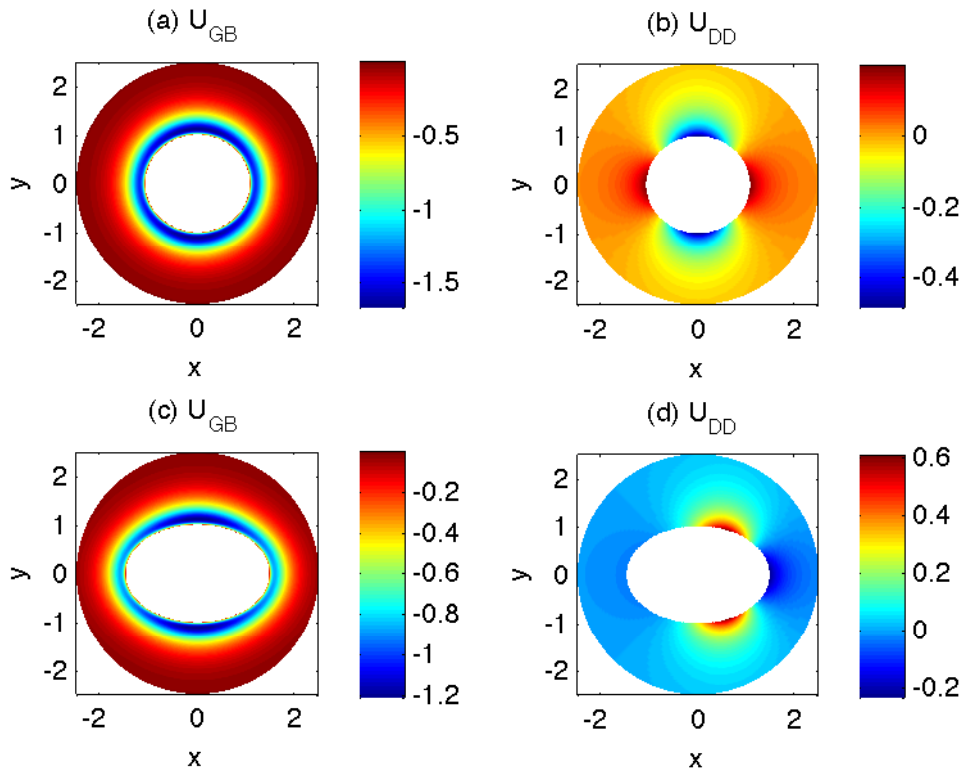


Figure 2.6: The Gay-Berne and dipole-dipole potential as a surface depending on \mathbf{r}_{12} , the variables (r and ψ), for the molecular orientations ($\phi = 0, \theta = \frac{\pi}{8}$) in (a), (b) and ($\phi = \pi, \theta = \frac{\pi}{8}$) in (c) and (d).

the molecules c.o.m are close (r small) and increases as the c.o.m. move further from one another (r increasing). In Figure 2.6 (b) and (d) the U_{DD} is minimum when $\psi = \frac{\pi}{2}$ and $\psi = 0$ respectively. These relative orientations allow the dipoles to align. The GB energy is minimised depending on a balance of the molecular centres closeness and reduction of unoccupied space between the molecules. The DD potential is minimised when the ‘negative’ end of a dipole is not positioned alongside another, but near a ‘positive’ end of a dipole.

We now consider how the molecular parameters affect the related potentials. For the GB potential we vary κ , the length-breadth ratio of the molecules. In Figure 2.7, the effects of lengthening the molecules can be seen through an increase of

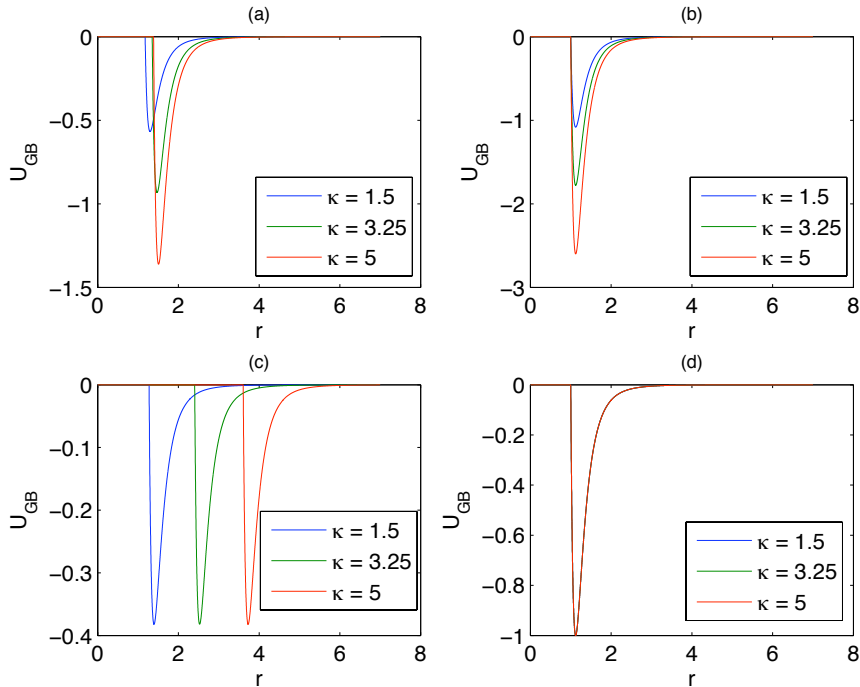


Figure 2.7: GB potential in 4 molecular configurations varying molecular length to breadth ratio κ . (a) $\phi = 0, \theta = \frac{\pi}{4}, \psi = 0$, (b) $\phi = 0, \theta = \frac{\pi}{4}, \psi = \frac{\pi}{2}$, (c) $\phi = \pi, \theta = \frac{\pi}{4}, \psi = 0$, (d) $\phi = \pi, \theta = \frac{\pi}{4}, \psi = \frac{\pi}{2}$

the preferred separation distance when the configuration would otherwise result in an overlap of molecules. We also note that the minimum energy decreases when the unoccupied space decreases. There is no change in (d) due to the cross configuration of the molecules being unaffected by increasing molecule length.

In Figure 2.8 we consider the dipole-dipole potential and vary the four model parameters: molecular length to breadth ratio κ , well-depth ratio κ' , dipole location ν , and dipole strength d_{\perp} for one molecular configuration. As we increase κ the separation distance increases also. In the chosen tilted molecular configuration, lengthening the molecules, increasing κ , has increased the minimum separation distance $\sigma(2.1)$ of the Gay-Berne potential. The dipole-dipole potential is independent of κ' . The molecular orientation of $\phi = \frac{\pi}{6}, \psi = \frac{\pi}{2}$ aligns the ‘negative’

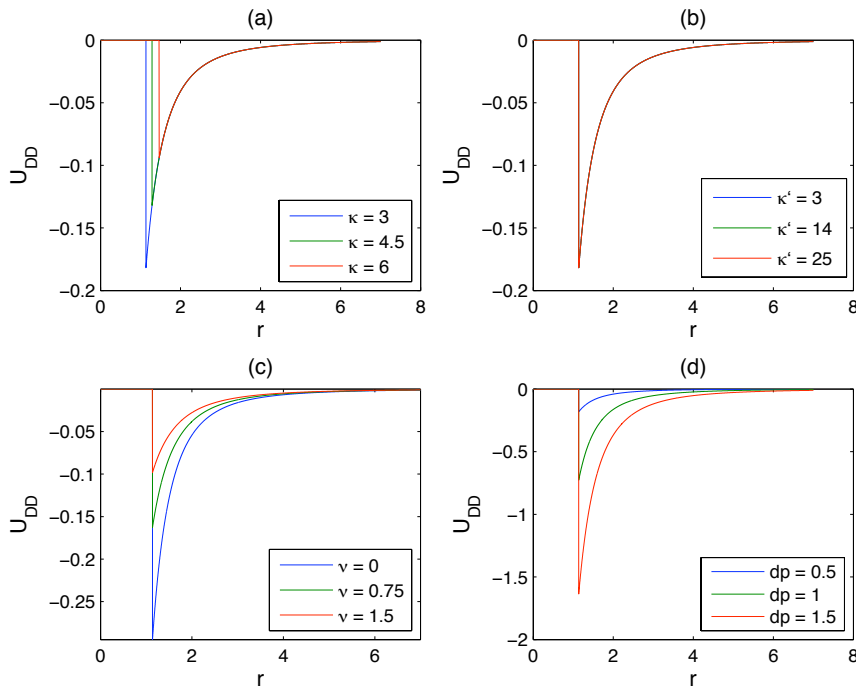


Figure 2.8: DD potential varying: molecular length to breadth ratio κ , well-depth ratio κ' , dipole location ν , and dipole strength d_{\perp} . $\phi = \frac{\pi}{6}, \theta = \frac{\pi}{4}, \psi = \frac{\pi}{2}$

part of a dipole on the first molecule with the ‘positive’ part of the dipole on the second molecule. Sterically, the molecules are closest at their cores, so U_{DD} will have lowest energy when the dipole is located at the core. As the dipole location moves further from the core along the molecule, the dipoles move further from one another due to the relative orientation, thus resulting in U_{DD} increasing. The dipole-dipole potential energy is proportional to d_{\perp}^2 , so as expected, when two dipoles align U_{DD} will have lower energy when the dipole strength d_{\perp} increases.

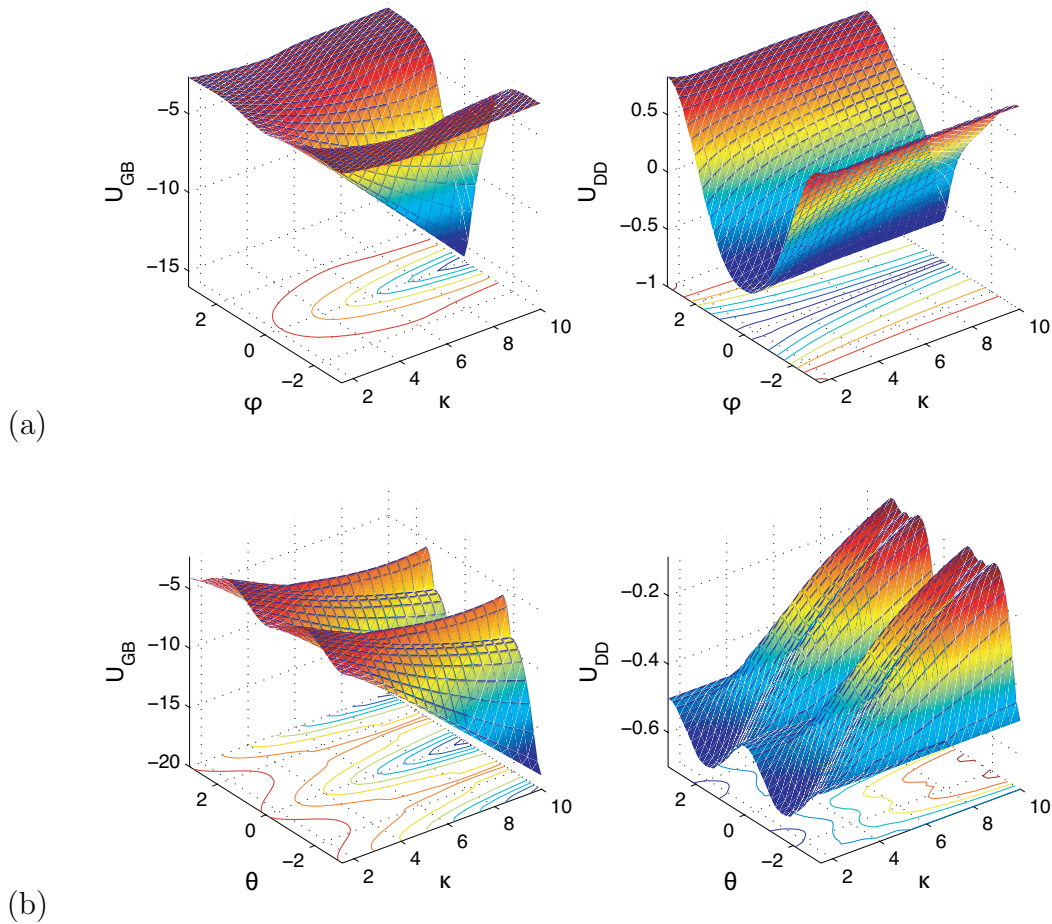


Figure 2.9: Surfaces of U_{GB} and U_{DD} as functions of (ϕ, κ) with: (a) $\theta = \frac{\pi}{4}$ and (b) $\phi = \frac{\pi}{6}$.

A complete picture of the Gay-Berne and the dipole-dipole potential calculations integrated over \mathbf{r}_{12} are shown in Figures 2.9 and 2.10. In Figures 2.9 and 2.10 we have integrated U_{GB} and U_{DD} over \mathbf{r}_{12} as a surface for $-\pi \leq \phi \leq \pi$ with $\theta = \frac{\pi}{4}$, and as a surface while varying $-\pi \leq \theta \leq \pi$ with $\phi = \frac{\pi}{6}$ for the four molecular parameters.

In Figure 2.9, increasing κ decreases the minimum energy and increases, to a lesser extent, the maximum energy of U_{GB} . The effect of κ on U_{DD} is more complicated. In Figure 2.9 (a) with a fixed tilt angle ($\theta = \frac{\pi}{4}$) we see that increasing κ increases the minimum energy of U_{DD} but its influence reduces as the molecules lengthen and the minimum separation distance asymptotes to $\frac{\sigma_0}{\cos\theta}$. In Figure 2.9 (b) with a fixed azimuthal angle $\phi = \frac{\pi}{6}$, the tilt angle at which the U_{DD} has minimum energy changes when increasing κ . Initially, $\theta = \pm\frac{\pi}{2}$ has minimum energy but as κ increases $\theta = 0$ or $\pm\pi$ is preferred.

In Figure 2.10 we look at how the remaining molecular parameters affect their respective potentials. In Figure 2.10 (a) Increasing κ' appears to increase the U_{GB} potential energy across all molecular configurations. In Figure 2.10 (b) increasing ν decreases the minimum and increases the maximum energy of U_{DD} . Fixing $\phi = \frac{\pi}{6}$ and increasing ν , we see that the preferred θ stays constant but decreases the minimum energy, while the θ with maximum energy changes. (c) The dipole-dipole potential is proportional to d_{\perp}^2 so we see increasing dipole strength magnifies the potential energy across all molecular orientations.

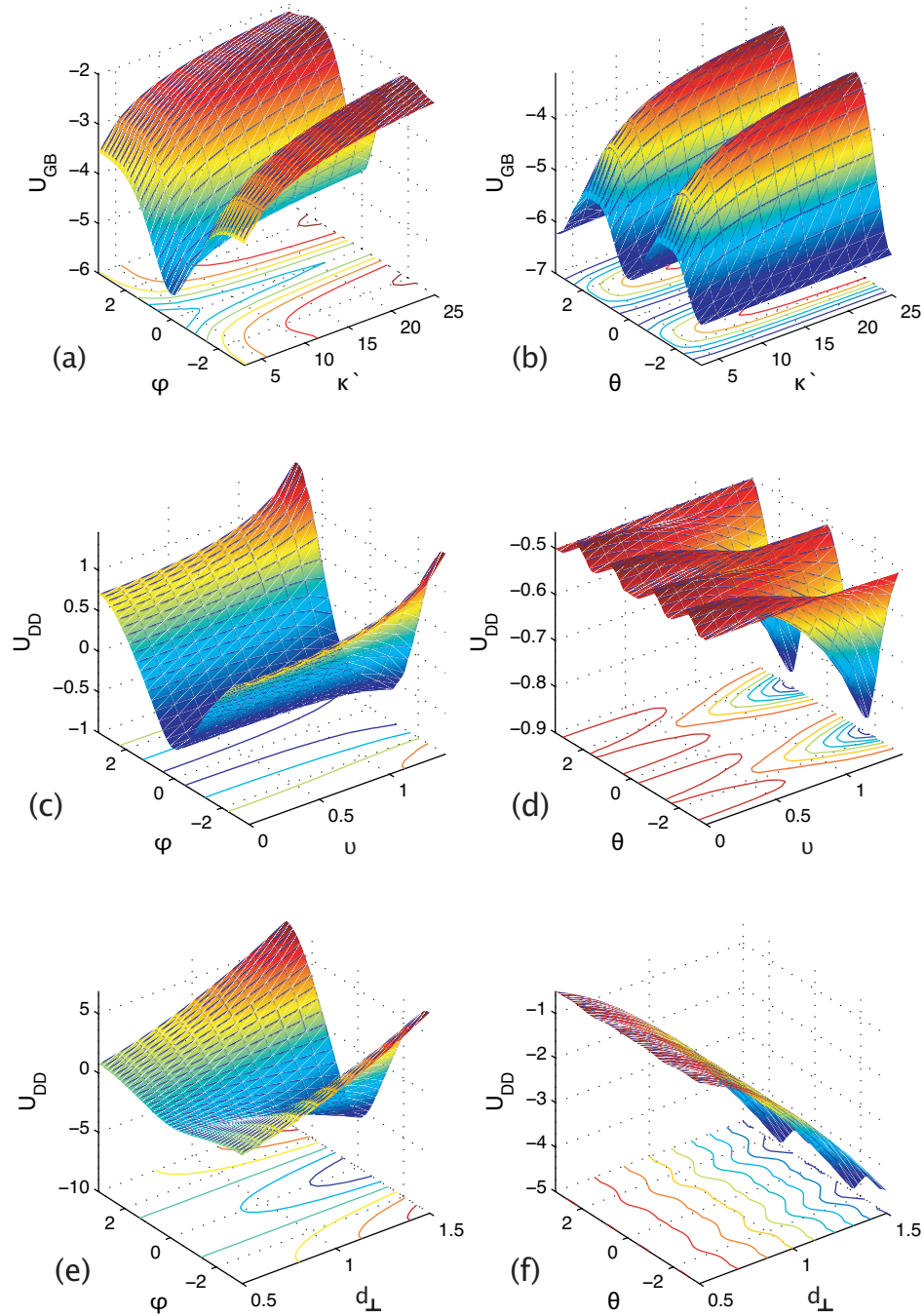


Figure 2.10: (a) U_{GB} as a function of (ϕ, κ') with $\theta = \frac{\pi}{4}$, and (θ, κ') with $\phi = \frac{\pi}{6}$. (b) U_{DD} as a function of (ϕ, ν) and (θ, ν) . (c) U_{DD} as a function of (ϕ, d_{\perp}) and (θ, d_{\perp}) .

2.2 An analytic form of the averaged Gay-Berne and dipole-dipole potentials

The aim of modelling liquid crystals at the molecular level is to be able to map molecular properties to the existence of various states of liquid crystal. We hope to understand the effect the microscopic pair interaction potential has on the thermodynamic behaviour of the macroscopic system. In the next Chapter we examine in detail how we can calculate the free energy of a system of molecules from the foundation of the interaction pair potential. Given the current forms of the two potentials, analysis of the free energy would be impossible. We now try to find an expression that will allow us to calculate the free energy.

We will assume two molecules on a fixed smectic cone (cone angle θ), integrate out the \mathbf{r} dependence and look at the potential for different positions on the cone. The GB(3,5,2,1) potential (2.5) was calculated and integrated over \mathbf{r}_{12} and is shown in Figure 2.11: (a) for three cone angles ($\theta_1 = \theta_2 = \theta$) and a range of azimuth difference angles ($\phi = \phi_2 - \phi_1$), (b) for three azimuth difference angles ($\phi = \phi_2 - \phi_1$) and a range of cone angles ($\theta_1 = \theta_2 = \theta$), and (c) over a range of (ϕ, θ) . We repeated the same process for the dipole-dipole potential (2.9, shown in Figure 2.12, here we use $d_{\perp} = 0.5$, $\nu = 0.6$). It is apparent that the $U_{GB}(\phi, \theta)$ and $U_{DD}(\phi, \theta)$ are periodic functions in ϕ and θ . As such, we can perform a Fourier series decomposition that will approximate these potentials. This harmonic analysis will result in a simpler form of the potentials more suitable for further analysis. We will therefore calculate a Fourier cosine series in ϕ and θ in the hope that they will approximate the molecular potentials sufficiently.

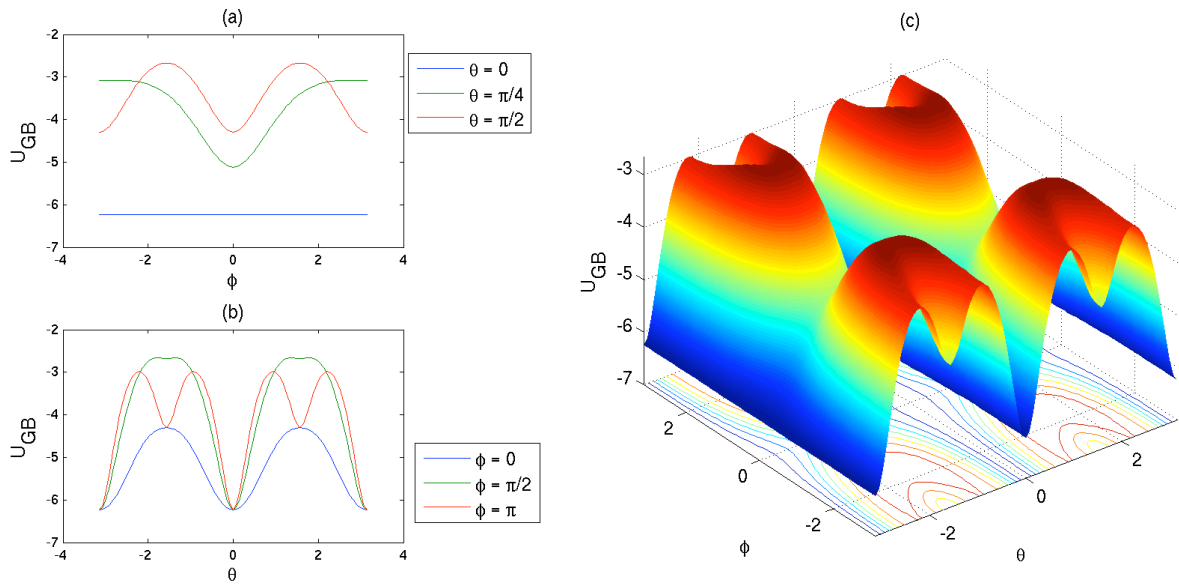


Figure 2.11: The periodic nature of GB(3,5,2,1): (a) U_{GB} periodic in ϕ , (b) U_{GB} periodic in θ , and (c) the surface of $U_{GB}(\phi, \theta)$ over θ and ϕ . As θ increases the minimum at $\phi = 0$ is joined by another minimum at $\phi = \pi$.

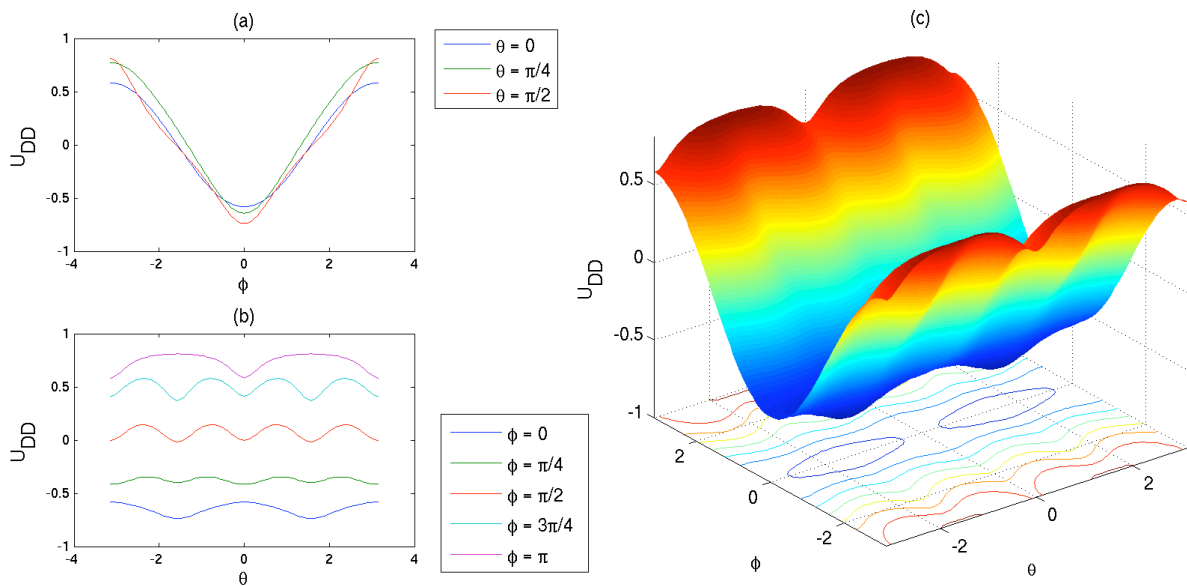


Figure 2.12: The periodic nature of U_{DD} : (a) U_{DD} periodic in ϕ , (b) U_{DD} periodic in θ , and (c) the surface of $U_{DD}(\phi, \theta)$ over θ and ϕ .

2.2.1 Fourier Analysis

Assuming the characteristics of the pair potential can be fitted by a harmonic series, the potential is approximated by

$$U \approx \sum_{m,n=0}^N A_{mn} \cos m\theta \cos n\phi \quad (2.10)$$

where, for the following analysis, we have chosen $N = 4$.

Given the orthogonal nature of the cosine function we can calculate the Fourier coefficients of the pair potentials as

$$A_{00} = \frac{1}{2\pi} \int_{-\pi}^{\pi} \int_{-\pi}^{\pi} U_{pp} d\phi d\theta, \quad A_{mn} = \frac{1}{\pi} \int_{-\pi}^{\pi} \int_{-\pi}^{\pi} U_{pp} \cos n\phi \cos m\theta d\phi d\theta, \quad (2.11)$$

where U_{pp} is a pair potential dependent on ϕ and θ .

To determine which modes are significant in the approximation we will look at the magnitude of the Fourier coefficients. Using Matlab, the coefficients were calculated for the Gay-Berne and dipole-dipole potential. The approximations for the GB(3,5,2,1) (2.5), and the dipole-dipole ($v = 0.6, d_{\perp} = 0.5$) (2.9) potentials, where the modes with coefficients of order $O(\frac{A_{mn}}{A_{00}}) > 0.01$, are shown below

$$\begin{aligned} U_{GB} = & -4.23 - 1.34 \cos 2\theta - 0.54 \cos 4\theta - 0.55 \cos \phi - 0.08 \cos 2\theta \cos \phi \\ & + 0.46 \cos 4\theta \cos \phi - 0.35 \cos 2\phi + 0.37 \cos 2\theta \cos 2\phi - 0.02 \cos 4\theta \cos 2\phi \\ & - 0.04 \cos 3\phi + 0.02 \cos 2\theta \cos 3\phi + 0.04 \cos 4\theta \cos 3\phi \\ & - 0.03 \cos 4\phi + 0.04 \cos 2\theta \cos 4\phi - 0.01 \cos 4\theta \cos 4\phi, \end{aligned} \quad (2.12)$$

$$\begin{aligned}
U_{DD} = & 0.06 + 0.005 \cos 2\theta - 0.056 \cos 4\theta - 0.69 \cos \phi + 0.036 \cos 2\theta \cos \phi \\
& + 0.03 \cos 4\theta \cos \phi - 0.013 \cos 2\phi - 0.01 \cos 2\theta \cos 2\phi + 0.027 \cos 4\theta \cos 2\phi \\
& - 0.034 \cos 3\phi + 0.046 \cos 2\theta \cos 3\phi - 0.012 \cos 4\theta \cos 3\phi \\
& - 0.0004 \cos 4\phi - 0.0008 \cos 2\theta \cos 4\phi + 0.0046 \cos 4\theta \cos 4\phi. \quad (2.13)
\end{aligned}$$

There is a clear drop in the order of magnitude of the Fourier coefficients after the $\cos 2\phi$ mode of U_{GB} (2.12), so in order to use the simplest approximation to the potentials we examine the differences when including only those modes up to $\cos 2\phi$ and all modes up to $\cos 4\phi$. In Figure 2.13 we have plotted the two pair potentials

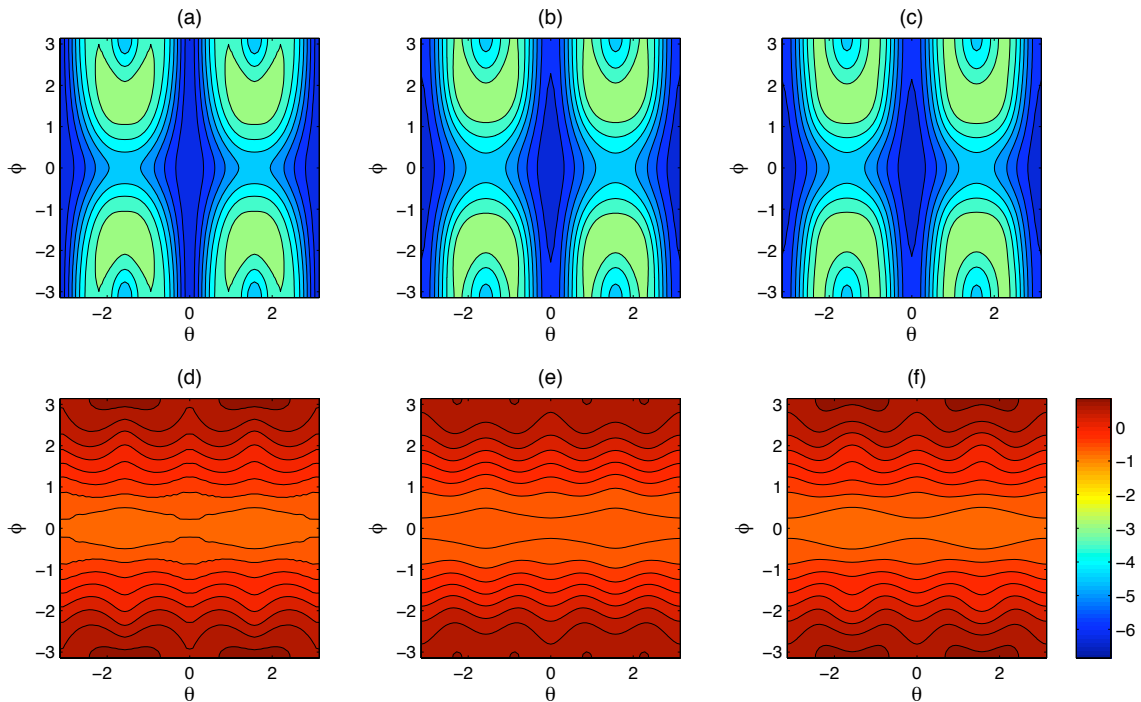


Figure 2.13: Contour plots of the (a) U_{GB} and (d) U_{DD} potentials and two examples of Fourier series approximations. Approximations include: (b) all modes to $\cos 2\phi$ from (2.12), (c) all modes to $\cos 4\phi$ from (2.12), (e) all modes to $\cos 2\phi$ from (2.13), (f) all modes to $\cos 4\phi$ from (2.13). The simpler approximations (b) and (e) are sufficient to capture the characteristics of U_{GB} and U_{DD}

as contour plots and included the approximations to the potentials also. The general properties of both potentials are also present in the two approximations. This would suggest that an approximation up to mode $\cos 2\phi$ would be sufficient to capture the essence of both potentials whilst also reducing the complexity of the model.

In Figure 2.14 we have plotted the Gay-Berne potential, GB(3,5,2,1), the dipole-

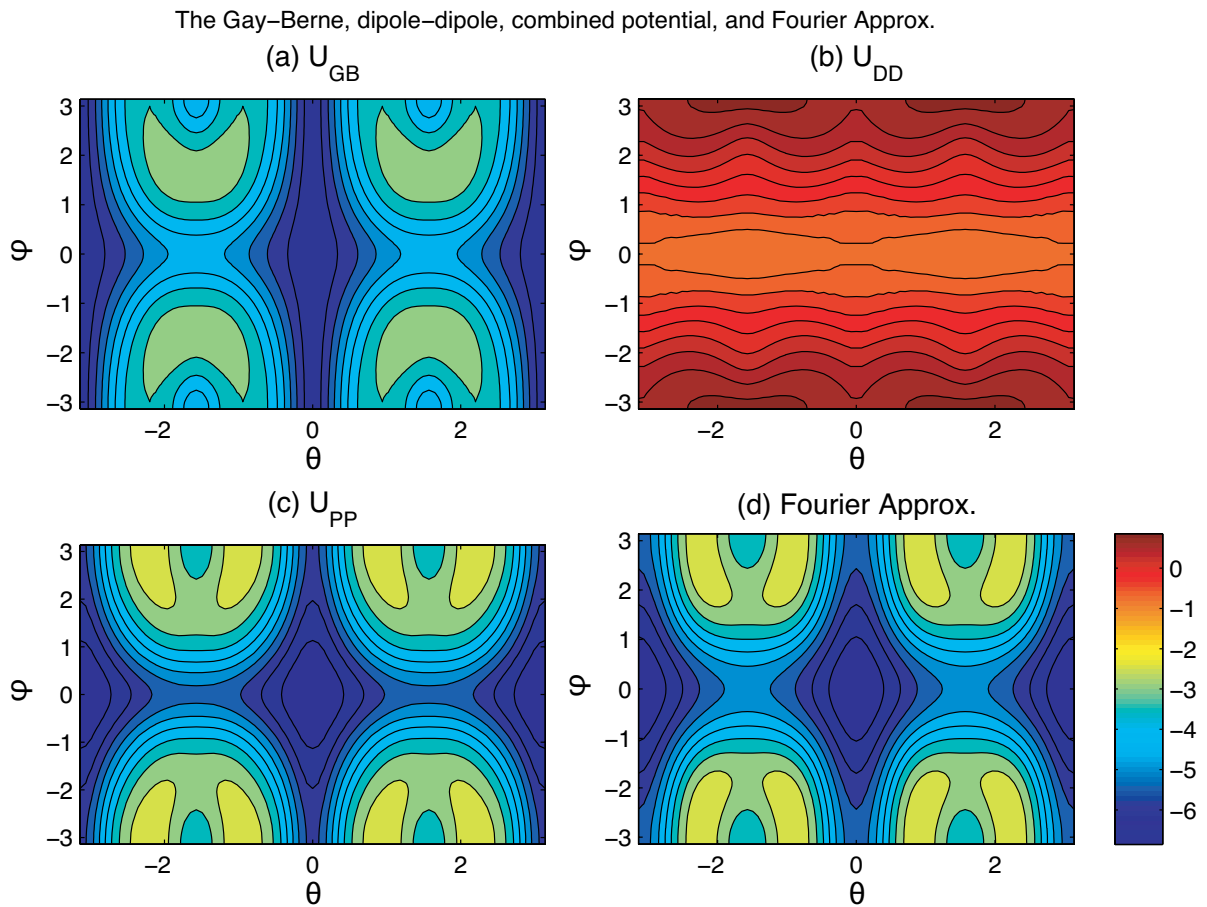


Figure 2.14: (a) $U_{GB}(\phi, \theta)$ and (b) $U_{DD}(\phi, \theta)$ were combined in (c) $U_{pp}(\phi, \theta)$. The Fourier approximation, which captures the characteristics of $U_{pp}(\phi, \theta)$, is plotted in (d).

dipole potential ($v = 0.6, d_{\perp} = 0.5$), the combined potential and the Fourier approximation to the combined potential. The Fourier approximation includes all combinations of the constant term, $\cos \phi$, $\cos 2\phi$, $\cos 2\theta$ and $\cos 4\theta$. The dipole-dipole potential was chosen to augment the Gay-Berne potential but not dominate it. The Fourier approximation exhibits similar energy levels and locations of the stationary points as the combined potential.

Now we look at how varying the molecular parameters alters the pair potential and the coefficients of the Fourier modes approximating it. A base state was chosen ($\kappa = 3, \kappa' = 5, v = 0.6, d_{\perp} = 0.5$) from which we systematically varied a single parameter while keeping the others constant. The results are plotted in Figure 2.15. We can see that, over the range of model parameters tested, all the Fourier coefficients are either of significant magnitude or dependent on a model parameter.

The Gay-Berne and dipole-dipole interaction potentials describe excluded volume effects and dipole-dipole interactions. They allow manipulation of physical characteristics such as the molecular length to breadth ratio, dipole location and strength, and strength of molecular orientation anisotropy. The aim of calculating a Fourier series modelling these two pair potentials was simply to be able to analyse how varying these molecular parameters would affect the phase behaviour of the liquid crystal materials from which these molecules came. We will see how a pair potential can be approximated to create a free energy in the next Chapter.

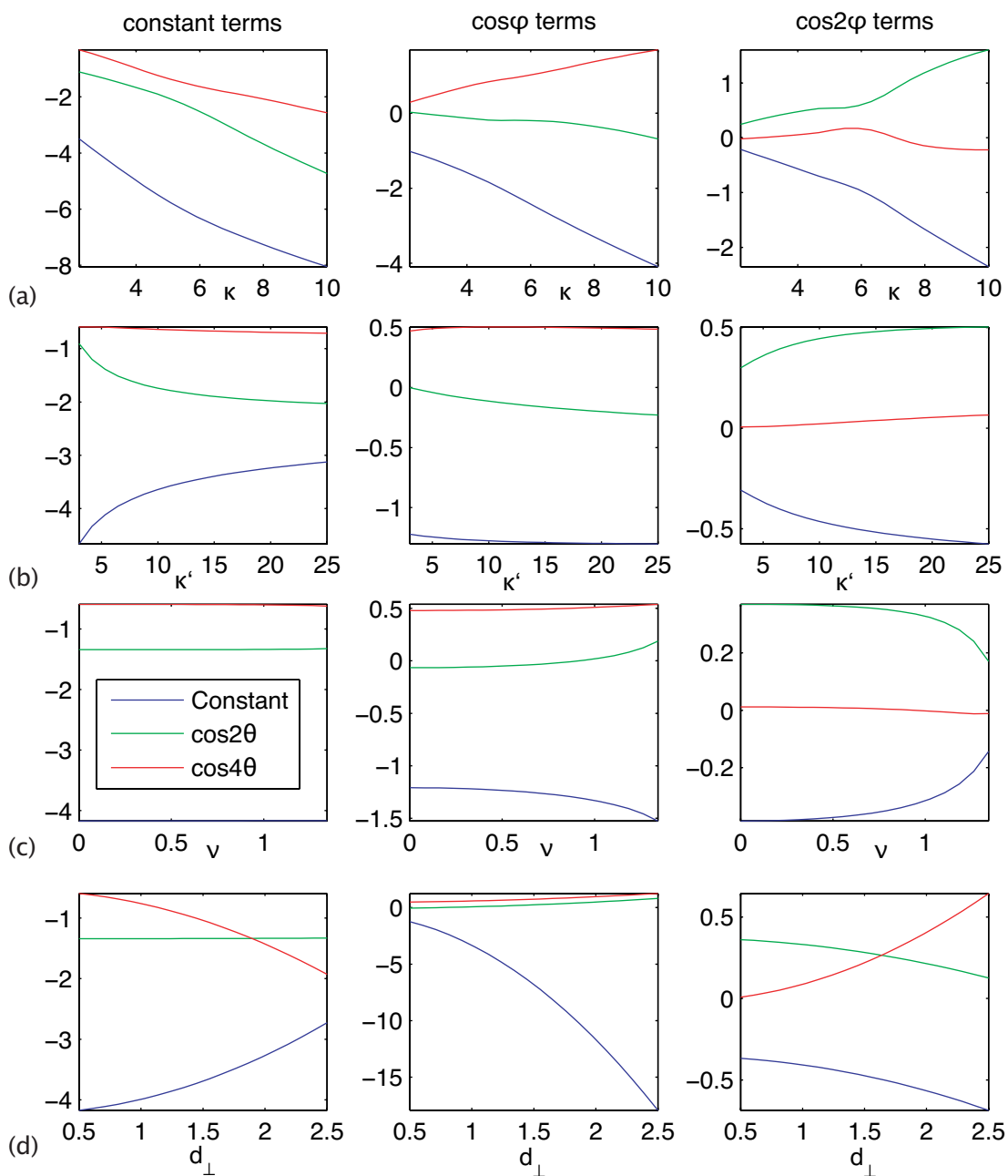


Figure 2.15: The significant general Fourier coefficients are plotted against the molecular parameters: (a) κ , the molecular length-breadth ratio; (b) κ' , the side-side to end-end well-depth ratio; (c) ν , dipole location; and (d) d_{\perp} , dipole strength.

2.2.2 A glimpse at the Maier-Saupe interaction potential

A popular distance independent pair potential used in macroscopic modelling theories is the Maier-Saupe potential derived in 1959 by authors of the same name [39, 40, 41]. Maier and Saupe modelled the dispersion interaction as their intermolecular potential. In the next Chapter we use a simplified dispersion interaction potential derived by Van der Meer [42, 43], see (3.10). The pair-potential potential can be expressed as

$$U_{MS}(\phi, \theta) = b_0 + b_1 \cos^2 \theta + b_2 \cos^4 \theta + b_3 \sin^2 2\theta \cos \phi + b_4 \sin^4 \theta \cos 2\phi, \quad (2.14)$$

where θ is the tilt angle and ϕ is the difference in the azimuthal angles of molecules 1 and 2. The Maier-Saupe coefficients b_i can now be found by performing a Fourier decomposition with the form given above on the combined pair potential. In this instance we would have five independent modes describing the pair potential. Calculating the intermolecular pair potential, $U_{pp}(\mathbf{u}_1, \mathbf{u}_2)$, for a sum of the Gay-Berne and dipole-dipole potentials, and performing a Fourier decomposition with the form given in (2.14) we can equate the Fourier coefficients with the Maier-Saupe coefficients. First we will calculate the coefficients of the ϕ modes, so after the first stage of Fourier decomposition we will express U_{pp} as

$$U_{pp} \approx A_0 + A_1 \cos \phi + A_2 \cos 2\phi \quad (2.15)$$

where A_0 , A_1 , and A_2 are the Fourier coefficients given by

$$A_0 = \frac{1}{2\pi} \int_0^{2\pi} U_{pp} d\phi, \quad A_1 = \frac{1}{\pi} \int_0^{2\pi} U_{pp} \cos \phi d\phi, \quad A_2 = \frac{1}{\pi} \int_0^{2\pi} U_{pp} \cos 2\phi d\phi.$$

When we try to decompose these coefficients further, this time in terms of the θ components, we will have difficulty with A_0 as our desired form contains non-orthogonal components. So to calculate coefficients b_0, b_1, b_2 , we will have to solve the system of equations,

$$\begin{aligned} \int_0^{2\pi} A_0 d\theta &= 2\pi b_0 + \pi b_1 + \frac{3\pi}{4} b_2, \\ \int_0^{2\pi} A_0 \cos^2 \theta d\theta &= \pi b_0 + \frac{3\pi}{4} b_1 + \frac{5\pi}{8} b_2, \\ \int_0^{2\pi} A_0 \cos^4 \theta d\theta &= \frac{3\pi}{4} b_0 + \frac{5\pi}{8} b_1 + \frac{35\pi}{64} b_2. \end{aligned}$$

The decompositions of A_1 and A_2 are more straight forward

$$b_3 = \frac{4}{3\pi} \int_0^{2\pi} A_1 \sin^2 2\theta d\theta, \quad b_4 = \frac{64}{35\pi} \int_0^{2\pi} A_2 \sin^4 \theta d\theta. \quad (2.16)$$

In Figure 2.16, the general Fourier approximation and the Maier-Saupe approxi-

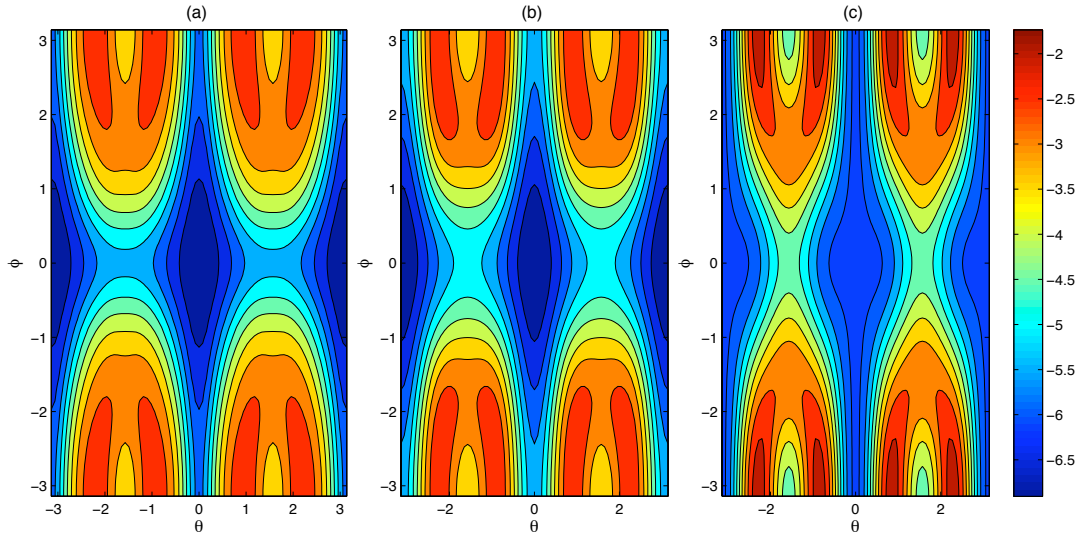


Figure 2.16: (a) the combined pair potential, (b) the general Fourier approximation, and (c) the Maier-Saupe Fourier approximation as functions of ϕ and θ .

mation to the combined pair potential is plotted. We see that both approximations to the interaction energy possess the same symmetry and similar energy levels to the combined pair potential, although the Maier-Saupe has only five independent coefficients as opposed to the nine of the general Fourier decomposition model.

To compare the general Fourier decomposition (2.12, 2.13) to the Maier-Saupe potential we rewrite the Maier-Saupe potential using cosine double angle relations. The modes that are represented by the potential are similar as those chosen during our Fourier analysis of the combined potential.

$$\begin{aligned}
 U_{MS}(\mathbf{u}_1, \mathbf{u}_2) = & c_0 + c_1 \cos 2\theta + c_2 \cos 4\theta + c_3 \cos \phi + c_4 \cos 2\theta \cos \phi + c_5 \cos 4\theta \cos \phi \\
 & + c_6 \cos 2\phi + c_7 \cos 2\theta \cos 2\phi + c_8 \cos 4\theta \cos 2\phi
 \end{aligned} \tag{2.17}$$

where

$$\begin{aligned}
 c_0 = b_0 + \frac{b_1}{2} + \frac{3b_2}{8}, & \quad c_1 = \frac{b_1 + b_2}{2}, & \quad c_2 = \frac{b_2}{8}, \\
 c_3 = \frac{b_3}{2}, & \quad c_4 = 0, & \quad c_5 = -\frac{b_3}{2}, \\
 c_6 = \frac{3b_4}{8}, & \quad c_7 = -\frac{b_4}{2}, & \quad c_8 = \frac{b_4}{8}.
 \end{aligned} \tag{2.18}$$

We see that only one mode, $\cos 2\theta \cos \phi$, is unrepresented, and also that the eight modes are dependent on the five independent coefficients. We repeated our analysis of the model parameters and plot the results in Figure 2.17. We compare the nine coefficients of the general Fourier decomposition of U_{pp} with the equivalent Maier-Saupe coefficients. Excluding the missing $\cos 2\theta \cos \phi$ mode, the Maier-Saupe approximation shows similar dependence on the molecular parameters as the general Fourier approximation. However, the magnitude of the dependence is

not always matched. The Maier-Saupe is least successful at matching the $\cos 2\phi$ terms when varying d_{\perp} , but that may be due to the relative weightings given to

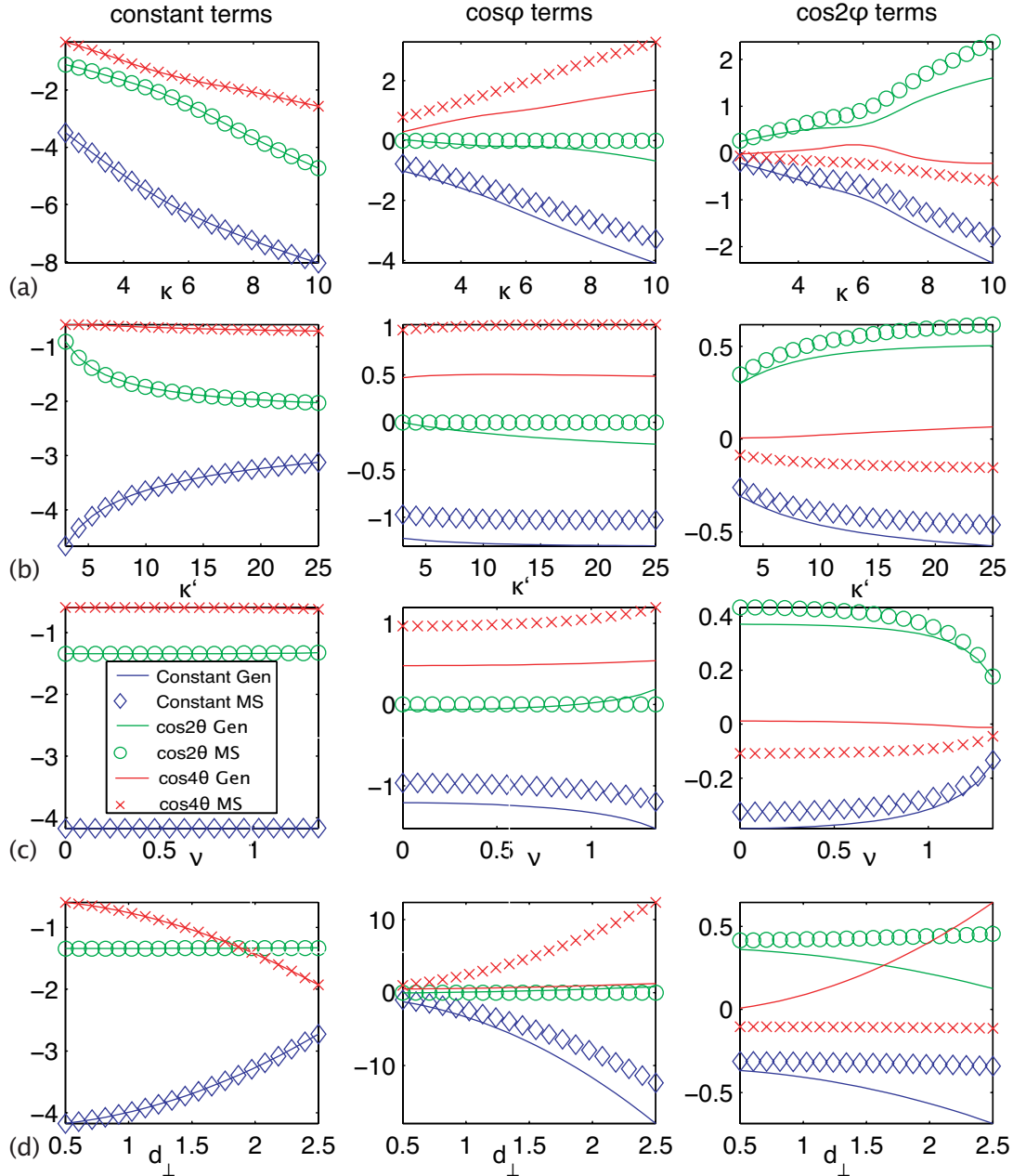


Figure 2.17: The significant general Fourier coefficients (solid lines) and Fourier Maier-Saupe (2.17) coefficients (markers) are plotted against the molecular parameters: (a) κ , the molecular length-breadth ratio; (b) κ' , the side-side to end-end well-depth ratio; (c) ν , dipole location; and (d) d_{\perp} , dipole strength.

the U_{GB} and U_{DD} when combining them. Therefore, the Maier-Saupe potential would be a simpler yet adequate approximation to the pair potential calculated from the combination of the Gay-Berne and dipole-dipole potentials.

In Figure 2.18 we have plotted the coefficients of (2.14) as they vary with the molecular parameters. We fixed the tilt angle θ so the preferred molecular orientation will depend only on the ϕ Fourier modes. The $\cos \phi$ mode aligns the molecules side-side on the smectic cone, $\phi = 0$, when $b_3 < 0$. The $\cos 2\phi$ mode aligns the molecules at opposite sides of the smectic cone, $\phi = \pi$, when $b_4 < 0$. Increasing any of the molecular parameters will cause b_3 to become more negative,

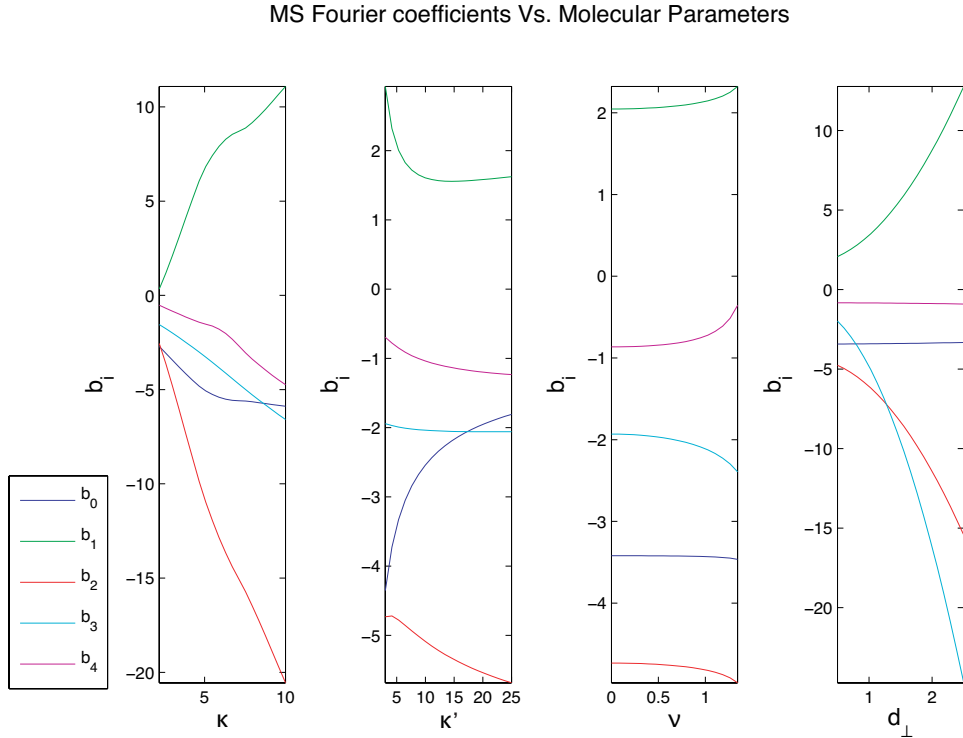


Figure 2.18: The Maier-Saupe coefficients (2.16) are plotted against the molecular parameters: κ , the molecular length-breadth ratio, κ' , the side-side to end-end well-depth ratio, ν , dipole location, and d_{\perp} , dipole strength.

and side-side molecular orientation to be preferred, but κ and d_{\perp} have the most influence. Increasing κ and κ' also increase the preference for the molecules to lie on opposite sides of the smectic cone, but increasing ν decreases end-end packing as the dipoles do not want to move further away from each other. It should be noted that the magnitude of b_3 is always greater than b_4 which tells us that in all of these cases the Maier-Saupe potential will prefer for the molecules to lie side-side on the smectic cone.

2.3 Summary

In this Chapter, we have investigated the Gay-Berne and dipole-dipole intermolecular interaction pair potentials. We have seen how intermolecular position and relative molecular orientation have affected the standard GB(3,5,2,1) potential and an arbitrary dipole-dipole potential ($\nu = 0.6$, $d_{\perp} = 0.5$). We then investigated the effect of the molecular parameters (κ , κ' , ν , d_{\perp}) after the potentials were integrated over the intermolecular vector so that the energy depended on only the relative orientation of the molecules. This set of varied model parameters will be used throughout this thesis as we increase the length-scales of our models. Finally, we used Fourier analysis to find an analytic form of the potentials that depended on the relative molecular orientation. We found that the Maier-Saupe potential was capable of being a reasonable approximation to the combination of the Gay-Berne and dipole-dipole potentials.

In conclusion, it should be possible to create a molecular interaction potential that accounted for short and long range forces. The Gay-Berne potential, modelling the steric effect of the molecules and the van der Waals dispersion force, and the

dipole-dipole potential, modelling the long range force of dipole interactions, can be combined to model these forces effectively. How these potentials are weighted when combined is still to be determined. The Fourier approximation of this combined potential would allow us to calculate coefficients of the Maier-Saupe model from the Gay-Berne and dipole-dipole potentials. This type of approximation allows us to model at length-scales larger than the molecule, and in the next Chapter we look at how the Maier-Saupe theory can be used in this way.

3 The Maier-Saupe approach

3.1 Introduction to the mean-field theory

The goal of the mean-field theory is to reveal the properties and structures of liquid crystals that are responsible for the onset of liquid crystal order at the microscopic level. The mean-field theory depends on the interaction between molecules, but the intermolecular interaction potentials can only be modelled. They are thought to be complex in form as the typical mesogenic molecules are complex. This complexity will complicate the statistical mechanics we wish to perform on our model potentials. Computing capabilities available today do allow us to perform simulations with realistic molecular models but also have their drawbacks. For example, very large systems using thousands of particles are necessary to model even simple systems. As well as computer time consumption, one drawback is the difficulty in relating the macroscopic parameters of liquid phases from empirical data to the features of simulated molecular structures. An accessible review by Osipov [44] covers the basics of molecular theories. In this Chapter we will introduce the intermolecular pair potential used by Maier and Saupe, and the mean-field theory they employed to calculate the free energy of the de Vries system.

3.1.1 The intermolecular interaction potential

The intermolecular interaction potential is desired because the characteristic properties of liquid crystals arise from how the molecules interact with each other. An effective potential should highlight the major qualities and ignore the less

prominent features. An established molecular theory is that of Maier and Saupe [39, 40, 41]. They assumed that the interaction of the anisotropic molecular polarisations were the cause of nematic order. This assumption was founded in the observations that molecules in the nematic state have strongly anisotropic polarisabilities and that the permanent dipoles are not required for the formation of the nematic phase. In thermotropic liquid crystals, where transition between phases depends on temperature, dispersion (van der Waals) interactions must be included in any model potential. Maier and Saupe used an approximation to the dipole-dipole dispersion interaction found from performing second order perturbation theory on the electrostatic interaction as their intermolecular interaction potential.

The dipole-dipole dispersion interaction was simplified by Van der Meer [42, 43] by assuming the short axes of the molecules rotate around the long axis (\mathbf{a}_1) without correlation. Van der Meer therefore averaged the dispersion potential over all short axes resulting in the expression for an effective uniaxial potential,

$$U_{eff} = C - J_{12}^2(\mathbf{a}_1 \cdot \mathbf{r}_{12})^2 - J_{21}^2(\mathbf{a}_2 \cdot \mathbf{r}_{12})^2 - J_{12} [(\mathbf{a}_2 \cdot \mathbf{a}_2) - (\mathbf{a}_1 \cdot \mathbf{r}_{12})(\mathbf{a}_2 \cdot \mathbf{r}_{12})]^2, \quad (3.1)$$

where C is a constant and the J coefficients are in terms of the dipole and quadrupoles. This effective uniaxial potential depends on how two molecules are orientated in relation with each other and in relation to the intermolecular vector \mathbf{r}_{12} . The next step in understanding the thermodynamic properties of the model would be to calculate the free energy associated with this pair potential. This requires summing over all possible pair interactions. Maier and Saupe employed the mean-field approximation to develop a simple usable form of the free energy.

3.1.2 The mean-field approximation and the free energy

The free energy of the system, which consists of the internal energy and entropy, is

$$F = \frac{1}{2}\rho^2 \int \int U(1, 2) f_2(1, 2) d\gamma_1 d\gamma_2 + kT\rho \int \int f_2(1, 2) \ln [f_2(1, 2)] d\gamma_1 d\gamma_2,$$

where $U(1, 2)$ is the interaction potential between molecules 1 and 2, $f_2(1, 2)$ is the pair distribution function of two molecules, γ_i denotes all microscopic variables of molecule i , and ρ is the number density of molecules in the system. Integration is over all pairs of molecules [44]. The mean-field approximation ignores all direct correlations between different molecules and replaces them with an average internal field experienced by each molecule. In statistical mechanics this means that the pair distribution is replaced by the product of two one-particle orientational distributions, that is $f_2(1, 2) = f_1(1)f_1(2)$.

This gives a free energy for the system,

$$F = \frac{1}{2}\rho^2 \int \int U(1, 2) f_1(1) f_1(2) d\gamma_1 d\gamma_2 + kT\rho \int f_1(1) \ln [f_1(1)] d\gamma_1, \quad (3.2)$$

where the mean-field interaction potential can now be defined as

$$U_{MF} = \rho \int U(1, 2) f_1(2) d\gamma_2. \quad (3.3)$$

Minimising the expression for the mean-field free energy (3.2) gives

$$f(\gamma_i) = \frac{1}{Z} e^{(-\frac{1}{kT} U_{MF}(\gamma_i))}, \quad (3.4)$$

$$\text{where } Z = \int e^{(-\frac{1}{kT} U_{MF}(\gamma_i))} d\gamma_i, \quad (3.5)$$

and substituting (3.4) into (3.2),

$$\begin{aligned} F &= \frac{1}{2}\rho \int U_{MF} f(\gamma_1) d\gamma_1 + kT\rho \int f(\gamma_1) \ln \left[\frac{1}{Z} e^{(-\frac{1}{kT} U_{MF}(\gamma_1))} \right] d\gamma_1 \\ &= \frac{1}{2}\rho \int U_{MF} f(\gamma_1) d\gamma_1 + kT\rho \int f(\gamma_1) \left[-\frac{1}{kT} U_{MF}(\gamma_1) - \ln Z \right] d\gamma_1 \\ &= -\frac{1}{2}\rho \int U_{MF} f(\gamma_1) d\gamma_1 - kT\rho \ln Z. \end{aligned} \quad (3.6)$$

Although Maier and Saupe devised this theory for the nematic phase equations (3.4) and (3.5) are not restricted to this phase. The one-point distribution function depends on the relative position \mathbf{r}_{12} so it can be used to describe smectic molecular distributions.

Unlike the Gay-Berne potential from the previous Chapter the Maier-Saupe theory enables us to construct a pair interaction potential from the dispersion interaction energy in such a form that we can analyse its characteristics. We can also use a mean-field approximation to find a free energy on which we can perform analysis. This analysis is covered in the following sections of this Chapter.

3.2 Construction of a mean-field model for de Vries Sm C

Our molecules exist in the 3-d space (x, y, z) . The average molecular long axis is the director, \mathbf{n} and is nonpolar so $\mathbf{n} \equiv -\mathbf{n}$. We define the molecular long axis as \mathbf{a}_i , the molecular short axis, perpendicular to the tilt plane, as \mathbf{b}_i . The spontaneous polarisation dipole μ is parallel to \mathbf{b}_i . The function describing the distribution of molecules on the cone $f = f(\mathbf{a}_i)$ is assumed to be symmetric about the mean azimuth angle $\bar{\phi}$, and $\int f d\mathbf{a} = 1$. We assume a symmetric distribution around the cone and a fixed tilt angle to model a de Vries smectic.

Using the molecular long axis we describe the molecules, see Figure (3.1),

$$\mathbf{a}_i = \mathbf{i} \sin \theta_0 \cos \phi_i + \mathbf{j} \sin \theta_0 \sin \phi_i + \mathbf{k} \tau_i \cos \theta_0. \quad (3.7)$$

\mathbf{k} is the unit vector in the \mathbf{z} direction, which is the smectic layer normal. Since the director $\mathbf{n} \equiv -\mathbf{n}$ the states (θ_0, ϕ) and $(\pi + \theta_0, \pi + \phi)$ must be equivalent. In order for $\mathbf{a}(\theta_0, \phi_i) = \mathbf{a}(\pi + \theta_0, \pi + \phi_i)$ then we must introduce a new variable $\tau_i = \pm 1$ which distinguishes between the two molecules \mathbf{a}_1 and $-\mathbf{a}_1$. In this way we need only consider $0 \leq \theta_0 \leq \frac{\pi}{2}$, $-\pi < \phi_i \leq \pi$, and $\tau_i = \pm 1$.

The interaction of two molecules will depend on their displacement from one another. If we assume all molecules are contained in a single layer then the displacement vector of two molecules' centres-of-mass (c.o.m.) is given by

$$\mathbf{r}_{12} = (\cos \psi, \sin \psi, 0), \quad (3.8)$$

where ψ is the angle of the displacement vector from the x axis. We also assume

that the c.o.m. are placed randomly so ψ has a uniform probability function.

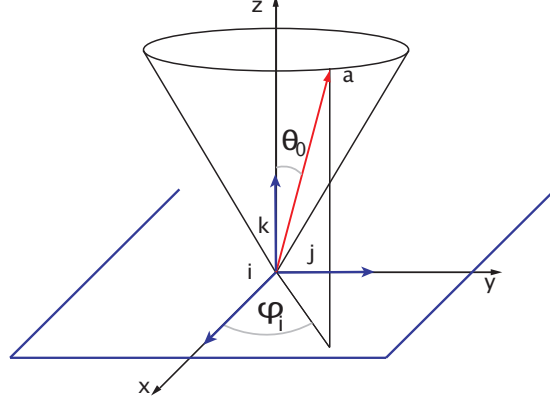


Figure 3.1: Geometry of model. \mathbf{i} , \mathbf{j} , and \mathbf{k} are unit vectors, \mathbf{a}_i is the molecular long axis, θ_0 is the cone tilt angle, and ϕ_i is the azimuthal angle.

3.2.1 Calculating the Maier-Saupe pair potential

Analysis of the free energy using a pair potential calculated from the sum of the GB and DD potentials would be impossible due to the lack of analytic form. Let us instead use an interaction potential with a more manageable functional form and the Fourier analysis discussed in Chapter 2 to combine the two approaches.

Van der Meer's version of the effective interaction potential (3.1) describes the electrostatic dispersion interactions between the molecules labelled 1 and 2. The effective interaction potential is a function of molecules ($\mathbf{a}_1, \mathbf{a}_2$), the displacement vector between the centre-of-mass (c.o.m) of the two molecules (\mathbf{r}_{12}), and the material dependent constants, J_s .

$$U_{eff}(\mathbf{a}_1, \mathbf{a}_2, \mathbf{r}_{12}) = J_0 - J_1(\mathbf{a}_1 \cdot \mathbf{a}_2)^2 + 2J_2(\mathbf{a}_1 \cdot \mathbf{a}_2)(\mathbf{a}_1 \cdot \mathbf{r}_{12})(\mathbf{a}_2 \cdot \mathbf{r}_{12}) - J_3(\mathbf{a}_1 \cdot \mathbf{r}_{12})^2(\mathbf{a}_2 \cdot \mathbf{r}_{12})^2 - J_{12}^2(\mathbf{a}_1 \cdot \mathbf{r}_{12})^2 - J_{21}^2(\mathbf{a}_2 \cdot \mathbf{r}_{12})^2, \quad (3.9)$$

where, as stated previously in equations (3.7) and (3.8),

$$\begin{aligned}\mathbf{a}_1 &= (\sin \theta_0 \cos \phi_i, \sin \theta_0 \sin \phi_i, \tau_i \cos \theta_0), \\ \mathbf{r}_{12} &= (\cos \psi, \sin \psi, 0),\end{aligned}$$

and we assume that all molecules lie on a cone with angle θ_0 . To calculate the pair potential we then integrate the two particle potential over \mathbf{r}_{12} . The working is given in appendix A. We can rewrite (3.9) as

$$\begin{aligned}U_{MS}(\mathbf{a}_1, \mathbf{a}_2) &= b_0 + b_1 \cos^2 \theta_0 + b_2 \cos^4 \theta_0 + b_3 \tau_1 \tau_2 \sin^2 2\theta_0 \cos(\phi_1 - \phi_2) \\ &\quad + b_4 \sin^4 \theta_0 \cos 2(\phi_1 - \phi_2).\end{aligned}\tag{3.10}$$

We define the coefficients of the trigonometric functions as:

$$\begin{aligned}b_0 &= \frac{\pi}{2} [4J_0 - 2J_1 + 2J_2 - J_3 - 2(J_{12}^2 + J_{21}^2)], \\ b_1 &= \pi [2J_1 - 2J_2 + J_3 + (J_{12}^2 + J_{21}^2)], \\ b_2 &= \frac{\pi}{2} [-6J_1 + 2J_2 - J_3], \\ b_3 &= \frac{\pi}{2} [-2J_1 + J_2], \\ b_4 &= \frac{\pi}{4} [-4J_1 + 4J_2 - J_3].\end{aligned}\tag{3.11}$$

and the b_i coefficients coincide with the definition in (3.9).

3.2.2 Analysis of U_{MS}

Analysing the intermolecular interaction potential we hope to find the molecular parameters that minimise the energy. Substituting $\phi = \phi_1 - \phi_2$ we differentiate (3.10) to determine when U_{MS} is minimised with respect to ϕ , the relative orientation,

$$\frac{\partial U_{MS}}{\partial \phi} = (-4b_3\tau_1\tau_2 \sin^2 \theta_0 \cos^2 \theta_0 - 4b_4 \sin^4 \theta_0 \cos \phi) \sin \phi.$$

So
$$\frac{\partial U_{MS}}{\partial \phi} = 0 \text{ when } \sin \phi = 0 \text{ or } \cos \phi = -\frac{b_3\tau_1\tau_2}{b_4 \tan^2 \theta_0},$$

ie. when
$$\phi = 0, \pi, \text{ or } \phi = \cos^{-1} \left(-\frac{b_3\tau_1\tau_2}{b_4 \tan^2 \theta_0} \right) \text{ when } \left| \frac{b_3}{b_4} \right| \leq \tan^2 \theta_0.$$

Looking at the second derivative we can establish the stability of the solutions.

Case (i) $\phi = 0$

$$\frac{\partial^2 U_{MS}}{\partial \phi^2} = -4b_3\tau_1\tau_2 \sin^2 \theta_0 \cos^2 \theta_0 - 4b_4 \sin^4 \theta_0,$$

minimum when
$$-\frac{b_3\tau_1\tau_2}{b_4} < \tan^2 \theta_0,$$

maximum when
$$-\frac{b_3\tau_1\tau_2}{b_4} > \tan^2 \theta_0.$$

Case (ii) $\phi = \pi$

$$\frac{\partial^2 U_{MS}}{\partial \phi^2} = 4b_3\tau_1\tau_2 \sin^2 \theta_0 \cos^2 \theta_0 - 4b_4 \sin^4 \theta_0,$$

minimum when
$$\frac{b_3\tau_1\tau_2}{b_4} < \tan^2 \theta_0,$$

maximum when
$$\frac{b_3\tau_1\tau_2}{b_4} > \tan^2 \theta_0.$$

Case (iii) $\phi = \cos^{-1} \left(-\frac{b_3}{b_4} \tau_1 \tau_2 \cot^2 \theta_0 \right)$, $\left| \frac{b_3}{b_4} \right| \leq \tan^2 \theta_0$

$$\frac{\partial^2 U_{MS}}{\partial \phi^2} = -\frac{4b_3^2}{b_4} \cos^4 \theta_0 + 4b_4 \sin^4 \theta_0,$$

minimum when $\frac{b_3}{b_4} > \tan^2 \theta_0$,

maximum when $\frac{b_3}{b_4} < \tan^2 \theta_0$.

Case (iii) is complex when $\left| \frac{b_3}{b_4} \right| > \tan^2 \theta_0$, so it is only real as a maximum. Cases (i) and (ii) describe two possible molecular orientations: two molecules at opposite sides of the smectic cone $[(\phi = 0, \tau_1 \neq \tau_2), (\phi = \pi, \tau_1 = \tau_2)]$, and two molecules aligned on the smectic cone $[(\phi = 0, \tau_1 = \tau_2), (\phi = \pi, \tau_1 \neq \tau_2)]$, see figure (3.2). This means that we have two possible molecular orientations that locally minimise the interaction potential. When $\frac{b_3}{b_4} > \tan^2 \theta_0$, the interaction energy is minimised when the two molecules align on the smectic cone, and when $\frac{b_3}{b_4} < \tan^2 \theta_0$ the interaction energy is minimised when the molecules align side by side or opposite on the smectic cone.

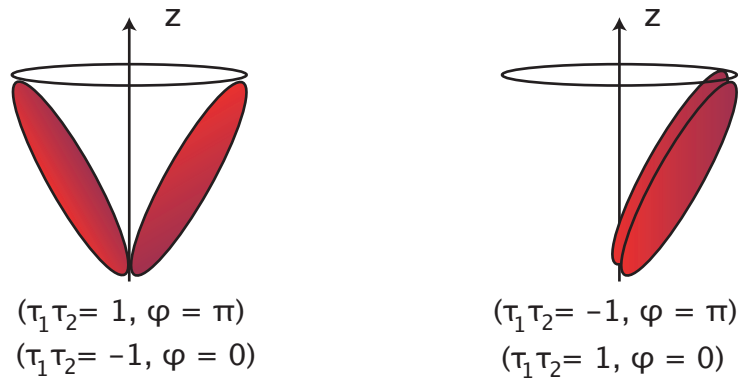


Figure 3.2: Diagram of preferred orientations in the mean-field interaction potential. The two molecules lying at opposite sides of smectic cone will create the smectic A biaxial phase, the director is along the smectic normal but now appears biaxial. The two molecules side-by-side on the smectic cone will create the smectic C phase, the director will be tilted and biaxial.

3.2.3 Mean-field interaction potential U_{MF} without an external electric field

In section 3.2.1 we calculated the Maier-Saupe interaction pair potential which we now use to calculate the mean-field interaction potential as defined in (3.3). This will calculate U_{MF} which the one-particle distribution function (3.4) depends on. Once we have calculated U_{MF} we can calculate an analytic form for the free energy (3.6). We split (3.10) into three parts: $U_{MF(i)}$ the constant component, $U_{MF(ii)}$ the $\cos(\phi_1 - \phi_2)$ component, and $U_{MF(iii)}$ the $\cos 2(\phi_1 - \phi_2)$ component. The constant component will be unaffected due to the properties of the distribution function,

$$\begin{aligned} U_{MF(i)} &= \rho \sum_{\tau_2=-1,1} \int_{-\pi}^{\pi} [b_0 + b_1 \cos^2 \theta_0 + b_2 \cos^4 \theta_0] f(\phi_2, \tau_2) d\phi_2, \\ &= \rho [b_0 + b_1 \cos^2 \theta_0 + b_2 \cos^4 \theta_0]. \end{aligned} \quad (3.12)$$

Next we consider the $\cos(\phi_1 - \phi_2)$ term in (3.10),

$$U_{MF(ii)} = \rho \sum_{\tau_2=-1,1} \int_{-\pi}^{\pi} b_3 \tau_1 \tau_2 \sin^2 2\theta_0 \cos(\phi_1 - \phi_2) f(\phi_2, \tau_2) d\phi_2.$$

We will rewrite

$$\begin{aligned} \cos(\phi_1 - \phi_2) &= \cos((\phi_1 - \bar{\phi}) - (\phi_2 - \bar{\phi})) \\ &= \cos(\phi_1 - \bar{\phi}) \cos(\phi_2 - \bar{\phi}) + \sin(\phi_1 - \bar{\phi}) \sin(\phi_2 - \bar{\phi}), \end{aligned}$$

where $\bar{\phi}$ is the mean of the distribution function. The distribution of $f(\phi_2, \tau_2)$ is symmetric about $\bar{\phi}$ and $\sin(\phi_2 - \bar{\phi})$ is an odd function about $\bar{\phi}$. Therefore,

$$\begin{aligned} \int_{-\pi}^{\pi} \sin(\phi_2 - \bar{\phi}) f(\phi_2, \tau_2) d\phi_2 &= \int_{\bar{\phi}}^{\pi} \sin(\phi_2 - \bar{\phi}) f(\phi_2, \tau_2) d\phi_2 + \int_{-\pi}^{\bar{\phi}} \sin(\phi_2 - \bar{\phi}) f(\phi_2, \tau_2) d\phi_2 \\ &= \int_{\bar{\phi}}^{\pi} \sin(\phi_2 - \bar{\phi}) f(\phi_2, \tau_2) d\phi_2 + \int_{-\pi}^{-\pi+\bar{\phi}} \sin(\phi_2 - \bar{\phi}) f(\phi_2, \tau_2) d\phi_2 \\ &\quad + \int_{-\pi+\bar{\phi}}^{\bar{\phi}} \sin(\phi_2 - \bar{\phi}) f(\phi_2, \tau_2) d\phi_2 \\ &= \int_{\bar{\phi}}^{\pi+\bar{\phi}} \sin(\phi_2 - \bar{\phi}) f(\phi_2, \tau_2) d\phi_2 + \int_{-\pi+\bar{\phi}}^{\bar{\phi}} \sin(\phi_2 - \bar{\phi}) f(\phi_2, \tau_2) d\phi_2 \end{aligned}$$

since $\phi_2 = \pi$ and $\phi_2 = -\pi$ are equivalent. So we have

$$\int_{-\pi}^{\pi} \sin(\phi_2 - \bar{\phi}) f(\phi_2, \tau_2) d\phi_2 = \int_{-\pi+\bar{\phi}}^{\pi+\bar{\phi}} \sin(\phi_2 - \bar{\phi}) f(\phi_2, \tau_2) d\phi_2 = 0 \quad (3.13)$$

since f is even and $\sin(\phi_2 - \bar{\phi})$ is odd about $\phi_2 = \bar{\phi}$. Therefore,

$$U_{MF(ii)} = b_3 \rho \sin^2 2\theta_0 \tau_1 \cos(\phi_1 - \bar{\phi}) V, \quad (3.14)$$

where we define

$$V = \sum_{\tau_2=-1,1} \int_{-\pi}^{\pi} \tau_2 \cos(\phi_2 - \bar{\phi}) f(\phi_2, \tau_2) d\phi_2. \quad (3.15)$$

Finally, we integrate the $\cos 2(\phi_1 - \phi_2)$ term in (3.10),

$$U_{MF(iii)} = \rho \sum_{\tau_2=-1,1} \int_{-\pi}^{\pi} b_4 \sin^4 \theta_0 \cos 2(\phi_1 - \phi_2) f(\phi_2, \tau_2) d\phi_2.$$

Using the same approach used to calculate (3.14) we rewrite

$$\begin{aligned}\cos 2(\phi_1 - \phi_2) &= \cos(2(\phi_1 - \bar{\phi}) - 2(\phi_2 - \bar{\phi})), \\ &= \cos 2(\phi_1 - \bar{\phi}) \cos 2(\phi_2 - \bar{\phi}) + \sin 2(\phi_1 - \bar{\phi}) \sin 2(\phi_2 - \bar{\phi}),\end{aligned}$$

which results in

$$U_{MF(iii)} = b_4 \rho \sin^4 \theta_0 \cos 2(\phi_1 - \bar{\phi}) B, \quad (3.16)$$

where we define

$$B = \sum_{\tau_2=-1,1} \int_{-\pi}^{\pi} \cos 2(\phi_2 - \bar{\phi}) f(\phi_2, \tau_2) d\phi_2. \quad (3.17)$$

Gathering (3.12), (3.14), and (3.16), the expression for the mean-field potential is then

$$\begin{aligned}U_{MF} &= \rho [b_0 + b_1 \cos^2 \theta_0 + b_2 \cos^4 \theta_0] + b_3 \rho \sin^2 2\theta_0 \tau_1 \cos(\phi_1 - \bar{\phi}) V \\ &\quad + b_4 \rho \sin^4 \theta_0 \cos 2(\phi_1 - \bar{\phi}) B,\end{aligned} \quad (3.18)$$

where ρ is the number density, the b s are defined in (3.11). The parameters B and V are order parameters. When B and V are zero the uniform distribution of the molecules around the smectic cone gives a director with zero tilt angle. When B is non zero the smectic cone appears biaxial and has a director with zero tilt angle. When V is non zero, B is non zero and the smectic cone has a tilted director and appears biaxial.

3.2.4 Model with external electric field

We assume that the spontaneous polarisation, μ , of a molecule is parallel to the molecular short axis \mathbf{b} . Assuming that \mathbf{b} is always normal to the instant tilt plane we have

$$\mathbf{b} = -\frac{\mathbf{k} \times \mathbf{a}}{|\mathbf{k} \times \mathbf{a}|} = \sin \phi \mathbf{i} - \cos \phi \mathbf{j},$$

which gives an expression for the spontaneous polarisation vector $\mu = \mu_0 \tau (\sin \phi \mathbf{i} - \cos \phi \mathbf{j})$, where μ_0 is the polarisation specific to the material and τ maintains the nonpolar property of the molecular distribution.

The contribution to the energy of interaction with the field $\mathbf{E} = (E_x, E_y, E_z)$ is

$$\mu \cdot \mathbf{E} = \mu_0 \tau (E_x \sin \phi - E_y \cos \phi),$$

giving an interaction potential of

$$\begin{aligned} U_{MF} = & \rho [b_0 + b_1 \cos^2 \theta_0 + b_2 \cos^4 \theta_0] + b_3 \rho \sin^2 2\theta_0 \tau_1 \cos(\phi_1 - \bar{\phi}) V \\ & + b_4 \rho \sin^4 \theta_0 \cos 2(\phi_1 - \bar{\phi}) B + \mu_0 \tau (E_x \sin \phi - E_y \cos \phi). \end{aligned} \quad (3.19)$$

We now have an expression for the mean-field interaction potential that we can use to calculate the free energy of our system. Minimising the free energy of the system will give us the order parameters (B, V) for a specific temperature and set of model parameters.

3.3 Free energy

3.3.1 Approximating the mean-field free energy

The mean-field free energy is

$$F = -\frac{1}{2}\rho \sum_{\tau_1=-1,1} \int_{-\pi}^{\pi} U_{MF} f(\phi_1, \tau_1) d\phi_1 - kT\rho \ln Z, \quad (3.20)$$

$$\text{where } Z = \sum_{\tau_1=-1,1} \int_{-\pi}^{\pi} e^{(-\frac{1}{kT}U_{MF}(\phi_1, \tau_1))} d\phi_1.$$

The mean-field interaction potential (3.19) was calculated previously but we will re-express it as a function of (τ_1, ϕ_1) to reduce working,

$$U_{MF} = D_0 + D_1\tau_1 \cos(\phi_1 - \bar{\phi})V + D_2 \cos 2(\phi_1 - \bar{\phi})B + \mu_0\tau_1(E_x \sin \phi - E_y \cos \phi), \quad (3.21)$$

where we define the coefficients of the mean-field potential as

$$D_0 = \rho(b_0 + b_1 \cos^2 \theta_0 + b_2 \cos^4 \theta_0), \quad D_1 = \rho b_3 \sin^2 2\theta_0, \quad D_2 = \rho b_4 \sin^4 \theta_0. \quad (3.22)$$

We can now calculate the free energy analytically. The first term of (3.20) is straightforward,

$$-\frac{1}{2}\rho \sum_{\tau_1=-1,1} \int_{-\pi}^{\pi} U_{MF} f(\phi_1, \tau_1) d\phi_1 = -\frac{1}{2}\rho (D_0 + D_1V^2 + D_2B^2)$$

$$-\frac{1}{2}\rho \sum_{\tau_1=-1,1} \int_{-\pi}^{\pi} \mu_0\tau_1(E_x \sin \phi - E_y \cos \phi) f(\phi_1, \tau_1) d\phi_1. \quad (3.23)$$

The last term in (3.23) can be split in two and integrated separately. First we use the trigonometric double angle formula,

$$\begin{aligned}\sin \phi &= \cos \bar{\phi} \sin(\phi - \bar{\phi}) + \sin \bar{\phi} \cos(\phi - \bar{\phi}), \\ \cos \phi &= \cos \bar{\phi} \cos(\phi - \bar{\phi}) - \sin \bar{\phi} \sin(\phi - \bar{\phi}),\end{aligned}$$

and (3.13),(3.15) to find

$$\begin{aligned}-\frac{1}{2}\rho \sum_{\tau_1=-1,1} \int_{-\pi}^{\pi} \mu_0 \tau_1 (E_x \sin \phi - E_y \cos \phi) f(\phi_1, \tau_1) d\phi_1 \\ = -\frac{1}{2}\rho \mu_0 (E_x \sin \bar{\phi} - E_y \cos \bar{\phi}) V.\end{aligned}$$

Therefore the first term of (3.20) is

$$-\frac{1}{2}\rho \sum_{\tau_1=-1,1} \int_{-\pi}^{\pi} U_{MF} f(\phi_1, \tau_1) d\phi_1 = -\frac{1}{2}\rho (D_0 + D_1 V^2 + D_2 B^2 + \mu_0 (E_x \sin \bar{\phi} - E_y \cos \bar{\phi}) V). \quad (3.24)$$

Next we will calculate the last term of (3.20) by first approximating the exponential term in Z assuming that B, V, E_x , and E_y are small. We truncate the Taylor approximation about $(B = V = E_x = E_y = 0)$ after order 2,

$$\begin{aligned}e^{(-\frac{1}{kT} U_{MF}(\phi_1, \tau_1))} \\ = e^{-\frac{D_0}{kT}} - \frac{e^{-\frac{D_0}{kT}}}{kT} (D_1 \tau_1 \cos(\phi_1 - \bar{\phi}) V + D_2 \cos 2(\phi_1 - \bar{\phi}) B + \mu \tau_1 (E_x \sin \phi_1 - E_y \cos \phi_1)) \\ + \frac{e^{-\frac{D_0}{kT}}}{2k^2 T^2} (D_1 \tau_1 \cos(\phi_1 - \bar{\phi}) V + D_2 \cos 2(\phi_1 - \bar{\phi}) B + \mu \tau_1 (E_x \sin \phi_1 - E_y \cos \phi_1))^2.\end{aligned}$$

Now we perform the integration over ϕ_1 and τ_1 ,

$$Z = \frac{\pi e^{-\frac{D_0}{kT}}}{2k^2T^2} (4k^2T^2 + \mu^2(E_x^2 + E_y^2) + 2D_1\mu(E_x \sin \bar{\phi}_1 - E_y \cos \bar{\phi}_1)V) \\ + \frac{\pi e^{-\frac{D_0}{kT}}}{2k^2T^2} (D_1^2V^2 + D_2^2B^2).$$

The last step is now to approximate $\ln Z$. Given our assumptions that that B, V, E_x , and E_y are small we can use the Taylor expansion for logarithms. We again truncate the Taylor approximation ($B = V = E_x = E_y = 0$) after order 2,

$$-kT\rho \ln Z = -\frac{\rho}{4kT}(D_1^2V^2 + D_2^2B^2 + 2D_1\mu(E_x \sin \bar{\phi} - E_y \cos \bar{\phi})) \\ - \frac{\rho}{4kT}(8k^2T^2 \ln 2 + 4k^2T^2 \ln \pi - 4kTD_0 + \mu^2(E_x^2 + E_y^2)). \quad (3.25)$$

The truncated second order Taylor approximation to (3.20), using (3.24, 3.25), is

$$F = -\frac{\rho}{4kT} [(2kTD_1 + D_1^2)V^2 + (2kTD_2 + D_2^2)B^2] \\ - \frac{\rho}{2kT}\mu(1 + D_1)(E_x \sin \bar{\phi} - E_y \cos \bar{\phi})V \\ - \frac{\rho D_0}{2} - \rho kT(2 \ln 2 + \ln \pi) - \frac{\rho \mu^2}{4kT}(E_x^2 + E_y^2). \quad (3.26)$$

We could now perform some analysis on the approximation of the free energy to learn more about the dependence of the order parameters on temperature. However, as the approximation is only to the second order the information we could learn would be rather limited. Instead, we can follow the same steps but

truncate the free energy approximation at fourth order and assume $\mathbf{E} = 0$,

$$\begin{aligned}
F &= \frac{\rho}{64k^3T^3}(D_1^4V^4 + D_2^4B^4) \\
&+ \frac{\rho}{8k^2T^2}(D_1^2D_2B - 2kTD_1^2 - 4k^2T^2D_1)V^2 \\
&- \frac{\rho}{4kT}(2kTD_2 + D_2^2)B^2 \\
&- \frac{\rho D_0}{2} - \rho kT(2 \ln 2 + \ln \pi), \tag{3.27}
\end{aligned}$$

which will provide more information when we perform the analysis due to the higher powers of B and V .

3.3.2 Analysis of approximated free energy

The free energy is expressed as an expansion in the order parameters B and V , and we can now minimise the free energy with respect to these two parameters. This will enable us to plot phase diagrams which will tell us what phases are possible in the model. If we consider possible extrema of the free energy (3.27) we need to investigate,

$$\frac{\partial F}{\partial V} = \frac{\rho}{16k^3T^3}D_1^4V^3 + \frac{\rho}{4k^2T^2}(D_1^2D_2B - 2kTD_1^2 - 4k^2T^2D_1)V = 0, \tag{3.28}$$

$$\frac{\partial F}{\partial B} = \frac{\rho}{16k^3T^3}D_2^4B^3 + \frac{\rho}{8k^2T^2}D_1^2D_2V^2 - \frac{\rho}{2kT}(2kTD_2 + D_2^2)B = 0. \tag{3.29}$$

Solutions of (3.28) are

$$V = 0 \quad \text{or} \quad V = \pm \frac{2}{D_1^2} \sqrt{-D_1(D_1D_2B - 2D_1kT - 4k^2T^2)kT}. \tag{3.30}$$

If $V = 0$ (3.29) gives three possible solutions for B ,

$$B = 0 \quad \text{or} \quad B = \pm \frac{2kT}{D_2^2} \sqrt{2D_2(2kT + D_2)}. \quad (3.31)$$

If $V^2 = -\frac{4}{D_1^3} (D_1 D_2 B - 2D_1 kT - 4k^2 T^2) kT$ then (3.29) becomes

$$\frac{\partial F}{\partial B} = \frac{\rho}{16k^3 T^3} D_2^4 B^3 - \frac{\rho}{kT} (kT D_2 + D^2) B + \frac{\rho D_2}{D_1} (D_1 + 2kT) = 0, \quad (3.32)$$

which has three solutions (B_1, B_2, B_3) . So possible phases are therefore

- (1) $V = 0, B = 0,$
- (2) $V = 0, B = \pm \frac{2kT}{D_2^2} \sqrt{2D_2(2kT + D_2)},$
- (3) $V = \pm \frac{2}{D_1^2} \sqrt{-D_1(D_1 D_2 B - 2D_1 kT - 4k^2 T^2) kT}, B = B_1, B_2, B_3.$

The stability of these phases can be investigated by looking at

$$\Delta = \frac{\partial^2 F}{\partial V^2} \frac{\partial^2 F}{\partial B^2} - \left(\frac{\partial^2 F}{\partial V \partial B} \right)^2. \quad (3.33)$$

- (1) $V = 0, B = 0$

$$\begin{aligned} \Delta &= \rho^2 D_1 D_2 \left(\frac{D_1}{2kT} + 1 \right) \left(\frac{D_2}{2kT} + 1 \right). \\ \Delta > 0 &\quad \text{if} \quad \left(\frac{D_1}{2kT} + 1 \right) > 0 \quad \text{and} \quad \left(\frac{D_2}{2kT} + 1 \right) > 0 \quad \mathbf{MIN} \\ &\quad \text{or} \quad \left(\frac{D_1}{2kT} + 1 \right) < 0 \quad \text{and} \quad \left(\frac{D_2}{2kT} + 1 \right) < 0 \quad \mathbf{MAX} \end{aligned} \quad (3.34)$$

The phase $V = 0, B = 0$ will therefore be a minimum when $T > -\frac{D_1}{2k}$ and $T > -\frac{D_2}{2k}$, and a maximum when $T < -\frac{D_1}{2k}$ and $T < -\frac{D_2}{2k}$.

$$(2) V = 0, B = \pm \frac{2kT}{D_2} \sqrt{2D_2(2kT + D_2)}$$

$$\Delta = \underbrace{\left(\pm \frac{\rho D_1^2}{2kT D_2} \sqrt{2D_2(2kT + D_2)} - \frac{\rho D_1^2}{2kT} - \rho D_1 \right)}_{F_1 = \frac{\partial^2 F}{\partial V^2}} \underbrace{\left(\frac{3\rho}{2kT} D_2(2kT + D_2) - \frac{\rho D_2^2}{2kT} - \rho D_2 \right)}_{F_2 = \frac{\partial^2 F}{\partial B^2}}.$$

The \pm sign denotes usage of $\pm B$ to calculate Δ . From (2) we know the phase $V = 0, B \neq 0$ will only be real when $T < -\frac{D_2}{2k}$. The phase $V = 0, B \neq 0$ will be a maximum when $F_1 < 0$ and $F_2 < 0$, and a minimum when $F_1 > 0$ and $F_2 > 0$. Solving $\Delta_2 = 0$ for T gives the transition temperatures

$$T_{F_1} = \frac{D_1}{4kD_2} \left(2(D_1 - D_2) \pm \sqrt{(2(D_1 - D_2))^2 + 4D_2^2} \right),$$

$$T_{F_2} = -\frac{D_2}{2k}.$$

These critical temperatures tell us when F_1 and F_2 switch sign. It is useful to know where these temperatures are in relation to one another. The square root term in T_{F_1} is always positive, so we have $T_{F_1}^- < T_{F_1}^+$. As we stated, the phase will not exist above T_{F_2} so we will check to see whether $T_{F_2} > T_{F_1}^+$,

$$\begin{aligned} T_{F_2} - T_{F_1}^+ &= -\frac{D_2}{2k} - \frac{D_1}{4kD_2} \left(2(D_1 - D_2) + \sqrt{(2(D_1 - D_2))^2 + 4D_2^2} \right) \\ &= -\frac{1}{4kD_2} \left(2D_1^2 - 2D_2^2 - 2D_1D_2 + D_1 \sqrt{(2(D_1 - D_2))^2 + 4D_2^2} \right) \\ &= -\frac{1}{4kD_2} \left(D_1 + \frac{1}{4} \sqrt{(2(D_1 - D_2))^2 + 4D_2^2} \right)^2 > 0, \end{aligned}$$

provided $D_2 < 0$. The transition temperatures are thus ordered $T_{F_1}^- < T_{F_1}^+ < T_{F_2}$. As we have ordered the transition temperatures we will also investigate what signs F_1 and F_2 take as temperature goes to infinity,

$$\begin{aligned} \text{as } T \rightarrow \infty \quad F_1 &\rightarrow -\rho D_1 > 0, \\ F_2 &\rightarrow 2\rho D_2 < 0, \end{aligned}$$

given the existence condition of $\frac{D_1}{D_2} > 0$ and the assumption $D_2 < 0$. Therefore F_1 will be negative between $(T_{F_1}^-, T_{F_1}^+)$ and positive at all other temperatures, and F_2 will be positive below T_{F_2} . The phase $V = 0, B \neq 0$ will therefore be a minimum of the energy below T_{F_2} , except between $(T_{F_1}^-, T_{F_1}^+)$ where it will be a saddle point.

$$(3) \quad V = \pm \frac{2}{D_1^2} \sqrt{-D_1(D_1 D_2 B - 2D_1 kT - 4k^2 T^2)} kT, \quad B = B_1, B_2, B_3.$$

It is impossible to solve analytically the $\Delta = 0$ associated with this phase with respect to temperature due to the higher order polynomials. Instead we can approximate the temperature when the phase $V = 0, B = 0$ transitions to $V \neq 0, B \neq 0$. The non-zero solution to (3.30) will exist when the square root term is real,

$$D_1 D_2 B - 2D_1 kT - 4k^2 T^2 \geq 0.$$

Assuming that B and V are small near the phase transition, then

$$\text{as } B \rightarrow 0 \implies T \leq -\frac{D_1}{2k}.$$

Therefore the phase $V = 0, B = 0$ transitions to $V \neq 0, B \neq 0$ when $T \leq -\frac{D_1}{2k}$.

3.4 Phase diagrams with order parameters

In the previous subsection we calculated analytic approximations to the order parameters B and V as functions of temperature under the assumption that B and V are small. We could also numerically calculate B and V as functions of temperature using two different methods.

The first method would be to calculate numerically the minimum points in the free energy for a range of temperatures, see Figure 3.3. Calculating the free energy as

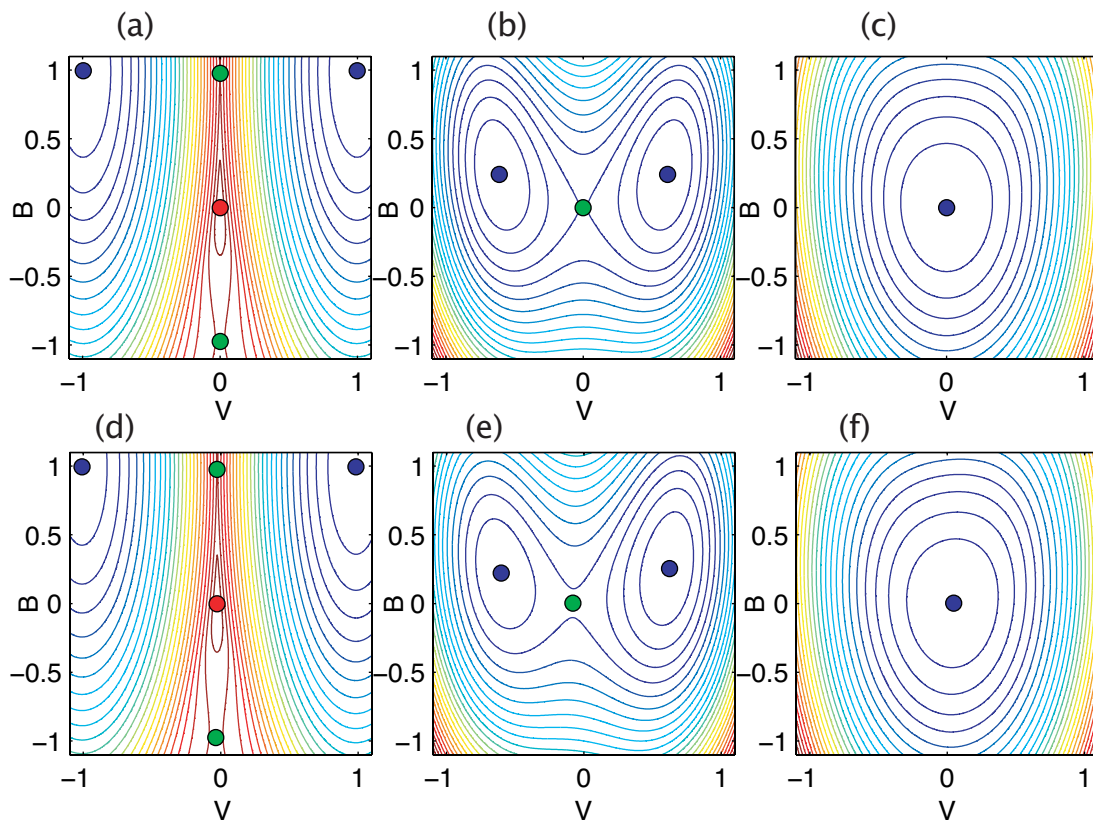


Figure 3.3: Cone angle $\theta_0 = \frac{\pi}{4}$; temperature (a) 0.01, (b) 0.8, (c) 1.2 with an applied electric field in y direction $E_y = 0$; temperature (d) 0.01, (e) 0.6, (f) 0.95 with an applied electric field in y direction $E_y = 0.05$. All stationary points of free energy surface are found and plotted on the contour plot: minima are blue, saddle points are green, maxima are red.

a function of B and V , we are left with a surface. It is non-trivial to detect the spatial critical points on an arbitrary discrete grid, and our first attempt at finding the stationary points was to move over a fixed grid finding where both $\frac{dF}{dV} = 0$ and $\frac{dF}{dB} = 0$ and then calculate the discriminant Δ (3.33) to classify and organise the stationary points. However, the discrete nature of the problem meant that the number of points identified as stationary was dependent on the size of the discretisation used. We therefore made use of the Matlab `contour` function which plots isolines at various levels of a surface, making it ideal to find the zero isoline of the surfaces $\frac{dF}{dV}$ and $\frac{dF}{dB}$. Next we calculated where the two isolines crossed using the Matlab function `intersections`, giving the coordinates (B, V) of the stationary points of the free energy. In this way we could calculate the stationary points for a range of temperature. However, this method is time consuming and computer intensive, leading us to another alternative method.

The second method would be to solve the simultaneous equations given by the definitions of B and V ,

$$B = \sum_{\tau_2=-1,1} \int_{-\pi}^{\pi} \cos 2(\phi_2 - \bar{\phi}) f(\phi_2, \tau_2) d\phi_2, \quad (3.35)$$

$$V = \sum_{\tau_2=-1,1} \int_{-\pi}^{\pi} \tau_2 \cos(\phi_2 - \bar{\phi}) f(\phi_2, \tau_2) d\phi_2, \quad (3.36)$$

and the equation for f in (3.4). All integrations were performed using the composite Simpson's rule and the system of equations was solved using the Matlab function `fsolve` for a range of temperature values. The previous method of calculating the minima of the free energy surfaces does, however, provide useful initial guesses of B and V for `fsolve` at low temperatures. The calculated B and V were then used for the initial guess of the following temperature. In Figure 3.4 we plot

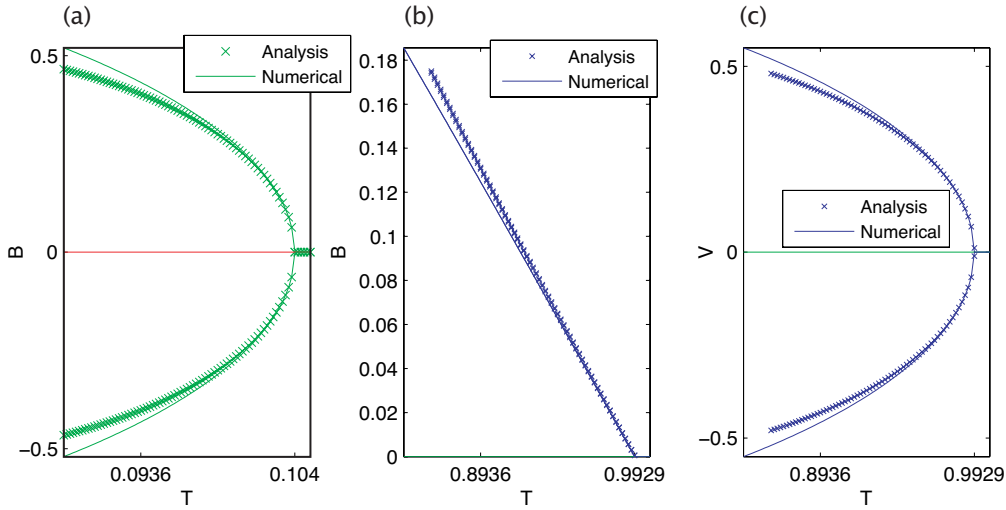


Figure 3.4: Cone angle $\theta_0 = \frac{\pi}{4}$, applied electric field in y direction $E_y = 0$. Red denotes a maximum, green a saddle point, and blue a minimum. Analytic and numerical approximations to the phase diagrams: (a) Phase ($B \neq 0, V = 0$) is a saddle point when $T < -\frac{D_2}{2k} = 0.104$, (b), (c) Phase transition ($B = 0, V = 0$) to ($B \neq 0, V \neq 0$) when $T < -\frac{D_1}{2k} = 0.9929$. Analysis matches numerical approximation well when B and V are small.

the analytic and numerical approximations for B and V against temperature. We used the b_i coefficients that were calculated from the base set of molecular parameters from the previous Chapter. We can see that the temperatures at which the phase transitions occur are the same for both approximations, and as we expected, the analytic approximation is less accurate as B and V increase in size.

The full numerical solutions for (3.35), (3.36) have been plotted in Figures 3.5 and 3.6, with cone angles of $\theta_0 = \frac{\pi}{4}, \frac{\pi}{3}$ respectively. Not all of the multiple solutions are minima. A few examples of the energy surface and the numerically determined stationary point solutions for B and V are shown in Figures 3.3, and 3.7. The free energy surface was calculated at temperatures to display the various possible solutions of B and V .

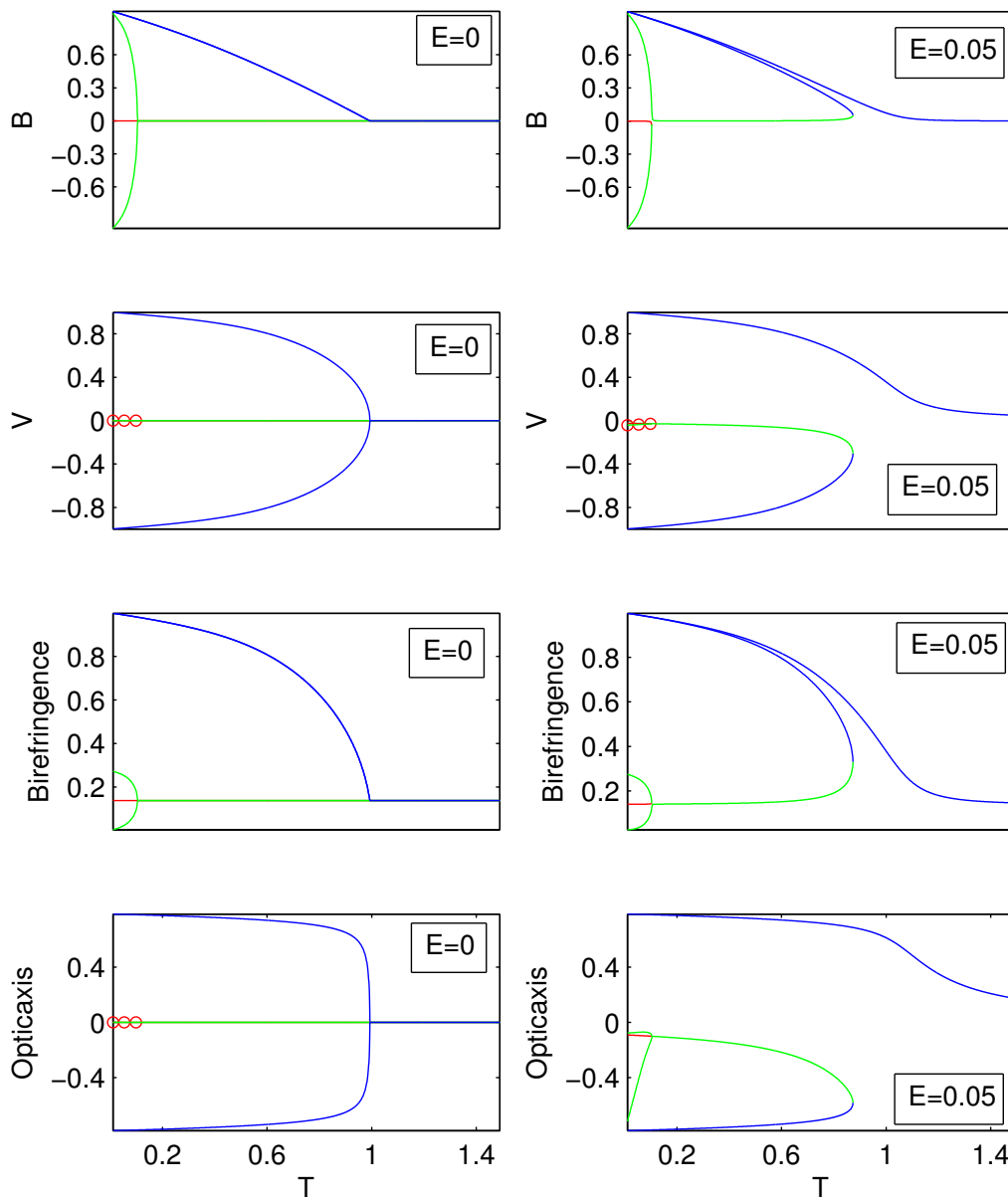


Figure 3.5: Cone angle $\theta_0 = \frac{\pi}{4}$. Order parameters B , V , birefringence and optic axis are plotted against temperature. Blue solutions are minima, green solutions are saddles, red solutions are maxima, and red circles show multiple solutions.

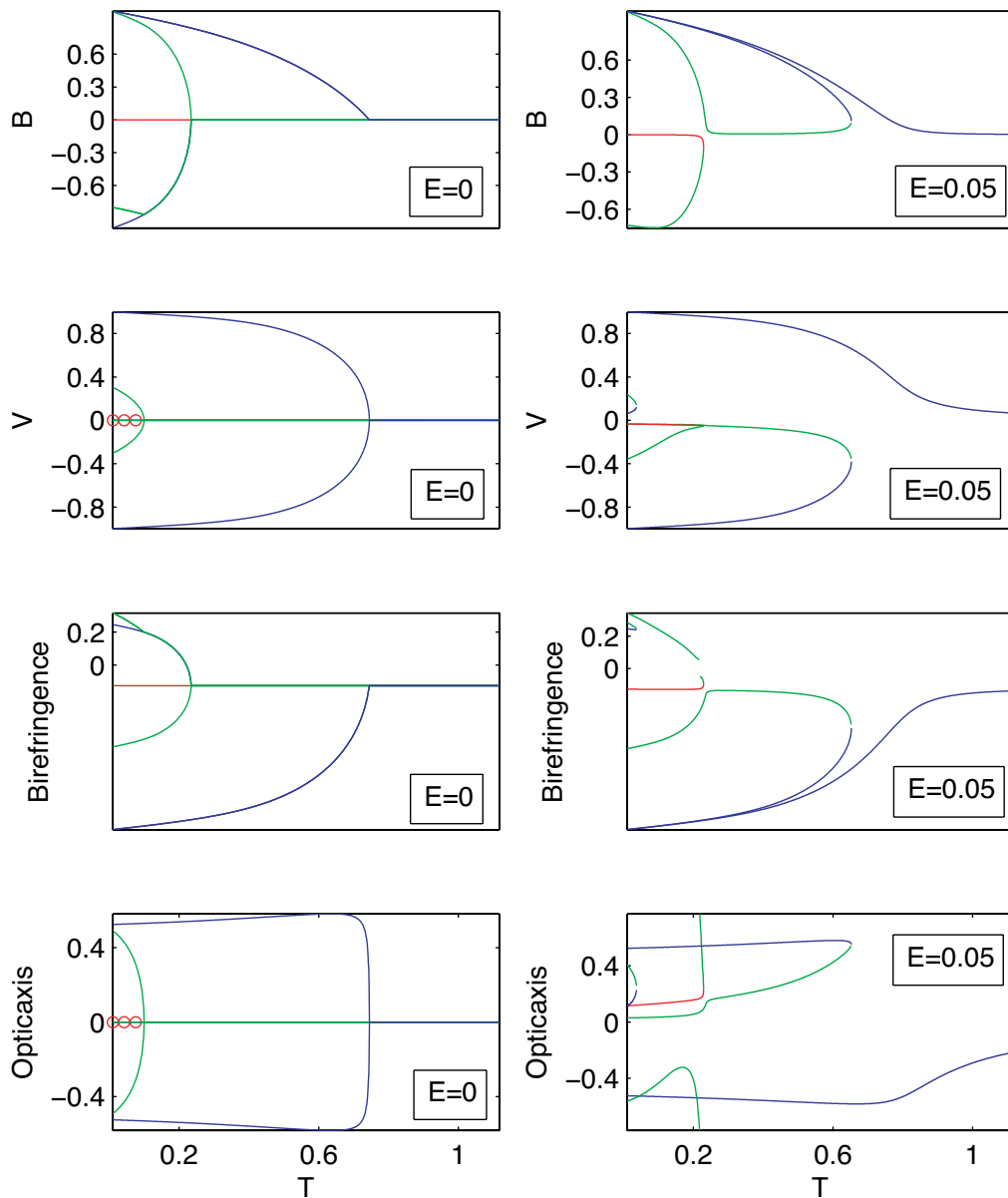


Figure 3.6: Cone angle $\theta_0 = \frac{\pi}{3}$. Order parameters B , V , birefringence and optic axis are plotted against temperature. Blue solutions are minima, green solutions are saddles, red solutions are maxima, and red circles show multiple solutions.

When $(E = 0, \theta_0 = \frac{\pi}{4})$, the stable phases that are possible are Sm A* ($V = 0, B = 0$) and Sm C* ($V \neq 0, B \neq 0$). When $(E_y = 0.05, \theta_0 = \frac{\pi}{4})$, the electroclinic effect causes ordering to appear in the tilt of the previous Sm A* phase ($V > 0, B > 0$). As temperature decreases bifurcation occurs and there is another stable solution ($V < 0, B > 0$). The energy levels of the stable solutions are not equal, ($V > 0, B > 0$) is the lowest energy state by design of the electric field interaction term in (3.19).

The solutions for (3.35, 3.36) when $\theta_0 = \frac{\pi}{3}$ are similar to $\theta_0 = \frac{\pi}{4}$. However, another stable phase occurs as temperature decreases below $T \approx 0.1$. The minimum is more apparent in Figure 3.7(a) and (b). When $E = 0$ the minimum of ($V = 0, B \approx -1$) would suggest a Sm A* biaxial phase. When $E_y = 0.05$ the stable phase would be a highly biaxial phase with a low tilt.

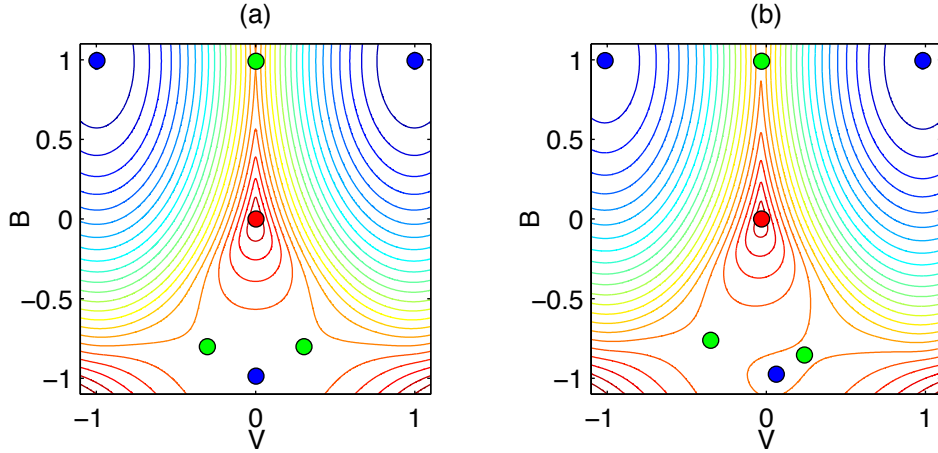


Figure 3.7: Cone angle $\theta_0 = \frac{\pi}{3}$, temperature $T = 0.01$ with an applied electric field (a) $E_y = 0$ and (b) $E_y = 0.05$. All stationary points of free energy surface are found and plotted on the contour plot: minima are blue, saddle points are green, maxima are red.

3.4.1 Optic axis and Birefringence

The optic axis and birefringence of a material are of importance when it comes to device applications. The optic axis is the tilt angle of the director and the birefringence is the ratio of the difference in refractive index and the difference of the average refractive index. Clark et al. [45] presented expressions to calculate the optic axis and the birefringence given the cone angle and distribution of the azimuthal angle,

$$\frac{\tan 2\Theta}{\tan 2\theta_0} = \left[\frac{\tan^2 \theta_0 - 1}{\frac{1}{2}(B + 1) \tan^2 \theta_0 - 1} \right] V, \quad (3.37)$$

$$\frac{\Delta n}{\Delta n_0} = \left[\frac{\frac{1}{2}(B + 1) \tan^2 \theta_0 - 1}{\tan^2 \theta_0 - 1} \right] \frac{\cos 2\theta_0}{\cos 2\Theta}. \quad (3.38)$$

The full numerical solutions for (3.35, 3.36) were used to calculate the optic axis and birefringence and have been plotted in Figures 3.5 and 3.6, with cone angles of $\theta_0 = \frac{\pi}{4}, \frac{\pi}{3}$ respectively.

3.5 Investigation of molecular model parameters

The mean-field theory and the Maier-Saupe interaction potential have enabled the calculation of a free energy for our model 3.6. Given a set of parameters for the molecular pair interaction potential, we can therefore calculate order parameters for the system. These order parameters, B and V , are measures of the distribution of molecules about a cone for a fixed temperature and fixed cone angle. The optic axis and birefringence of our model are expressed in terms of B and V .

In the previous Chapter we investigated two intermolecular pair potentials, the

Gay-Berne potential and the dipole-dipole potential. These two potentials have molecular parameters for steric properties and dipole strength and location. However, the free energy would be too complicated to calculate analytically for these potentials so we performed a Fourier analysis. Assuming the form of the pair potential was that of the Maier-Saupe potential (3.10), we can then couple the molecular parameters to the coefficients of the terms of the Maier-Saupe potential. In Figure 3.8 we plotted the b_i coefficients (3.11) whilst varying the four molecular parameters: κ molecular length-breadth ratio, κ' the side-side to end-end well-depth ratio, ν the dipole location, and d_{\perp} the dipole strength.

The order parameters B and V were calculated whilst varying the four molecular

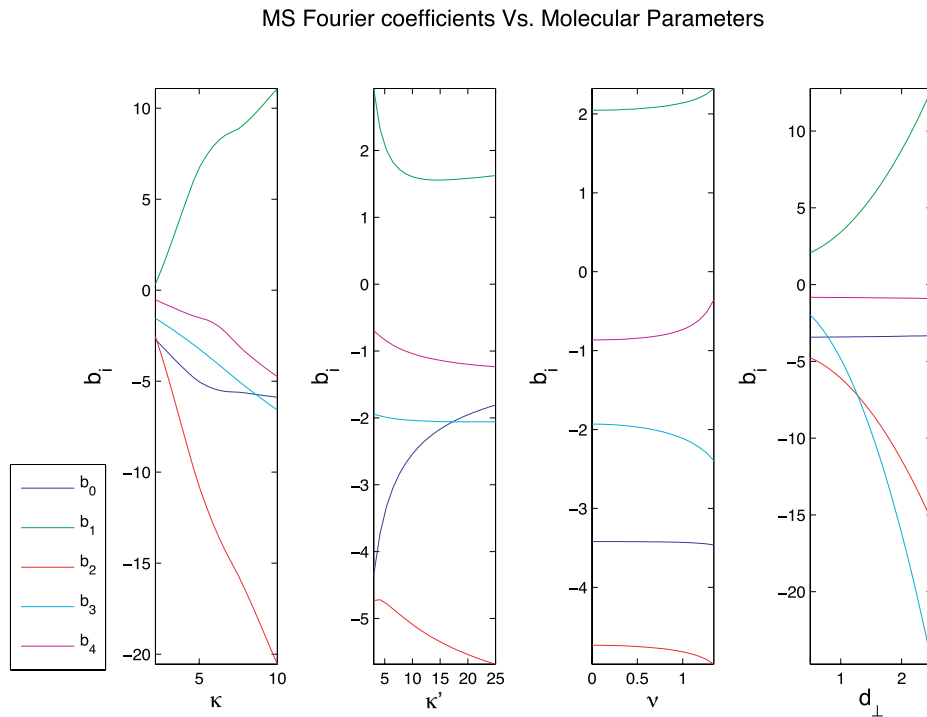


Figure 3.8: The Maier-Saupe Fourier coefficients (3.11) are plotted against the molecular parameters: κ , the molecular length-breadth ratio, κ' , the side-side to end-end well-depth ratio, ν , dipole location, and d_{\perp} , dipole strength.

potentials in turn. However, it would be trivial to calculate the related optic axis and birefringence plots. Figures 3.9 and 3.10 show the order parameters versus temperature in the absence and presence of an electric field. The predominant feature when changing any of the molecular parameters is the change in the critical temperature when $E = 0$. When an electric field is applied we see an increase in B and V when we increase any of the four parameters. Varying κ , Fig. 3.9, and d_{\perp} , Fig. 3.10, had the biggest effect on the transition temperatures, B and V of the four parameters with the values measured. Increasing κ increases the length-breadth ratio of the molecules. Longer, slimmer molecules can pack more efficiently than squatter molecules so we would expect the smectic order to increase as κ increases. We would expect molecules with increasing dipole strength, d_{\perp} , to align more tightly than molecules with weak dipoles. The influence of the side-side to end-end well-depth ratio, κ' , and the dipole location, ν , may be confounded by the assumptions of a fixed molecular tilt angle and the molecular distribution, $f(\phi, \theta)$, not depending on the short axis of the molecule respectively.

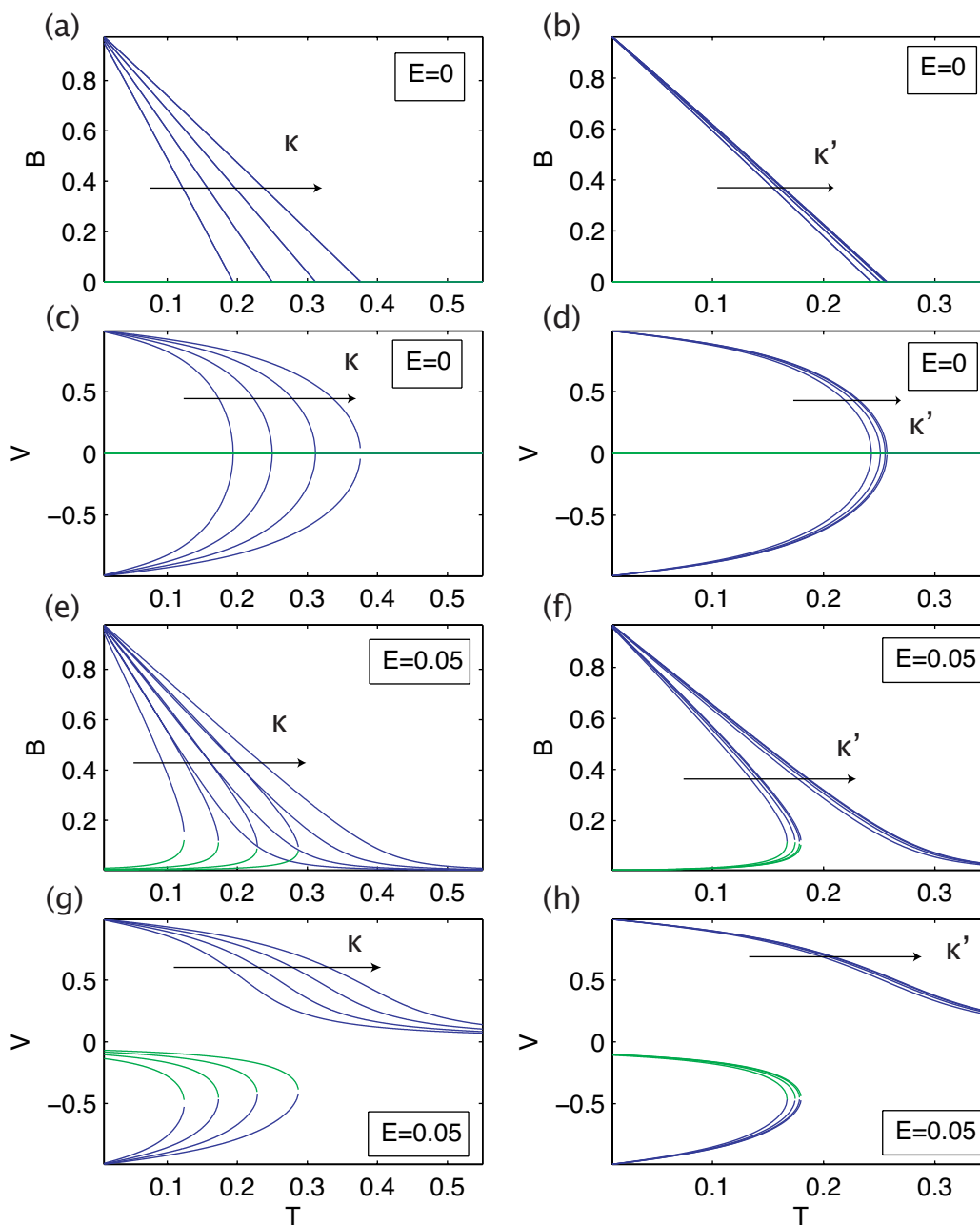


Figure 3.9: Cone angle $\theta_0 = \frac{\pi}{12}$, minima are blue, saddle points are green. We vary the molecular parameters: (a)(c)(e)(g) $\kappa = [2.20, 3.02, 3.84, 4.66]$, increasing the length-breadth ratio of the molecules increases the temperature for transition; (b)(d)(f)(h) $\kappa' = [3, 6.47, 11.11, 15.74]$, the GB well-depth ratio has little effect on the phase diagrams.

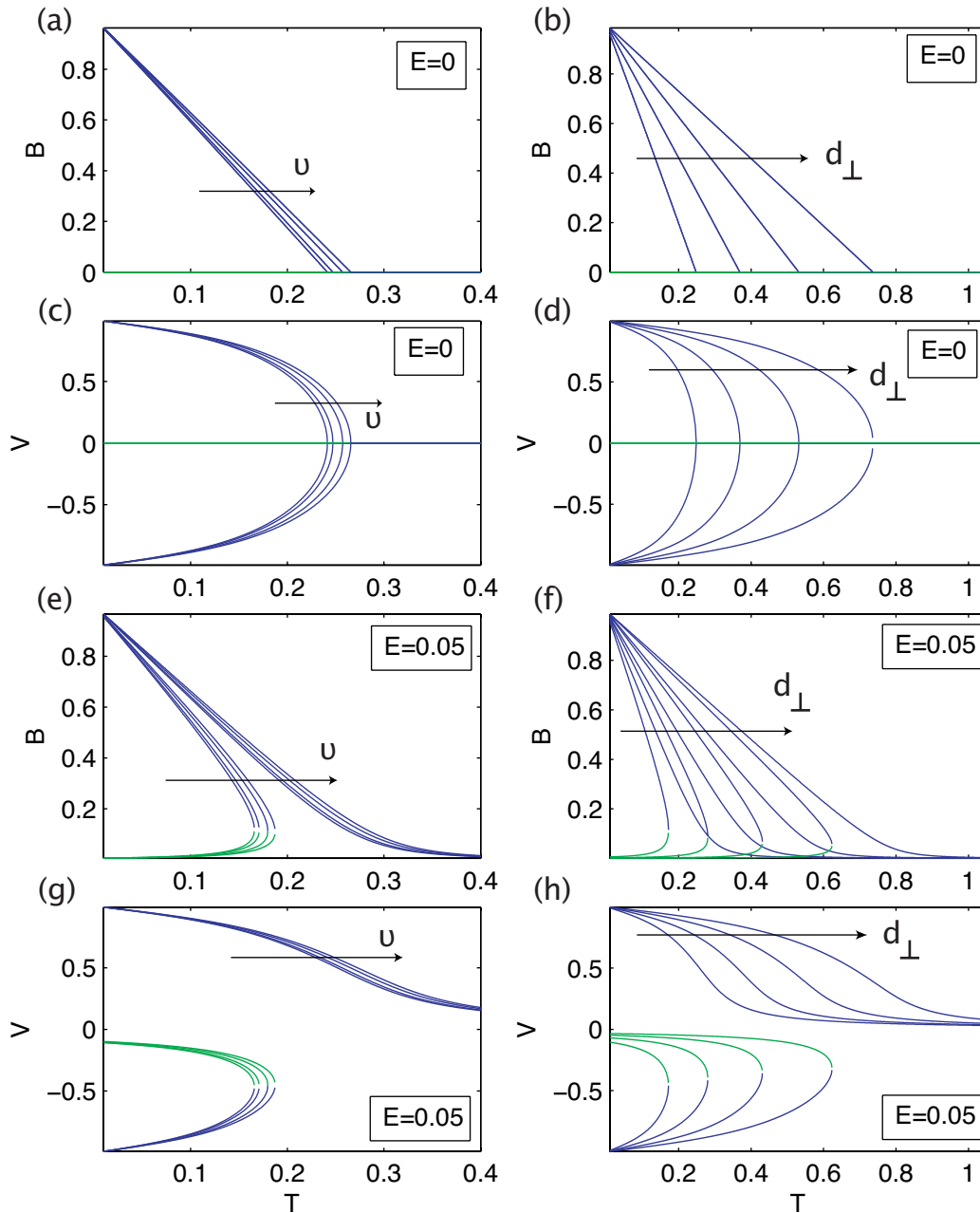


Figure 3.10: Cone angle $\theta_0 = \frac{\pi}{12}$, minima are blue, saddle points are green. We vary the molecular parameters: (a)(c)(e)(g) $\nu = [0, 0.55, 0.87, 1.03]$, dipole location appears to have little effect on the phase diagrams; (b)(d)(f)(h) $d_{\perp} = [0.5, 0.71, 0.92, 1.13]$, dipole strength has a large effect in scaling the transition temperature.

3.6 Summary

In this Chapter we have calculated the free energy given the Maier-Saupe pair potential using the mean-field theory. We have minimised the free energy with respect to the order parameters V and B , representing tilt and biaxiality respectively. The optical axis and birefringence were calculated in terms of the order parameters. The temperature dependence of the order parameters, optical axis and birefringence can be displayed using phase diagrams. This means that we have the capabilities to vary the parameters of the intermolecular potential and see the effect on the optical properties of the bulk of the material. Using the base parameter sets from Chapter 2, the Maier-Saupe potential parameters were varied, which in turn varied the phase diagrams of the order parameters against temperature.

So far we have successfully modelled liquid crystals at the molecular level and the mesoscopic level, even managing to link the two length-scales. We can alter the molecular properties of our molecules and see what effect they have on the physical observables, the optic axis and birefringence, of the bulk material. In Chapter 4 we will describe a simple model, that will allow us to investigate device applications, which we will then link to the Maier-Saupe free energy we derived in this Chapter.

4 Phenomenological model for switching in de Vries FLCs

4.1 Landau-de Gennes Theory

In previous Chapters we have looked at building models of liquid crystals from the interactions of the individual molecules with varying degrees of complexity. We now look at modelling on a different length-scale. The Landau - de Gennes [46] theory is a phenomenological model which tries to capture important qualities of the phase transition. Rather than building from molecular interactions to describe the behaviour of the system, the theory tries to reduce the complexity of the model and focus on the mesophase transitions.

The phase transitions we are interested in are driven by a change in temperature, we call this a thermotropic transition. This means that at a higher temperature there is a less-ordered phase than at a lower temperature. A phase transition can be identified through the use of an order parameter which often describes a change in the symmetry properties from one phase to the next.

The structural order of the mesophases will often be distinguishable from each other by the symmetry present in each mesophase. When operations, such as translations, rotations and reflections, are applied to the structure of the phase and the structure is left unchanged, then the symmetry of the phase is said to have those characteristics. The less ordered high temperature phase will have greater symmetry than the more ordered low temperature phase. Symmetry is broken at the phase transition. For example, when we compare the nematic phase to the Sm

A phase we notice that the degree of translational symmetry differs between the phases. In the nematic phase translation in any direction by any amount will have no effect on the nematic phase. However, due to the layers, the Sm A phase will only allow translation in the direction of the layer normal by a distance which is a multiple of the layer spacing. There are occasions where a change in symmetry is not present in the phase transition, the liquid-gas transition for instance. However, an order parameter depending on liquid density can be used.

The primary property of an order parameter is that it will have a value of zero in the high temperature phase and will be non-zero in the lower temperature phase. The phases' transitions can be first-order discontinuous or second-order continuous depending on the transition mechanism. The nematic-isotropic phase transition is first order in the widely used S order parameter, and the Sm A-nematic phase transition is second-order in the order parameter describing the formation of the layers. The Landau-de Gennes theory uses an order parameter to describe the phase transition.

4.2 Free Energy

4.2.1 The thermotropic terms

We are interested in modelling the Sm A (Sm A) to Sm C (Sm C) phase transition using a Landau-de Gennes type theory. The material is assumed to be a de Vries liquid crystal so we are primarily interested in the distribution of the molecules around a cone with fixed tilt angle θ . The distribution of molecules' azimuthal angle is assumed to be a uniform probability function of domain $(-d\phi, d\phi)$, see

Figure 4.1. We use this simplification because, in reality, the probability density function will not be uniform but analysis is impossible for a more complicated case. In the Sm A phase $d\phi = \pi$ and in the Sm C phase $0 \leq d\phi < \pi$. Hence, the order parameter we will use is $\Psi = (\pi - d\phi)$.

The Landau-de Gennes theory [46] assumes that close to transition in Sm C the order parameter will be small, so the free energy can be expanded as a power series in the order parameter. The Gibbs free energy of a system at constant temperature and volume is

$$G(\Psi, T) = a_0(T - T_a)\Psi^2 + a\Psi^3 + b\Psi^4, \quad (4.1)$$

with positive constants a_0 and b and negative constant a . The coefficient of the leading term of the power series expansion has the form of the simplest temperature dependence possible, when $a = 0$, T_a is the transition temperature.

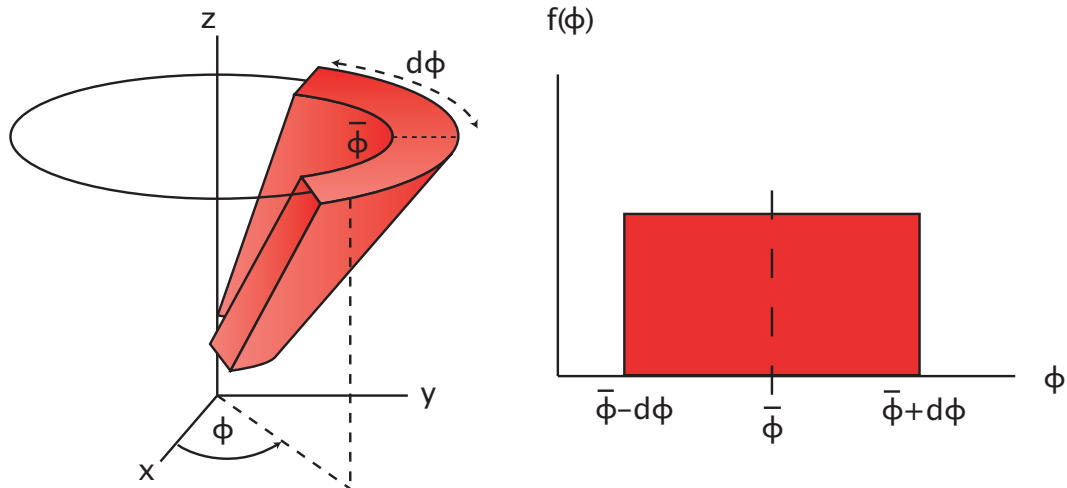


Figure 4.1: Molecular distribution described by the director azimuthal angle $\bar{\phi}$ and the spreads $d\phi$ around the Sm cone, and the probability distribution function, $f(\theta)$.

4.2.2 Analysis of the thermodynamic terms

Our expression for the Gibbs free energy (4.1) is dependent on our order parameter Ψ and temperature T , by performing relatively simple analysis we can ascertain which properties the Landau expansion models. Whichever temperature we choose, the system will prefer a stable energy state. Therefore, we calculate the stationary points of the free energy with respect to the order parameter and assess their qualities. The temperature dependence of the order parameter can be calculated by solving $\frac{dG}{d\Psi} = 0$ for Ψ ,

$$\frac{dG}{d\Psi} = 2a_0(T - T_a)\Psi + 3a\Psi^2 + 4b\Psi^3 = 0, \quad (4.2)$$

$$\text{so } \Psi_0 = 0, \text{ or } \Psi_{\pm} = \frac{-3a \pm \sqrt{9a^2 - 32a_0(T - T_a)b}}{8b}, \quad (4.3)$$

Ψ_+ denotes the solution where the square root term is added, and Ψ_- denotes the solution where the square root term is subtracted. The solution $\Psi = 0$ represents the lower ordered Sm A phase and the $|\Psi| > 0$ solutions represent the higher ordered Sm C phase.

The discriminant of the polynomial on the right hand side of equation (4.2) will determine when the roots are real or complex. The cubic discriminant has the form

$$D_3 = \alpha_1^2\alpha_2^2 - 4\alpha_0\alpha_2^3 - 4\alpha_1^3\alpha_3 + 18\alpha_0\alpha_1\alpha_2\alpha_3 - 27\alpha_0^2\alpha_3^2,$$

where $[\alpha_0, \alpha_1, \alpha_2, \alpha_3]$ are the coefficients of $[\Psi^0, \Psi^1, \Psi^2, \Psi^3]$ in (4.2) respectively. When $D_3 < 0$ there is one real root and two complex conjugate roots, $D_3 = 0$

means there are three real roots with two being equal, and when $D_3 > 0$ there are 3 real distinct roots. Here the discriminant has the form,

$$D_3 = 36(a_0(T - T_a))^2 a^2 - 128(a_0(T - T_a))^3 b. \quad (4.4)$$

The discriminant is zero when

$$T_1 = T_a, \quad \text{or} \quad T_2 = T_a + \frac{9a^2}{32a_0b}, \quad (4.5)$$

and we see from (4.2) that when $T > T_2$ there will be one real and two complex roots; when $T = T_2$ or $T = T_1$ there will be three real roots where two are equal; and when $T_1 < T < T_2$ or $T < T_1$ there will be three distinct roots. The stability of the roots as it relates to energy can be found from looking at the second derivative of the energy with respect to Ψ . Using the second derivative test we know that the solution Ψ_0 is a minimum when $T > T_1$. The solution Ψ_+ is a minimum when $T < T_2$, and the solution Ψ_- is a minimum when $T < T_1$. The roots and their stabilities are displayed on Figure 4.2.

At any given temperature the system prefers whichever Ψ solution has lowest free energy. Given that we have chosen $a_0 > 0$, $b > 0$ and $a < 0$ for the model coefficients, we can calculate which Ψ solution gives lowest free energy. We find $G(\Psi_0) < G(\Psi_{\pm})$ when $T > T_a + \frac{a^2}{4a_0b}$, and $G(\Psi_+) < G(\Psi_{0,-})$ when $T < T_a + \frac{a^2}{4a_0b}$. However, the system may not always lie in the lowest energy state. If we were to reduce temperature and investigate when the high temperature Ψ_0 phase transitions to the low temperature Ψ_+ phase, the transition temperature would be $T = T_a$ rather than $T = T_a + \frac{a^2}{4a_0b}$. This is due to the energy barrier between the two stable energy states stemming from the discontinuity at T_2 . We

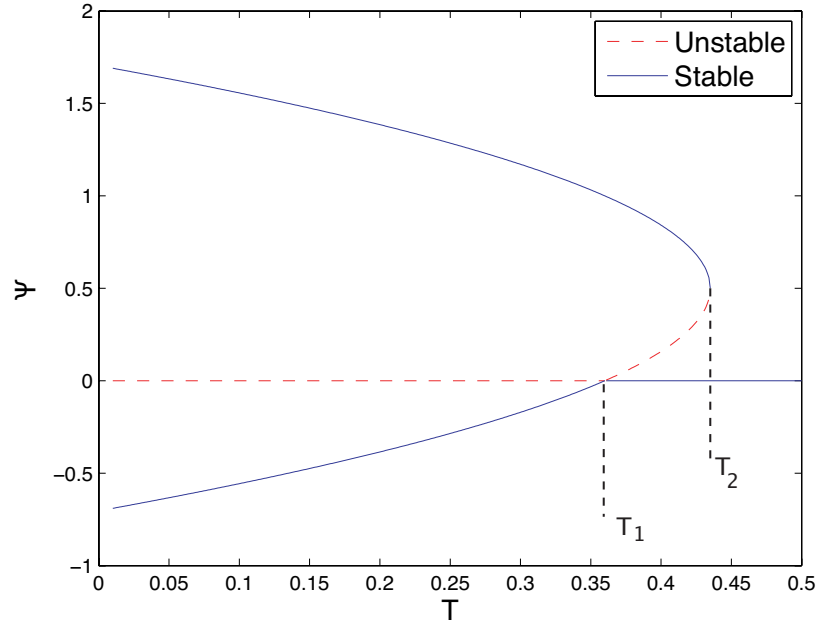


Figure 4.2: $\Psi = \pi - d\phi$ versus temperature T . The stability of the branches is denoted by solid or dashed lines. T_1 and T_2 are the transition temperatures

can calculate the discontinuity of the order parameter at T_2 by substituting this transition temperature into (4.3),

$$\Psi = 0, \quad \text{or} \quad \Psi = -\frac{3a}{8b}.$$

Clearly $a < 0$ is necessary if Ψ is to be positive and the discontinuity will exist while $a \neq 0$.

The thermodynamic terms of the free energy were designed in this way for two reasons. Firstly, at high temperatures there is one minimum Ψ of the function and when the temperature decreases past some transition temperature there will be two minima. Secondly, the Ψ_+ minimum has a lower energy than the other minimum. These two characteristics are modelled using the quadratic, cubic and

quartic terms of a Landau expansion where the coefficient of the cubic term is negative to meet the second characteristic.

4.2.3 The dielectric terms

So far we have assumed that the cone tilt angle θ is fixed and allowed the distribution of molecules about the director to change depending on temperature. By adding dielectric terms to the free energy of the system, we can incorporate electric field effects and polarisation self-interaction, and investigate the effect these terms have on the distribution and orientation of the molecules in the steady state.

To construct these dielectric terms we look at the polarisation present in a layer of our material. The Sm layer lies in the xy -plane and on each molecule there exists a dipole perpendicular to the long axis of the molecule in this plane. The strength of

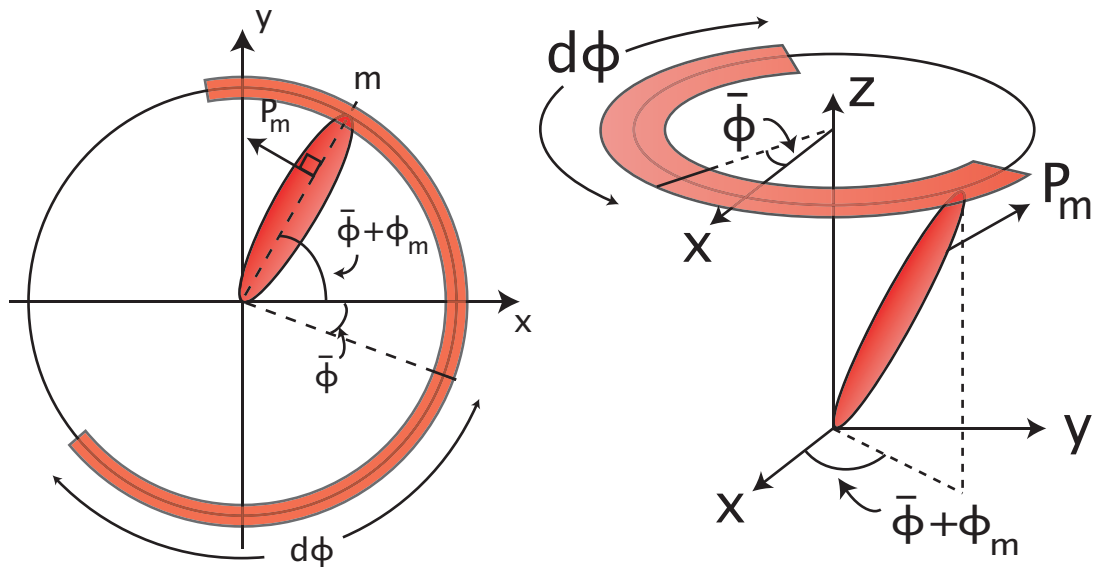


Figure 4.3: Dipole of molecule m , P_m , described by the director azimuthal angle $\bar{\phi}$ and the spreads $d\phi$ around the Sm cone

the dipole is the local molecular polarisation P and the polarisation vector for each molecule is $\mathbf{P}_m = P(\cos \psi_m, \sin \psi_m, 0)$. The angle between the dipole of molecule m and the x -axis is $\psi_m = \bar{\phi} + \phi_m + \frac{\pi}{2}$, and ϕ_m is the difference in azimuthal angle of molecule m from the director azimuth angle $\bar{\phi}$, see Figure 4.3. The distribution of molecules around the Sm cone is assumed to be uniform from $[\bar{\phi} - d\phi, \bar{\phi} + d\phi]$ about the azimuthal angle of the layer director $\bar{\phi}$. Therefore, the net polarisation of the layer is simply the sum of these local molecular polarisations. We then integrate \mathbf{P}_m with respect to the distribution of molecules, f , on the smectic cone to calculate the net polarisation

$$\begin{aligned} \mathbf{P} &= \int_{-d\phi}^{d\phi} \mathbf{P}_m f(\phi_m) d\phi_m = \int_{-d\phi}^{d\phi} P(\cos \psi_m, \sin \psi_m, 0) f(\phi_m) d\phi_m \\ &= \int_{-d\phi}^{d\phi} P \left(\cos(\bar{\phi} + \phi_m + \frac{\pi}{2}), \sin(\bar{\phi} + \phi_m + \frac{\pi}{2}), 0 \right) f(\phi_m) d\phi_m \\ &= P \int_{-d\phi}^{d\phi} (-\sin(\bar{\phi} + \phi_m), \cos(\bar{\phi} + \phi_m), 0) f(\phi_m) d\phi_m. \end{aligned}$$

Expressing the polarisation vector as a combination of the unit vectors \mathbf{i} and \mathbf{j} in the \mathbf{x} and \mathbf{y} directions we have

$$\begin{aligned} \mathbf{P} &= -\mathbf{i}P \int_{-d\phi}^{d\phi} (\sin \bar{\phi} \cos \phi_m + \cos \bar{\phi} \sin \phi_m) \frac{1}{2d\phi} d\phi_m \\ &\quad + \mathbf{j}P \int_{-d\phi}^{d\phi} (\cos \bar{\phi} \cos \phi_m - \sin \bar{\phi} \sin \phi_m) \frac{1}{2d\phi} d\phi_m \\ &= -\mathbf{i}P \left[\sin \bar{\phi} \frac{\sin \phi_m}{2d\phi} + \cos \bar{\phi} \frac{\cos \phi_m}{2d\phi} \right]_{-d\phi}^{d\phi} + \mathbf{j}P \left[\cos \bar{\phi} \frac{\sin \phi_m}{2d\phi} + \sin \bar{\phi} \frac{\cos \phi_m}{2d\phi} \right]_{-d\phi}^{d\phi} \\ &= P \left(-\sin \bar{\phi} \frac{\sin d\phi}{d\phi}, \cos \bar{\phi} \frac{\sin d\phi}{d\phi}, 0 \right). \end{aligned}$$

We have now calculated the net polarisation of the layer so we can add dielectric terms to our Gibbs free energy. The self-interaction energy of a polarisation \mathbf{P}

within a material was presented by Goodby *et al* [47]. In a material of dielectric susceptibility χ , the self-interaction energy is given as $\frac{\mathbf{P}^2}{2\chi}$. The self-interaction energy term of the free energy is

$$G_{inter} = \frac{\mathbf{P}^2}{2\chi} = \frac{P^2 \sin^2 d\phi}{2\chi d\phi^2}. \quad (4.6)$$

The spontaneous polarisation interacting with an external field $\mathbf{E} = E(\cos \psi, \sin \psi, 0)$, where ψ is the angle of E field in relation to the x axis, will have an energy of $-\frac{\mathbf{E} \cdot \mathbf{P}}{2}$. The final dielectric term of the free energy is

$$G_{elec} = -\frac{\mathbf{E} \cdot \mathbf{P}}{2} = -\frac{EP}{2} \sin(\psi - \bar{\phi}) \frac{\sin d\phi}{d\phi}. \quad (4.7)$$

4.2.4 The thermotropic and dielectric free energy

The free energy of the system including the thermotropic and dielectric terms is thus

$$G = G_{therm} + G_{inter} + G_{elec} \quad (4.8)$$

$$= a_0(T - T_a)\Psi^2 + a\Psi^3 + b\Psi^4 + \frac{P^2 \sin^2 d\phi}{2\chi d\phi^2} - \frac{EP \sin d\phi}{2 d\phi} \sin(\psi - \bar{\phi}), \quad (4.9)$$

where a is a negative constant, a_0 and b are positive constants, P is the local molecular polarisation, χ is susceptibility, E is an applied electric field with angle ψ from the x axis, and T_a is a constant temperature near the transition from Sm C to Sm A phase if $P = 0$.

The first three terms in (4.9) are derived from the Taylor expansion of the ther-

modynamic potential function. The thermodynamic terms will exhibit one stable root of $d\phi = \pi$ when the temperature $T > T_2$, and two stable roots when $T < T_2$. When $T < T_1$ the root $d\phi < \pi$ is energetically preferred. The negative constant a causes the stable root $d\phi < \pi$ to have minimum energy. The fourth term of the energy is the self-energy of a polarisation P within a material of susceptibility χ . This term has a minimum energy contribution when $d\phi = \pi$, it prefers the molecules to be spread apart. The fifth term is the electric-polarisation interaction term and it prefers the molecules to be ordered $d\phi = 0$ and $\bar{\phi} = \psi - \frac{\pi}{2}$.

These three components of the free energy are plotted separately in Figure 4.4. The polar term has a maximum at $d\phi = 0$, the function is symmetric at this line also and it has a minimum at $d\phi = \pi$. When combined with the thermodynamic term, the polar term will influence the free energy to choose equilibrium $d\phi \geq \pi$. The electric field term will have a minimum at $d\phi = 0$ when a field, $E > 0$, is present with angle $\psi = \bar{\phi} + \frac{\pi}{2}$. This means that the spread of the molecules on the Sm cone will decrease as the molecules dipoles align with the electric field. When the electric field is reversed this term prefers an equilibrium $d\phi \approx 4.5$, the molecules would overlap at the opposite side of the cone from $\bar{\phi}$ which disrupts our model design of $d\phi \in [0, \pi]$. In this case we would redefine $\bar{\phi}$ to the opposite side of the cone, which would flip the electric term of the energy which now has a minimum of $d\phi = 0$.

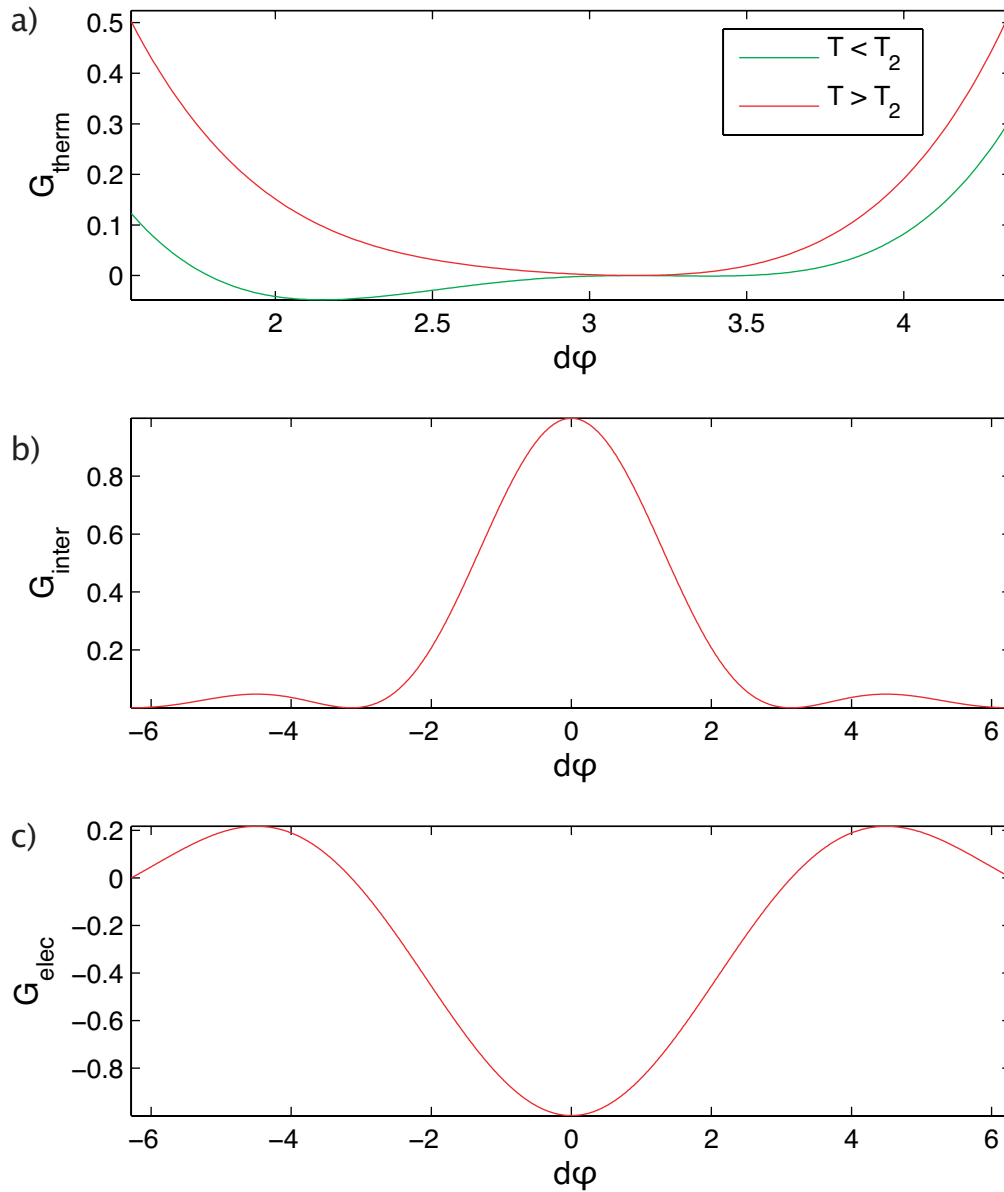


Figure 4.4: Energy versus $d\phi$ for the three components of the free energy (4.8): a) Thermodynamic terms above (red) and below (green) T_2 , b) Polar term, c) Electric term.

4.2.5 Analysis of the energy including the thermodynamic and polar components

We have previously found analytic solutions for Ψ depending on temperature T while only looking at the thermodynamic terms. It is possible to find approximate analytic solutions for $\Psi(T)$ from the thermotropic and self-interaction terms of (4.9). We solve $\frac{\partial G}{\partial \Psi} = 0$ and for ease of working, we redefine $c = \frac{P^2}{2\chi}$. The free energy is now

$$G = a_0(T - T_a)\Psi^2 + a\Psi^3 + b\Psi^4 + c\frac{\sin^2(\Psi)}{(\pi - \Psi)^2}. \quad (4.10)$$

A perturbation analysis, near the Sm C - Sm A transition, will allow the characteristics of the free energy to be revealed. Assuming Ψ is small we calculated the truncated Taylor expansion of our energy about $\Psi = 0$ to $O(\Psi^5)$.

$$G_T = \left(a_0(T - T_a) + \frac{c}{\pi^2}\right)\Psi^2 + \left(a + \frac{2c}{\pi^3}\right)\Psi^3 + \left(b - \frac{c}{3\pi^4}(\pi^2 - 9)\right)\Psi^4. \quad (4.11)$$

Given our model assumptions of a global minimised free energy when $d\phi \in [0, \pi]$, we require that the coefficient of Ψ^3 be negative and Ψ^4 be positive. This gives us:

$$a \leq -\frac{2c}{\pi^3}, \quad c < \frac{3\pi^4 b}{\pi^2 - 9}. \quad (4.12)$$

The first derivative with respect to Ψ will be

$$\frac{dG_T}{d\Psi} = 2\left(a_0(T - T_a) + \frac{c}{\pi^2}\right)\Psi + 3\left(a + \frac{2c}{\pi^3}\right)\Psi^2 + 4\left(b - \frac{c}{3\pi^4}(\pi^2 - 9)\right)\Psi^3, \quad (4.13)$$

which will be zero when $\Psi = 0$ or

$$\Psi = \pm \frac{\sqrt{81\pi^5 a(\pi^3 a + 4c) + 96\pi^4(c^2 - 3bc\pi^2 + a_0(T - T_a)(c(\pi^2 - 9) - 3b\pi^4)) - 540\pi^2 c^2}}{8(3b\pi^4 + 9c - c\pi^2)} - \frac{9\pi^4 a + 18\pi c}{8(3b\pi^4 + 9c - c\pi^2)} \quad (4.14)$$

As previously, the discriminant of the polynomial on the right hand side of equation (4.13) will tell us when the roots are real or complex. The significant temperatures are now

$$T_i = T_a - \frac{c}{a_0\pi^2}, \quad T_{ii} = T_a - \frac{c}{a_0\pi^2} + \frac{27}{32} \frac{(a\pi^3 + 2c)^2}{a_0\pi^2(3b\pi^4 + (9 - \pi^2)c)}. \quad (4.15)$$

The relationship between b and c stated in (4.12) determines that the denominator of the difference $T_{ii} - T_i$ is positive, so $T_i < T_{ii}$. Therefore the temperature at which the model transitions from Sm A to Sm C is T_{ii} . Temperature T_i denotes where the Sm A solution ($d\phi = \pi$) becomes unstable.

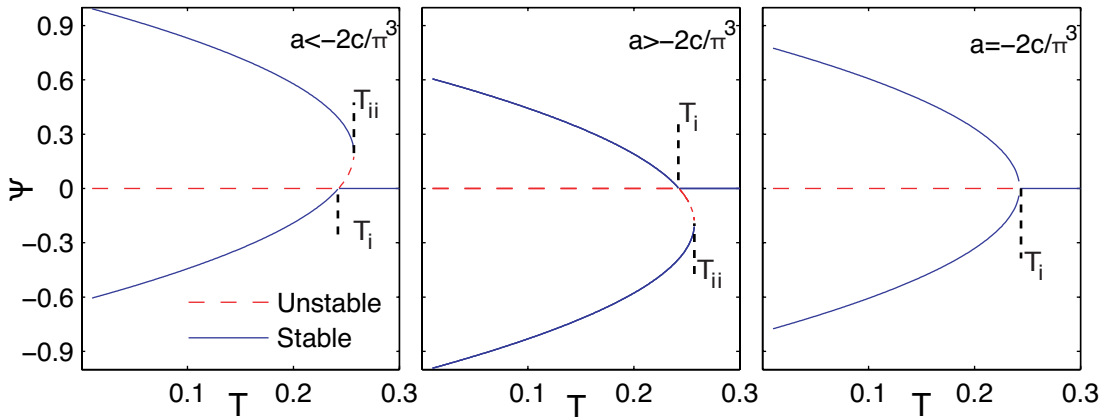


Figure 4.5: $\Psi = \pi - d\phi$ versus temperature T . The stability of the branches of the phase diagram are denoted by solid or dashed lines. T_i and T_{ii} are the transition temperatures. The order of the phase transition depends on parameters a and c .

We repeated the process of calculating the discriminant (4.4) to determine the stable roots of (4.13), see Figure 4.5. There will be one real and two complex conjugate roots when $T > T_{ii}$, three real roots with two being equal when $T = T_i$ or $T = T_{ii}$, and three real and distinct roots when $T < T_i$ or $T_i < T < T_{ii}$. We can see the effect of including the polar term to the free energy on the significant temperatures when we notice that a second order phase transition would be possible, $T_i = T_{ii}$, if $a = -\frac{2c}{\pi^3}$.

The approximate temperature at which the stable roots (4.14) have the same energy is

$$T_{iii} = T_a - \frac{c}{\pi^2} + \frac{3}{4} \frac{(a\pi^3 + 2c)^2}{a_0\pi^2(3b\pi^4 + (9 - \pi^2)c)}, \quad (4.16)$$

below this temperature the Sm C solution, $\Psi > 0$ has a lower free energy.

The next step in our analysis of the free energy we have constructed would be to include the electric field term. Although perturbation analysis can find solutions for $\frac{\partial G}{\partial \Psi} = 0$, the form those solutions take are too unwieldy to be given here. Instead, we will now look at creating a relationship between the Maier-Saupe model from Chapter 3 and the current Landau-de Gennes model.

4.3 Fitting the model parameters

In this Chapter we have created a simple phenomenological model which we hope to relate to the Maier-Saupe model of Chapter 3. In Chapter 3 we investigated a macroscopic level model using order parameters which described the orientational

distribution of the liquid crystal over a range of temperatures and applied electric fields. The order parameters were used to calculate the optic axis and birefringence over the same ranges. The optic axis and birefringence are expressed as

$$\Theta = \frac{1}{2} \tan^{-1} \left[\frac{\tan^2 \theta_0 \langle \cos \psi \rangle (\tan^2 \theta_0 - 1)}{\langle \cos^2 \psi \rangle \tan^2 \theta_0 - 1} \right], \quad (4.17)$$

$$\frac{\Delta n}{\Delta n_0} = \frac{\cos 2\theta_0}{\cos 2\Theta} \left[\frac{\langle \cos^2 \psi \rangle \tan^2 \theta_0 - 1}{\tan^2 \theta_0 - 1} \right], \quad (4.18)$$

respectively, where

$$\langle \cos \psi \rangle = \int_{-d\phi}^{d\phi} \cos(\bar{\phi} + \phi_m) \frac{1}{2d\phi} d\phi_m = \frac{\cos \bar{\phi} \sin d\phi}{d\phi}, \quad (4.19)$$

$$\langle \cos^2 \psi \rangle = \int_{-d\phi}^{d\phi} \cos^2(\bar{\phi} + \phi_m) \frac{1}{2d\phi} d\phi_m = \frac{1}{2} + \frac{\cos 2\bar{\phi} \sin 2d\phi}{4d\phi}. \quad (4.20)$$

It is the matching of one model's optic characteristics to the other that we now undertake.

The mathematical software package Matlab includes an optimisation toolbox that will aid us in the parameter fitting process. The function `lsqcurvefit` will fit unknown model parameters, \mathbf{x} , by minimising the sum of squared differences of two sets of data,

$$\min_{\mathbf{x}} \|F(\mathbf{x}, xdata) - ydata\|_2^2 = \min_{\mathbf{x}} \sum_i (F(\mathbf{x}, xdata_i) - ydata_i)^2. \quad (4.21)$$

The algorithm `lsqcurvefit` uses a trust-region-reflective algorithm described in [48].

In this instance we will be trying to fit the optic axis and the birefringence temper-

ature and electric dependence of the $d\phi$ model, $F(\mathbf{x}, xdata)$, to the Maier-Saupe, $ydata$, results. This means that we will have to solve (4.9) for $d\phi$. As we noted in the last section, a perturbation analysis can calculate the approximate solution (4.13). In the case of $E \neq 0$ the approximate solution is unwieldy so finding the numerical solution may be preferable. In the next section we will describe two possible methods, using a mix of analytic and numerical solutions, for fitting the model parameters $[a_0, T_a, a, b, c, P]$.

4.3.1 Systematic method

In section 4.2.5 we calculated the approximation to Ψ which minimised (4.10). Using Ψ we can calculate the optic axis and birefringence of the model for the case of no electric field, $E = 0$. For this example, the optic axis and birefringence for the Maier-Saupe (MS) model representing the Gay-Berne, GB(3,5,2,1), and dipole-dipole, dd(1.1,0.1), pair potential was calculated.

The function `lsqcurvefit` compares the optic axis and birefringence curves of the $d\phi$ model to those calculated from the MS model and fits the parameters $[a_0, T_a, a, b, c]$. However, fitting five parameters is computationally expensive and time consuming. Instead, we will use some of the information gained from the MS model to reduce the number of parameters we need to fit. Using three different approaches to calculating Ψ and hence the optic axis and birefringence, we fit our parameters systematically.

The first step is to calculate an expression for Ψ at temperatures close to the phase transition when there is no electric field applied. We know the transition

temperature (T_{MS}) and we know that it is a second order transition. It is possible to enforce these qualities on the $d\phi$ model. A second order phase transition for the $d\phi$ model is possible if the coefficient of Ψ^3 in (4.11) is zero

$$a + \frac{2c}{\pi^3} = 0 \Rightarrow a = -\frac{2c}{\pi^3}.$$

Fixing the $d\phi$ transition temperature (4.15) to match T_{MS} , we get an expression for c in terms of (a_0, T_a) ,

$$T_{MS} = T_a - \frac{c}{a_0\pi^2} \Rightarrow c = a_0\pi^2(T_a - T_{MS}). \quad (4.22)$$

Therefore, we can express a in terms of (a_0, T_a)

$$a = -\frac{2a_0}{\pi}(T_a - T_{MS}). \quad (4.23)$$

Using these two expressions of (a, c) we can reduce the problem (4.13) to be solved,

$$\frac{dG_T}{d\Psi} = 2a_0(T - T_{MS})\Psi + 4\left(b - \frac{a_0}{3\pi^2}(\pi^2 - 9)(T_a - T_{MS})\right)\Psi^3. \quad (4.24)$$

Setting $\frac{dG_T}{d\Psi} = 0$, dividing through by a_0 , and substituting

$$B = \frac{4}{a_0}\left(b - \frac{a_0}{3\pi^2}(\pi^2 - 9)(T_a - T_{MS})\right), \quad (4.25)$$

we need to solve

$$0 = 2(T - T_{MS})\Psi + B\Psi^3. \quad (4.26)$$

Solving for Ψ , we get

$$\Psi = 0, \pm \sqrt{\frac{2(T_{MS} - T)}{B}}. \quad (4.27)$$

We have now reduced our function for Ψ to one parameter B for small Ψ . If $\Psi \in [0, \pi]$ then rearranging the second solution (4.27) limits

$$B > \frac{2(T_{MS} - T)}{\pi^2}. \quad (4.28)$$

Expressions for the optic axis and birefringence are calculated using (4.27), (4.17) and (4.18). The function `lsqcurvefit` uses these expressions to fit B given condition (4.28). In Figure 4.6 (a) and (b) the optic axis and birefringence of the MS model, and the fitted $d\phi$ model for small Ψ are plotted. The mean relative error (MRE) was calculated as

$$MRE = \frac{1}{N} \sum_{i=1}^N \frac{|d\phi_i - MS_i|}{MS_i}, \quad (4.29)$$

where the subscript i is the index of the grid, $d\phi_i$ and MS_i are representative of the respective models' optic axis or birefringence discretised surfaces, and N is the number of grid points. At this stage the optic axis is reasonably well fitted with an error of 5%, while the birefringence has error under 1%.

The second stage in fitting the $d\phi$ model is calculating Ψ over a larger temperature range when $E = 0$. For this we need to find the numerical solution of Ψ . We

differentiate the free energy (4.10) with respect to Ψ ,

$$\frac{\partial G}{\partial \Psi} = 2a_0(T - T_a)\Psi + 3a\Psi^2 + 4b\Psi^3 + 2c \left(\frac{\sin \Psi \cos \Psi}{(\pi - \Psi)^2} + \frac{\sin^2 \Psi}{(\pi - \Psi)^3} \right). \quad (4.30)$$

Maintaining the conditions of a second order transition at the same temperature as the MS model (4.22, 4.23), we rewrite the derivative as

$$\begin{aligned} \frac{\partial G}{\partial \Psi} = & 2a_0(T - T_a)\Psi - \frac{6a_0}{\pi}(T_a - T_{MS})a\Psi^2 + 4b\Psi^3 \\ & + 2a_0\pi^2(T_a - T_{MS}) \left(\frac{\sin \Psi \cos \Psi}{(\pi - \Psi)^2} + \frac{\sin^2 \Psi}{(\pi - \Psi)^3} \right). \end{aligned} \quad (4.31)$$

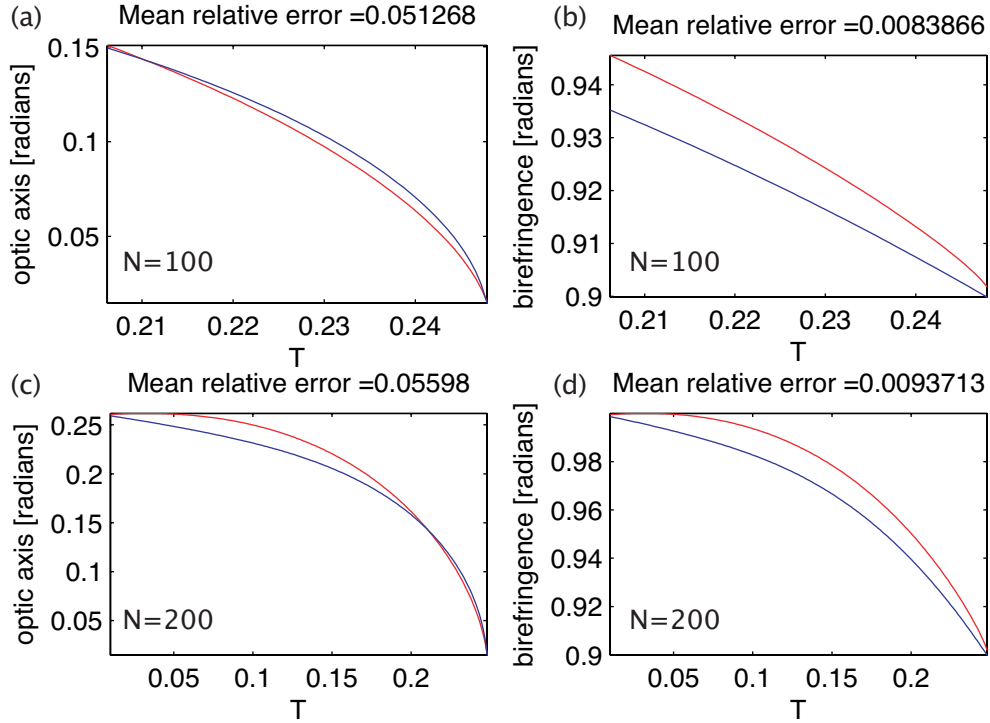


Figure 4.6: A fit of the optical properties of the $d\phi$ model (red) to that of the Maier-Saupe potential (blue) using the conditions determined from the analysis of the Taylor approximation to the $d\phi$ free energy. Initially, for $E = 0$ only the B parameter is fitted (a) and (b), then the T_a parameter (c) and (d).

Lastly, we use the B we fitted by rearranging (4.25) for

$$b = \frac{a_0 B}{4} + \frac{a_0}{3\pi^2}(\pi^2 - 9)(T_a - T_{MS}), \quad (4.32)$$

in (4.31) and note that Ψ is independent of a_0 . The resulting equation

$$\begin{aligned} \frac{\partial G}{\partial \Psi} = & 2(T - T_a)\Psi - \frac{6}{\pi}(T_a - T_{MS})\Psi^2 + 4\left(\frac{B}{4} + \frac{1}{3\pi^2}(\pi^2 - 9)(T_a - T_{MS})\right)\Psi^3 \\ & + 2\pi^2(T_a - T_{MS})\left(\frac{\sin \Psi \cos \Psi}{(\pi - \Psi)^2} + \frac{\sin^2 \Psi}{(\pi - \Psi)^3}\right) = 0, \end{aligned} \quad (4.33)$$

is solved numerically for Ψ , using the Matlab function `fzero`.

Parameter T_a is unknown but is found by fitting to the Maier-Saupe optical surfaces using Matlab function `lsqcurvefit`. Figure 4.6 (c) and (d) shows the optic axis and birefringence of the fitted $d\phi$ model and the MS model. The mean relative errors calculated and the fit after this stage are similar to the first step. The optic axis is within approximately 6% of the MS model, while the birefringence is within 1% of the MS model. It is now fair to say that the $d\phi$ model can be a good approximation to the MS model when no electric field is applied.

The final step in this fitting process is to find a value for parameter P , which models the interaction with the applied electric field. The minimum of the free energy, including the spontaneous polarisation term and the new expressions for

(a, b, c) , is found by solving

$$\begin{aligned} \frac{\partial G}{\partial \Psi} = & 2(T - T_a)\Psi - \frac{6}{\pi}(T_a - T_{MS})\Psi^2 + 4\left(\frac{B}{4} + \frac{(\pi^2 - 9)}{3\pi^2}(T_a - T_{MS})\right)\Psi^3 \\ & + 2\pi^2(T_a - T_{MS})\left(\frac{\sin \Psi \cos \Psi}{(\pi - \Psi)^2} + \frac{\sin^2 \Psi}{(\pi - \Psi)^3}\right) \\ & - \frac{PE}{2}\sin(\psi - \bar{\phi})\left(\frac{\cos \Psi}{\pi - \Psi} + \frac{\sin \Psi}{(\pi - \Psi)^2}\right) = 0. \end{aligned} \quad (4.34)$$

(4.34) is solved numerically for Ψ , using the Matlab function `fzero`. Parameter P is again found by fitting to the Maier-Saupe optical surfaces using Matlab function `lsqcurvefit`. In Figure 4.7 (a), (b), (c) and (d) the optic axis and birefringence surfaces over $[E, T]$ of the fitted $d\phi$ model and the MS model are shown. Visually it appears that the $d\phi$ model matches the MS model reasonably well. The mean relative errors calculated tell us that the optic axis is not as well fitted as the birefringence. The optic axis is within approximately 15.6% of the MS model, while the birefringence is within 1% of the MS model. In Figure 4.7 (e) and (f), the relative error for optic axis and birefringence is represented by a filled contour surface. The worsening of the fit from the previous stage to the current may indicate that the expression for the spontaneous polarisation is not accurately describing the MS electric field interaction, or that the stepwise nature of this fitting process is inadequate. A new method we look at is at the other end of the spectrum in terms of analysis. For comparison purposes we note that the final fitted parameters for the systematic method are $(T_a = 0.2485, a = 0, b = 0.01095, c = 0, P = 10.8240)$ with a fitting time of 80 seconds.

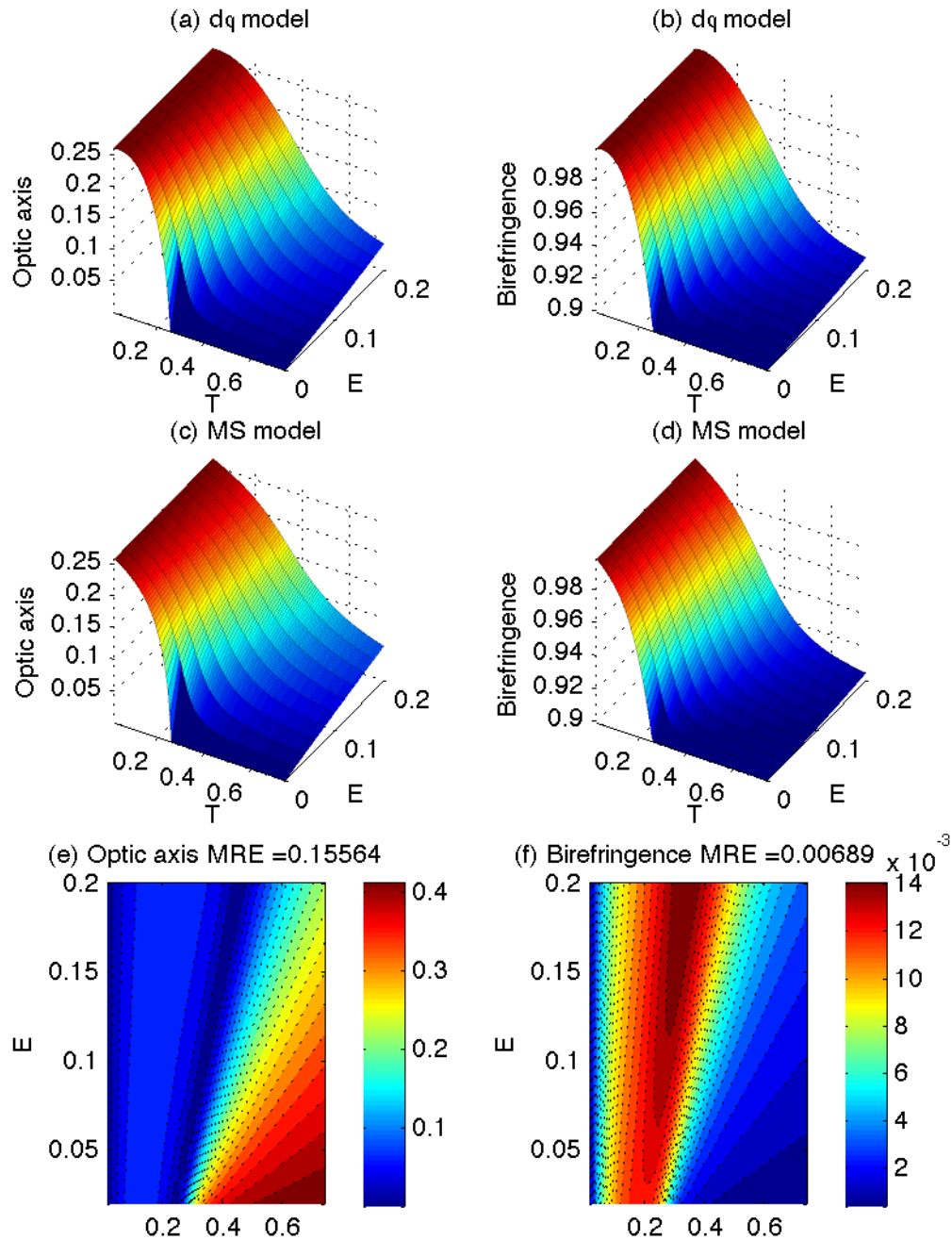


Figure 4.7: The Matlab function `lsqcurvefit` fits P , the final step of the systematic method, using the $[E, T]$ optical properties surfaces. The mean relative error contours are shown.

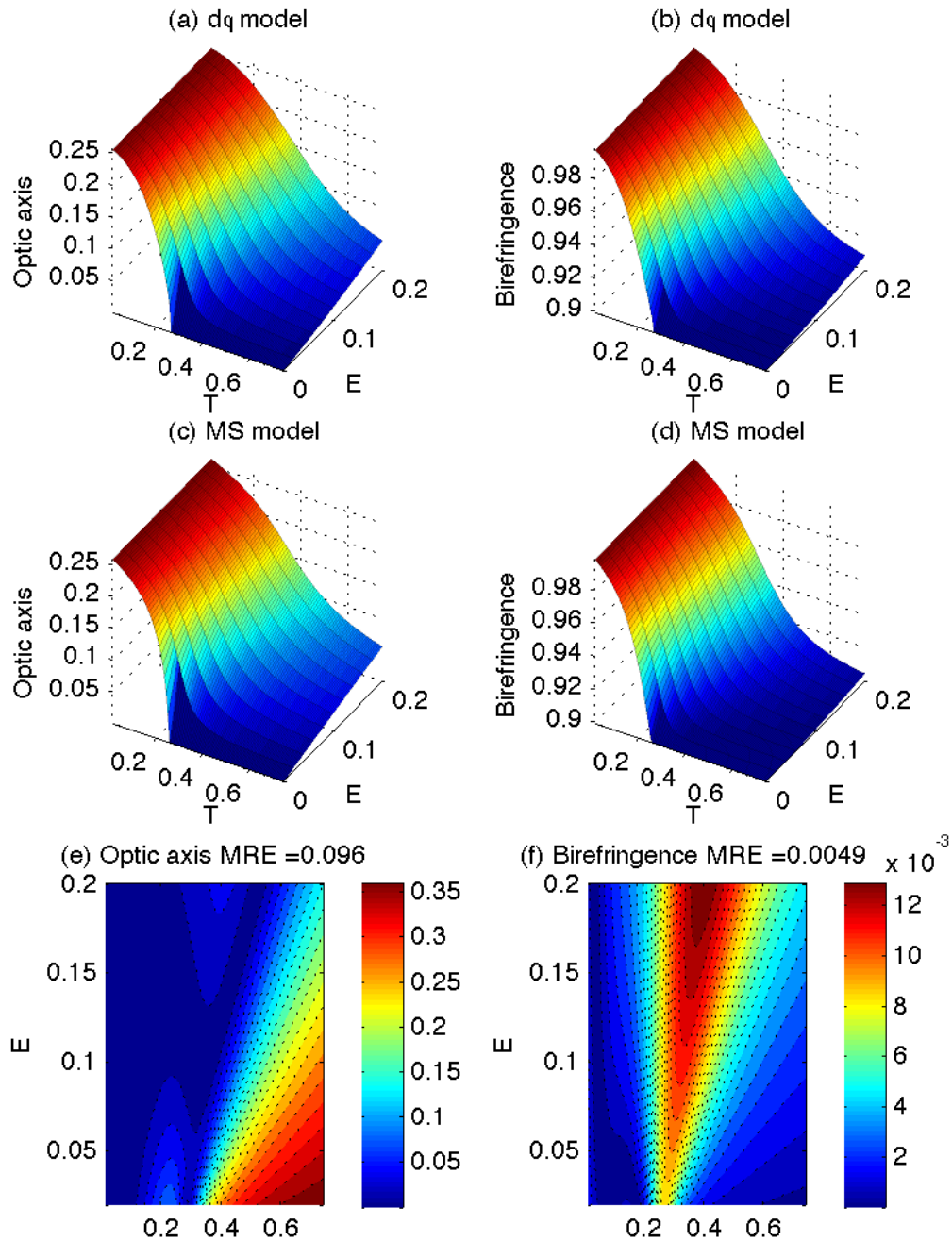


Figure 4.8: The brute force method fits all 5 $d\phi$ parameters using the Matlab function `lsqcurvefit` and the $[E, T]$ optical properties surfaces. The mean relative error contours are shown.

4.3.2 Brute force method

Section 4.3.1 detailed a fitting procedure that aimed to limit the computation time by reducing the number of parameters to be fit from five to three. The remaining three parameters were fitted systematically simplifying the job of the Matlab function `lsqcurvefit`. In this section we instead fit all the parameters simultaneously. As before we first need to find the functional form of $\Psi \in [0, \pi]$ by solving, using `fzero`,

$$0 = 2(T - T_a)\Psi + 3a\Psi^2 + 4b\Psi^3 + 2c \left(\frac{\sin \Psi \cos \Psi}{(\pi - \Psi)^2} + \frac{\sin^2 \Psi}{(\pi - \Psi)^3} \right) - \frac{PE}{2} \sin(\psi - \bar{\phi}) \left(\frac{\cos \Psi}{\pi - \Psi} + \frac{\sin \Psi}{(\pi - \Psi)^2} \right). \quad (4.35)$$

The optic axis (4.17) and birefringence (4.18) are derived using Ψ and `lsqcurvefit` then fits the five parameters (T_a, a, b, c, P) . The resulting fit is shown in Figure 4.8. The surface fittings are almost identical to the systematic method and the calculated mean relative error is of the same magnitude also, optic axis has 9.5% error and birefringence has 0.5% error. The fitted parameters had values: $T_a = 0.3148$, $a = -0.0379$, $b = 0.0288$, $c = 0.5403$, $P = 11.5696$, and a fitting time of 105 seconds. The fitting time of the brute force method is 25% greater than the previous method that used analysis to reduce the number of unknown parameters. However, the mean relative error of the brute force approach is two thirds that of the systematic approach. We see a notable difference in the values of the parameters after fitting. This would suggest that there could be a certain level of degeneracy present. Degeneracy is where there is a range of values for the unknown parameters that give a good fit, but these are dependent on the fitting routine, tolerances chosen and the initial guess as to the parameter value. We examined

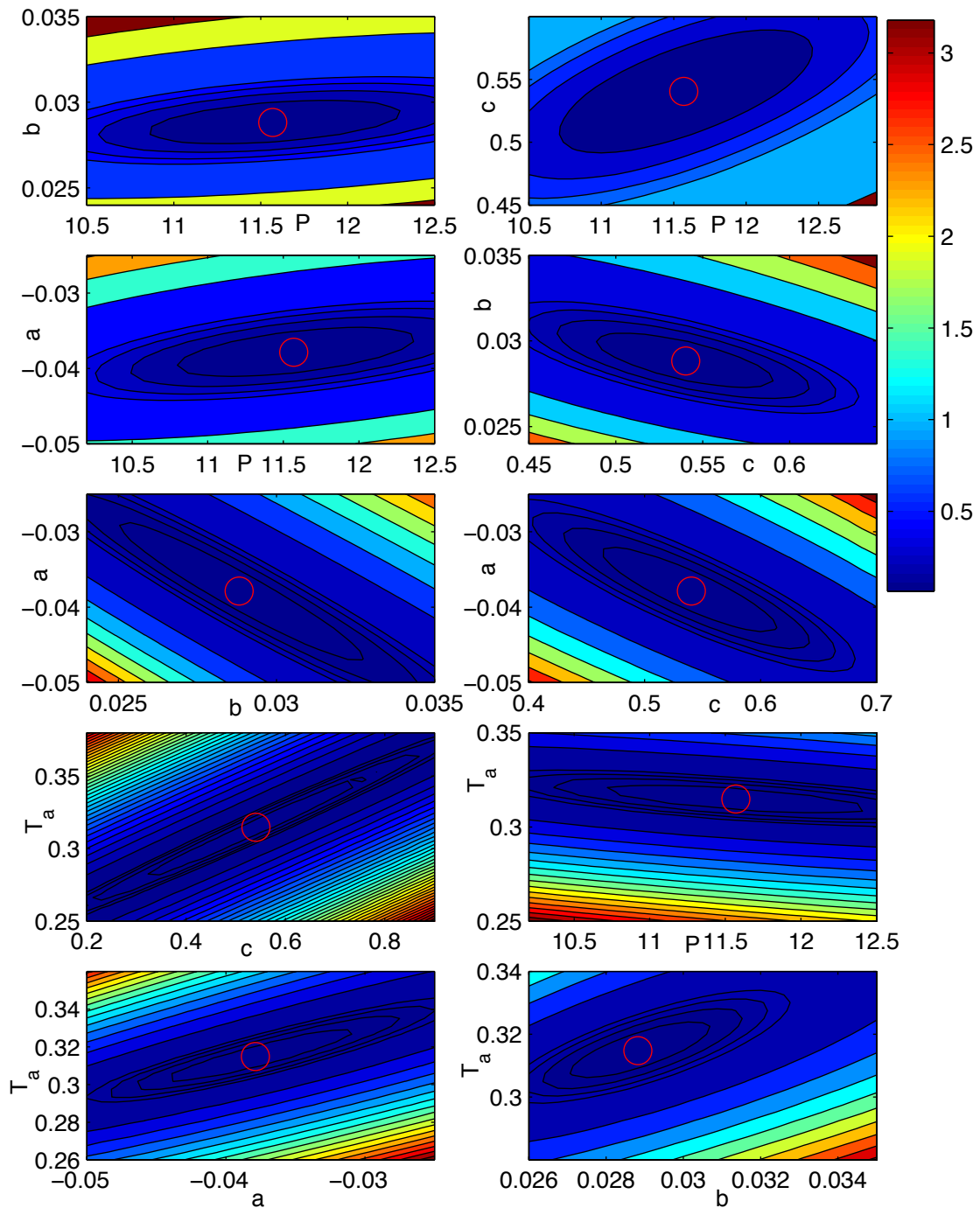


Figure 4.9: Systematically we fixed three of the model parameters and calculated the SSRE while varying the fourth and fifth parameters. The red circle is the value of the parameter pair chosen by `lsqcurvefit`.

the extent of degeneracy in the model in Figure 4.9. The five parameters found using the brute force method are used as the base parameter set. In Figure 4.9 we varied a combination of two parameters systematically while fixing the remaining parameters and calculated the sum of squares of residuals, SSRE (4.21). The pair of parameters chosen by the brute force algorithm matches the minimum level of the contour plots. This suggests that the fitting algorithm is successful in choosing the minimum set of parameters at least to this degree. However, we can see that many of the contours have minimum levels that could include a broad range of parameter pairs. This is important since there exist directions in parameter space in which linear combinations of parameters can be varied with very little change in error. If theoretical results are to be used in conjunction with experimental data, or to predict material behaviour, these degenerate directions should be checked to ensure that the results of the model do not vary significantly. For instance, from Figure 4.9 (top-right subplot) we see that varying a certain linear combination of c and P will leave the error almost unchanged. It will be important to check that using different combinations of parameters along this direction in parameter space will not affect the resulting simulations of a real device.

In future sections of this Chapter we will only consider the brute force method of parameter fitting. The time saving benefit of the systematic approach is not significant enough in absolute terms to discard the reduction in MRE of the brute force approach.

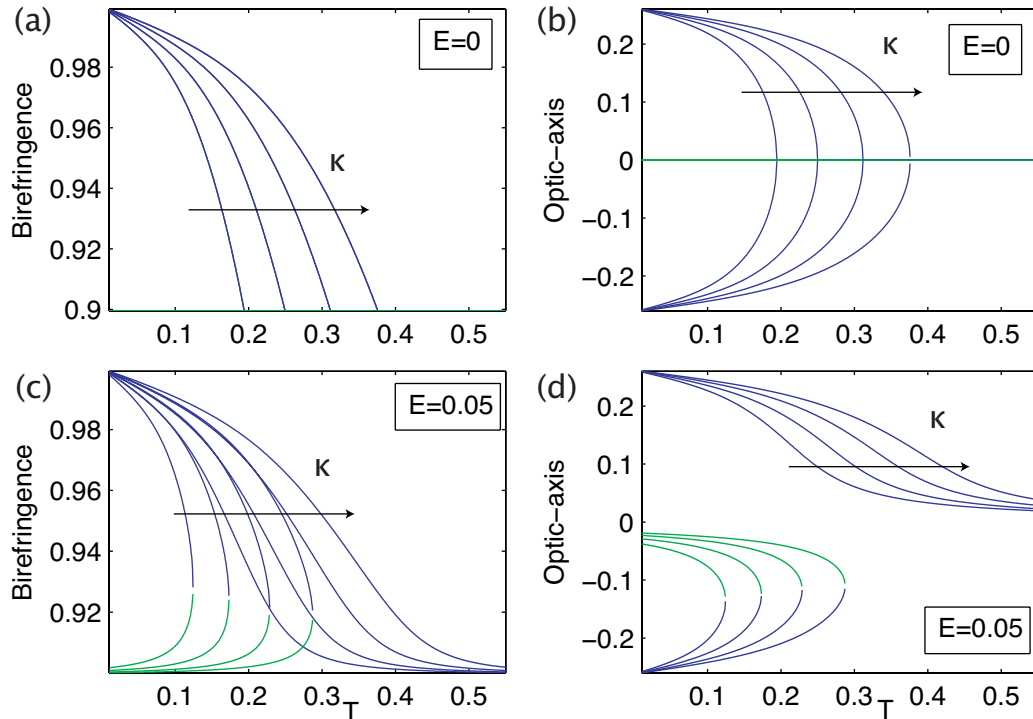


Figure 4.10: The MS optic axis and birefringence versus temperature with and without an electric field are calculated for increasing values of the Gay-Berne molecular parameter κ , the free energy is at a minimum when blue and a saddle point when green.

4.3.3 Investigation of molecular model parameters

In Chapter 3 we investigated the effect of altering the parameters of the Gay-Berne and dipole-dipole pair potentials on the order parameter phase diagrams of the Maier-Saupe free energy. For example, in Figure 4.10 we draw the optic axis and birefringence of the material versus temperature in the absence and presence of an electric field whilst varying κ , the molecular length-breadth ratio. The predominant feature when changing any of the molecular parameters is the change in the critical temperature when $E = 0$. This was most evident when varying κ and d_{\perp} the dipole strength. Using the brute force fitting routine described in section

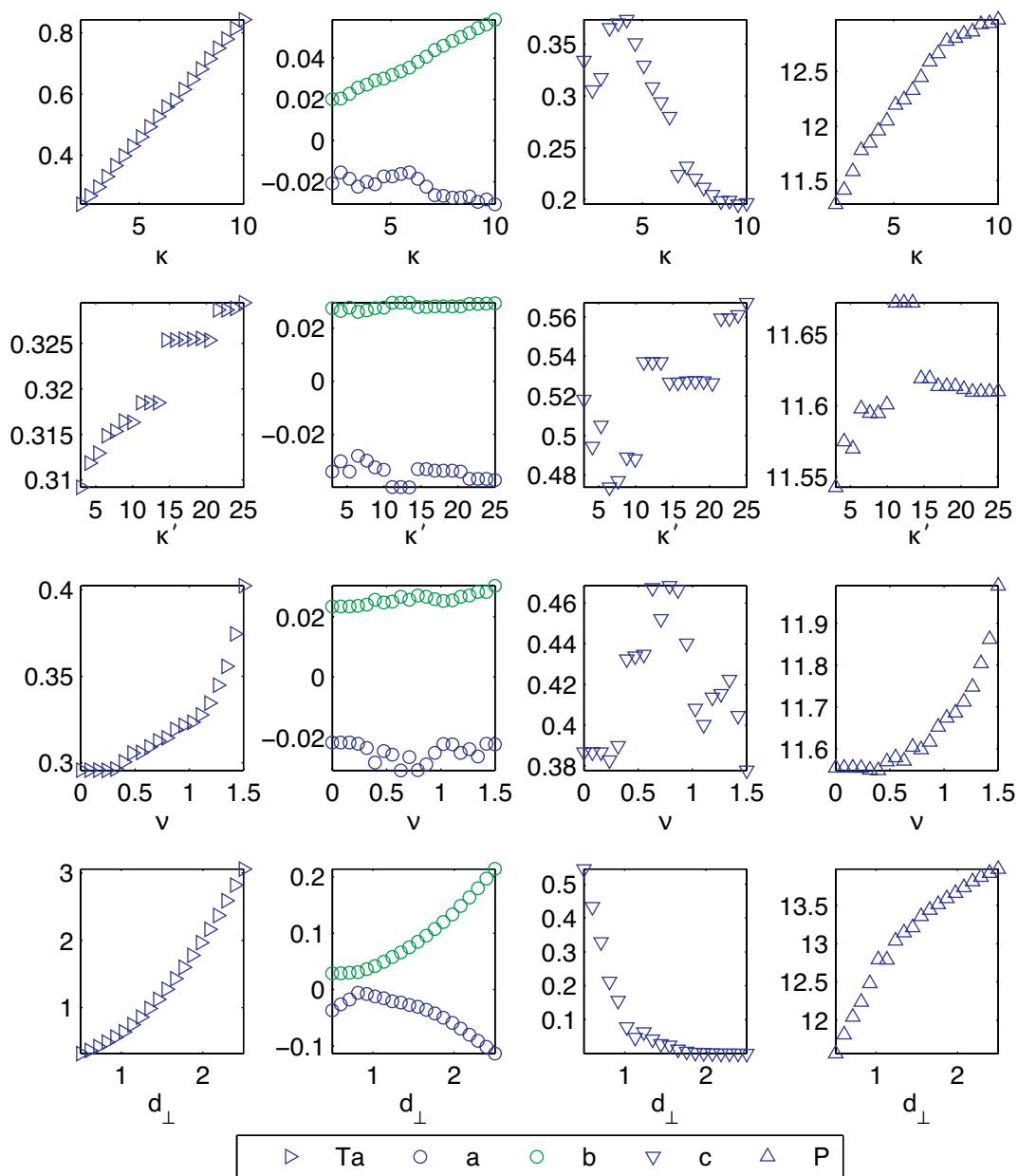


Figure 4.11: The effect of varying the four molecular parameters of the Gay-Berne and dipole-dipole potentials on the fitted $d\phi$ model parameters are shown. The κ and d_{\perp} parameters cause greatest $d\phi$ parameter variation

4.3.2 we fit the optic axis and birefringence surfaces for the MS free energy while varying the four parameters. The results are given in Figure 4.11. When we vary all four molecular parameters T_a follows qualitatively the change in T_{MS} , the MS transition temperature. As we expected when κ and d_{\perp} are varied we see greater parameter variation of (a, b, c) while (a, b, c) remain approximately constant when κ' , the well-depth ratio, and ν , the dipole location, are varied. The degeneracy of the $d\phi$ model may be contributing to the plateauing of the model parameters when κ' is varied. In conclusion, the fitting process we have chosen appears to be capturing the characteristics exhibited by the Maier-Saupe free energy of Chapter 3. In the next Section we will investigate the dynamic properties of the $d\phi$ model. Switching studies will reveal the influence of the Gay-Berne and dipole-dipole potentials on the optoelectric properties of the $d\phi$ model.

4.4 Dynamic analysis of a liquid crystal cell switching

In this Section we carry out switching studies that will investigate what effect the parameters of the Gay-Berne (2.5) and dipole-dipole (2.9) potentials have on the optical properties of the $d\phi$ model. The switching study will begin with the construction of a simple model of a liquid crystal device. The cell is a region of liquid crystal sandwiched between two surfaces across which a voltage will be applied to change the orientation of the director, as illustrated in Figure 4.12. Surface anchoring on both plates will cause the molecules to lie flat on the surfaces. This means that the Sm cone will only allow two stable equilibrium states at the surfaces. Thus a bistable device can be created.

Our previous free energy (4.9) will be augmented by the addition of a surface effect

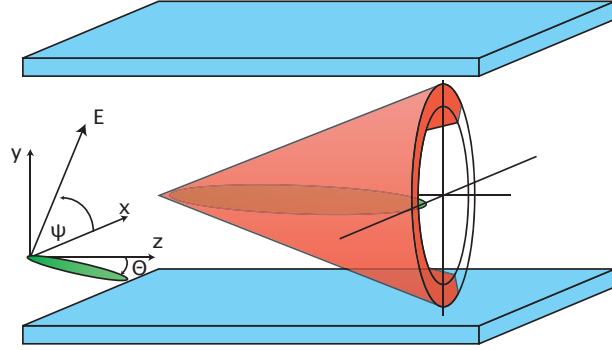


Figure 4.12: The cell of our device. The tilt angle (Θ) of the director (green) is measured from the z axis, the electric field angle (ψ) is measured in the xy plane from the x axis.

term, G_{SA} , to represent the anchoring present at the boundaries to force bistability in the device,

$$\begin{aligned}
 G_d &= G_{therm} + G_{inter} + G_{elec} + G_{SA} \\
 &= a_0(T - T^*)\Psi^2 + a\Psi^3 + b\Psi^4 \\
 &\quad + \frac{P^2 \sin^2 d\phi}{2\chi} \frac{d\phi}{d\phi^2} - \frac{EP \sin d\phi}{2} \frac{d\phi}{d\phi} \sin(\psi - \bar{\phi}) + s_e \sin^2 \bar{\phi}. \quad (4.36)
 \end{aligned}$$

The G_{SA} term will have minima at $\bar{\phi} = 0, \pi$. With this free energy we can now look at the dynamics of how the molecular orientation changes when an electric field is applied. Once we have modelled the dynamics we can begin to quantify and understand the operating voltages and switching characteristics of a bistable cell using τV -plots, which we will explain later.

The governing equations for the dynamics are found by assuming that the rate of change of both $\bar{\phi}$ and $d\phi$ are proportional to the gradient of the free energy at that

point [49],

$$\gamma_{\bar{\phi}} \frac{\partial \bar{\phi}}{\partial t} = -\frac{\partial}{\partial \bar{\phi}} G_d(\bar{\phi}, d\phi), \quad (4.37)$$

$$\gamma_{d\phi} \frac{\partial d\phi}{\partial t} = -\frac{\partial}{\partial d\phi} G_d(\bar{\phi}, d\phi). \quad (4.38)$$

The viscosity of the rotation of the distribution around the Sm cone is $\gamma_{\bar{\phi}}$ and the viscosity of the spreading motion of the distribution is $\gamma_{d\phi}$.

4.4.1 Forward Euler time discretisation

To solve the coupled system (4.37, 4.38) we used the forward Euler numerical method to approximate the partial derivatives $\frac{\partial \bar{\phi}}{\partial t}$ and $\frac{\partial d\phi}{\partial t}$. Calculating the Taylor series expansion in time of $\bar{\phi}_{i+1}$ gives the approximation

$$\bar{\phi}_{i+1} = \bar{\phi}_i - \frac{dt}{\gamma_{\bar{\phi}}} \left(2s_e \sin \bar{\phi}_i \cos \bar{\phi}_i - \frac{PE \sin d\phi_i}{2} \frac{\cos(\bar{\phi}_i - \psi)}{d\phi_i} \right), \quad (4.39)$$

by equation (4.37). Similarly, for $d\phi_{i+1}$ we have

$$\begin{aligned} d\phi_{i+1} = d\phi_i - \frac{dt}{\gamma_{d\phi}} & \left[-2a_0(T - T_a)(\Psi_i) - 3a(\Psi_i)^2 - 4b(\Psi_i)^3 \right] \\ & - \frac{dt}{\gamma_{d\phi}} \left[2c \frac{\sin d\phi_i}{d\phi_i^2} \left(\cos d\phi_i - \frac{\sin d\phi_i}{d\phi_i} \right) \right] \\ & - \frac{dt}{\gamma_{d\phi}} \left[\frac{EP \sin(\bar{\phi}_i - \psi)}{2d\phi} \left(\cos d\phi_i - \frac{\sin d\phi_i}{d\phi_i} \right) \right]. \end{aligned} \quad (4.40)$$

We now have the dynamic equations of our model approximated using the forward Euler method in equations (4.39) and (4.40). At each timestep i , the right hand side of (4.39) and (4.40) are computed using $\bar{\phi}_i$, $d\phi_i$ and $dt = t_{i+1} - t_i$, to compute

$\bar{\phi}_{i+1}$ and $d\phi_{i+1}$. In order to maintain numerical stability of this method we need a relatively small time step size.

4.4.2 Adaptive time

Initial attempts to solve our system of equations used a timestep size of dt which remained constant throughout each simulation. We were forced to choose a dt which was small enough to approximate the solution at times when the gradients of the free energy were steepest, $E > 0$. This meant that our computation time was inefficient when $E = 0$, as the relaxed gradient would allow a larger timestep to be used.

To combat this problem, we have employed an adaptive time-stepping algorithm based on [50]. The algorithm involves calculating two approximations ($y_1 = (\bar{\phi}_1, d\phi_1)$, $\hat{y}_1 = (\hat{\phi}_1, d\hat{\phi}_1)$) to the solution of system (4.37, 4.38), and calculating the error for the less precise result. The first approximation (y_1) is calculated by solving (4.39) and (4.40) iteratively for two timesteps of size dt . The second approximation (\hat{y}_1) is calculated by solving (4.39) and (4.40) for one timestep of size $2dt$. We estimate the error of the less precise approximation as $|y_1 - \hat{y}_1|$, which we use to calculate an optimal step size,

$$dt_{\text{new}} = dt \times \min \left(\text{facmax}, \max \left(\text{facmin}, \text{fac} \cdot \left(\frac{sc}{|y_1 - \hat{y}_1|} \right)^{\frac{1}{2}} \right) \right), \quad (4.41)$$

where facmax and facmin are the maximum and minimum scaling factors for dt . When $|y_1 - \hat{y}_1| < sc$, where sc is a user defined tolerance, we accept the computed step and we advance the solution with y_1 and dt_{new} , otherwise we reject the

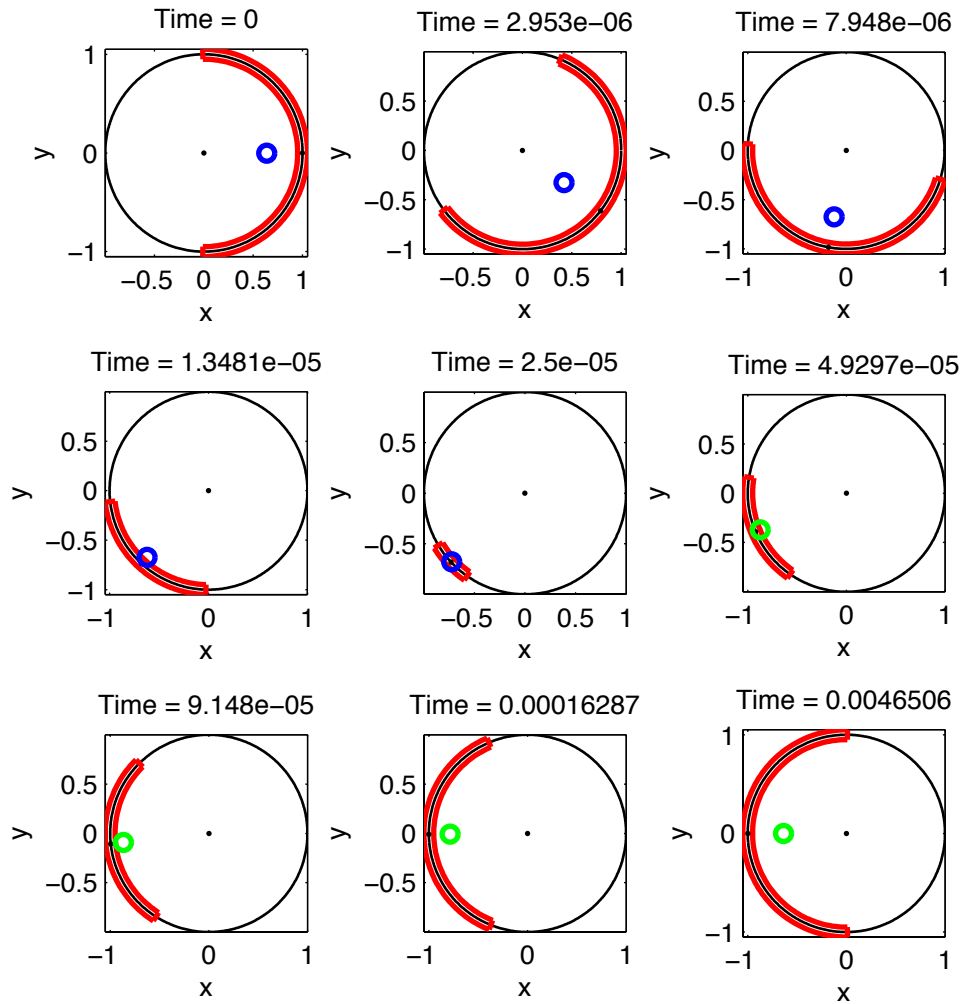


Figure 4.13: An electric field is applied with $\psi = -\frac{\pi}{4}$. The bulk initially spreads out around the cone while the centre, $\bar{\phi}$, rotates towards $-\frac{\pi}{4}$ (time= $2.953e-06$). When $\bar{\phi}$ passes $-\frac{\pi}{4}$ the bulk contracts until $\bar{\phi} = -\frac{3\pi}{4}$, which is when the molecular dipole is aligned with ψ (time = $2.5e-05$). The field is turned off and the bulk and centre move towards equilibrium (time= 0.0046506). The director is given as the blue ring (electric field on) and the green ring (electric field off)

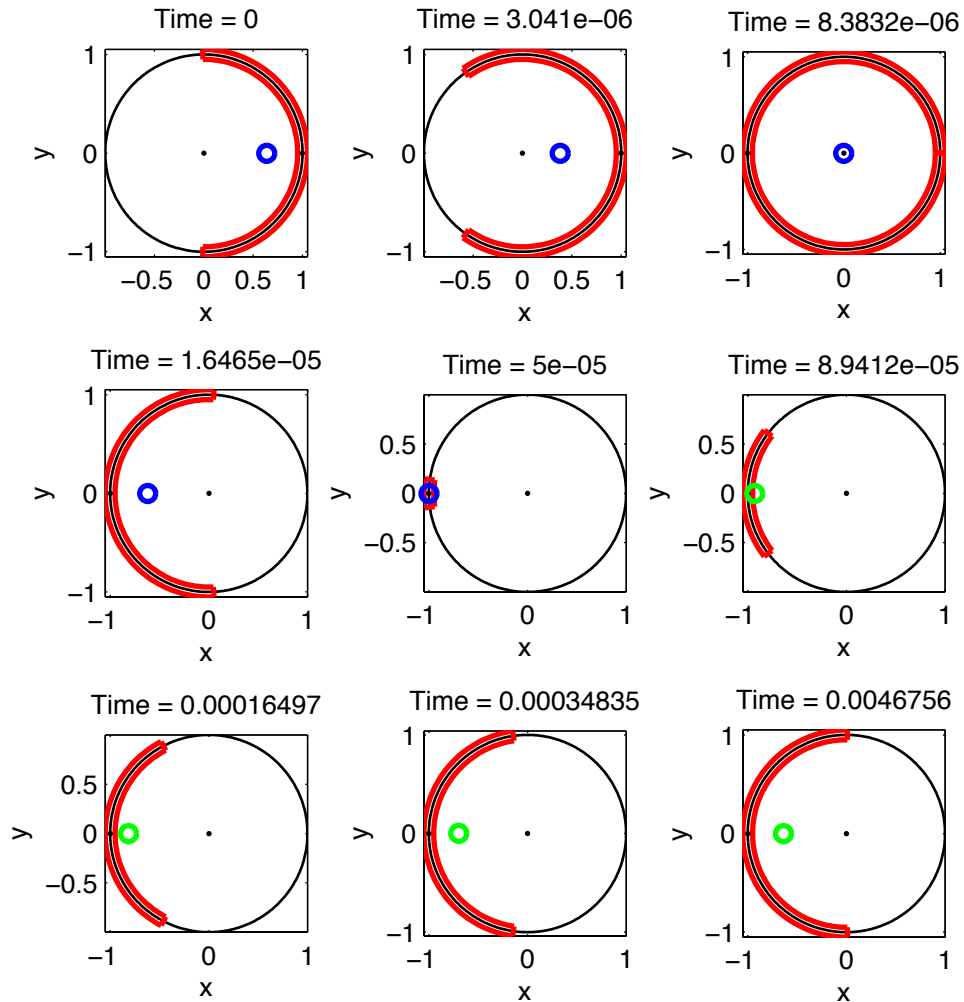


Figure 4.14: An electric field is applied with $\psi = -\frac{\pi}{2}$. The bulk spreads out around the cone (time=3.041e-06). When $d\phi > \pi$ the centre is switched to $\bar{\phi} = \pi$ (time=8.3832e-06) which causes the bulk to contract to allow alignment with the field (time=5e-05). The field is turned off and the bulk moves toward equilibrium (time=0.0046756). The director is given as the blue ring (electric field on) and the green ring (electric field off)

computed step and use dt_{new} to compute new approximations (y_1, \hat{y}_1) . The safety factor, fac , determines how cautious the next time step will be depending on acceptance or rejection of the computed step. We will use the values $\text{facmax} = 2.5$, $\text{facmin} = 0.1$, $\text{fac} = 0.8$ and $sc = 5 \times 10^{-4}$ and $\text{facmax} = 1$ after a step rejection.

In Figure 4.13 we give an example of the motion of the bulk when an electric field is applied at an angle. The electric field is applied at an angle of $\psi = -\frac{\pi}{4}$ so we expect the dipole of the system to align with the field. This would mean that the molecules should align at the azimuthal angle of $-\frac{3\pi}{4}$. The electric field forces the centre of the molecular distribution to move around the cone. As $\bar{\phi} \rightarrow -\frac{\pi}{4}$ the bulk expands and $d\phi \rightarrow \pi$. Once $\bar{\phi} < -\frac{\pi}{4}$ the bulk contracts and $d\phi \rightarrow 0$. When the electric field is turned off the surface effect pulls the centre to $\phi = \pi$ while the bulk of the molecular distribution moves to equilibrium. The coordinates of the director are calculated using the optic axis (4.17), a circle radius of 1 and a fixed cone tilt angle $\theta_0 = \frac{\pi}{12}$, for the distance from the centre, and ϕ for the angle. The (x, y) coordinates are therefore,

$$\text{director}(x, y) = \left(\left| \frac{\tan(\Theta)}{\tan(\theta_0)} \right| \cos(\bar{\phi}), \left| \frac{\tan(\Theta)}{\tan(\theta_0)} \right| \sin(\bar{\phi}) \right). \quad (4.42)$$

In Figure 4.14 an electric field is applied at an angle of $\psi = -\frac{\pi}{2}$ so we expect the molecules to align at the opposite side of the cone. This causes the bulk to expand around the cone. However, the equilibrium value of $d\phi$ in this case is greater than π . Therefore, when $d\bar{\phi} > \pi$ we switch $\bar{\phi}$ to π which causes the bulk to contract and $d\phi \rightarrow 0$. When the electric field is turned off the bulk of the molecular distribution moves to equilibrium.

We now have the algorithm in place to solve the system of dynamic equations (4.37, 4.38). Before carrying out a τV study of the optic characteristics in relation to time and voltage, we will look at how we can relate the rotational viscosities to the Maier-Saupe potential of Chapter 3.

4.4.3 Rotational viscosity

In this Chapter we have created a simple phenomenological model which we hoped to relate to the Maier-Saupe model of Chapter 3. So far we have matched one model's optical characteristics to the other in the equilibrium case. We now investigate the dynamic behaviour of the $d\phi$ model while varying the Gay-Berne and dipole-dipole model parameters. To solve the dynamic equations (4.37) and (4.38) we introduce two new variables representing the rotational viscosity of the model. We will now go on to calculate the rotational viscosity of the Maier-Saupe potential and use it in the $d\phi$ model approximation.

The dynamic behaviour of our model depends on the torque generated by an applied electric field and the viscosity dependent on reorientating the molecules about the Sm cone (4.37) and (4.38). The rotational viscosities are proportional to the tilt angle of the Sm cone θ [51],

$$\gamma_\phi, \gamma_{d\phi} \propto \lambda_0 \sin^2 \theta, \quad (4.43)$$

where λ_0 is proportional to the microscopic friction constant. Osipov [52] obtained an expression for λ_0 in terms of the nematic order parameter S and the microscopic friction constant, λ . A simplified one-particle mean field potential in the Maier-

Saupe form was chosen,

$$U_{MF}(\mathbf{a}) = -J_0 S P_2(\mathbf{a} \cdot \mathbf{n}), \quad \langle U_{MF}(\mathbf{a}) \rangle = -J_0 S^2, \quad (4.44)$$

where S , in tensor notation, is the nematic order parameter defined as the average

$$S = \langle P_2(\mathbf{a} \cdot \mathbf{n}) \rangle, \quad (4.45)$$

P_2 is the second order Legendre polynomial, \mathbf{n} is the unit vector of the director and \mathbf{a} is the long axis of a molecule. The rotational viscosity coefficient can be calculated for (4.44) as

$$\lambda_0 = \frac{1}{70} \rho \lambda (7 + 5S) \frac{(J_0 S / kT)^2}{2 + J_0 S / kT}, \quad (4.46)$$

where ρ is the number density and k is the Boltzmann constant. However, the Maier-Saupe mean-field potential (3.18) we chose in Chapter 3 is of a different form to this so we will have to manipulate these expressions to suit our form.

We defined our potential (3.18) using the order parameters (V, B) . Gorkunov et al. [21] gave expressions for the nematic order parameter S , nematic tensor biaxiality P and optic axis Θ , in terms of (V, B) :

$$\tan 2\Theta = \frac{V}{Sk - 0.5B}, \quad (4.47)$$

$$S = \frac{1}{4} S_k + \frac{3}{8} B + \frac{3V}{4 \sin 2\Theta}, \quad (4.48)$$

$$P = \frac{1}{2} S_k + \frac{3}{4} B - \frac{V}{2 \sin 2\Theta}. \quad (4.49)$$

Here

$$S_k = \langle P_2(\cos \theta_0) \rangle, \quad B = \sin^2 \theta_0 \langle \cos 2\phi \rangle, \quad V = \sin 2\theta_0 \langle \cos \phi \rangle, \quad (4.50)$$

where (ϕ, θ_0) are the azimuthal and cone tilt angle respectively. We have an expression for S in terms of our order parameters (4.48) but we still require the coefficient, J_0 , of S^2 in (4.44), in terms of our model. In Chapter 3 (3.18) can be simplified and then averaged to give

$$\langle U_{MF} \rangle = C + \alpha B^2 + \beta V^2, \quad (4.51)$$

C was a constant term encapsulating S_k , (α, β) were coefficients dependent on molecular parameters. Solving the system of equations (4.47, 4.48, 4.49) in terms of (S_k, B, V) , we obtain,

$$V = \frac{1}{2} \sin 2\Theta S, \quad B = P + \frac{1}{4}(1 - \cos 2\Theta)S, \quad S_k = \frac{1}{2}P + \frac{1}{8}(1 + 3 \cos 2\Theta)S. \quad (4.52)$$

We can substitute these expressions for (V, B) to find the coefficient S^2 in terms of (α, β) . Therefore

$$J_0 = \frac{\alpha}{4} \sin^4 \Theta + \frac{\beta}{4} \sin^2 2\Theta. \quad (4.53)$$

The rotational viscosity (4.43) can now be approximated using the molecular parameters and model order parameters we have discussed in the previous two Chapters. The dependence of the rotational viscosity coefficient (4.46) on the molecular parameters is shown in Figure 4.15. In Figure 4.15 (a) and (d) we can see that

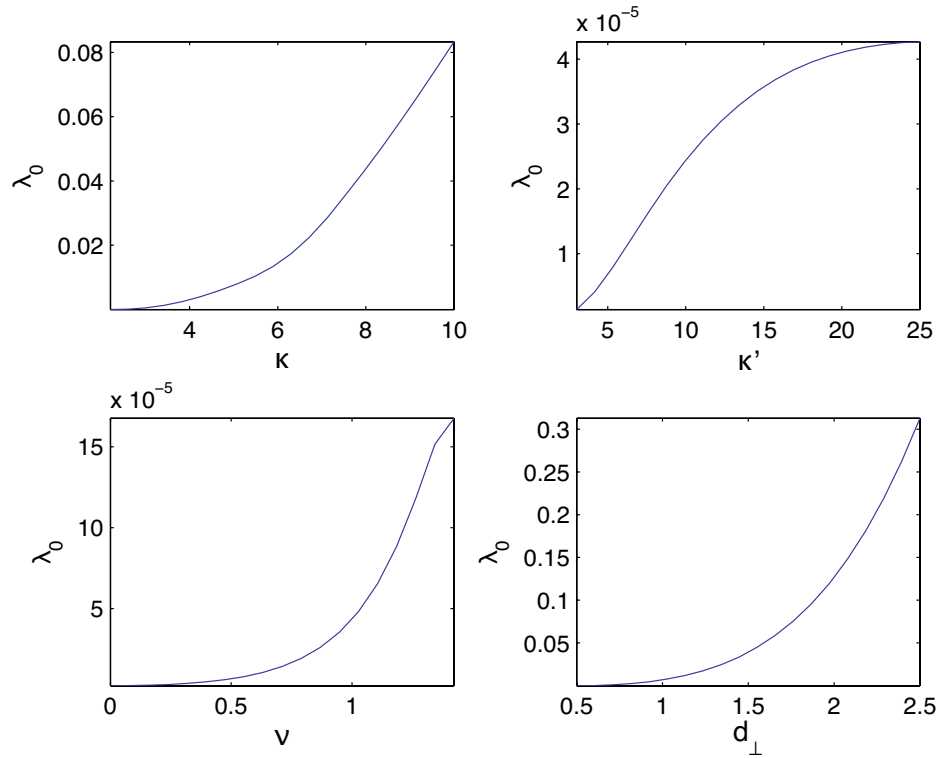


Figure 4.15: The rotational viscosity constant λ_0 calculated while varying the molecular parameters from base set of parameters ($\kappa = 3, \kappa' = 5, \nu = 0.6, d_{\perp} = 0.5$): (a) the molecular length-breadth ratio κ , (b) well depth ratio κ' , (c) dipole location ν , and (d) dipole strength d_{\perp} , respectively. ($T = 0.1883$).

κ and d_{\perp} have greatest effect on the rotational viscosity. This is as we would expect given the dependence of λ_0 on S and, in turn, on the MS order parameters B and V . As the molecular length-breadth ratio increases, λ_0 increases almost linearly. As the well-depth ratio κ' increases, the effect on λ_0 appears to level out, parameter λ_0 changes more rapidly for variations at low κ' , Figure 4.15 (b). The dipole location ν and dipole strength d_{\perp} have similar relationships with λ_0 , Figure 4.15 (c) and (d). λ_0 varies more dramatically when the dipole location, ν , moves towards the end of the molecule of length 1.5. Dipole strength has most effect on viscosity than all other molecular parameters.

4.4.4 τV -plot generation

A bistable liquid crystal device has the ability to switch from one state to the other depending on the strength and length of time that an electric field is applied. This behaviour can be graphed using a τV -plot which indicates where a bistable cell switches between states when a specific voltage, V , is applied for a period of time, τ . The τV -plot shows where in the parameter space switching from one state to the other occurs. With these plots we can quantify and understand the operating voltages and switching characteristics of a bistable cell.

To create the τV -plot we will use the brute-force method from section 4.3.2 in finding the switching regions. The test region is a 2D array made up of discrete voltages and pulse times. At each point of the array we test whether or not the system switches. The approximated region produced by this method will be dependent on the degree of discretisation present. However, we choose this method due to the relative ease of coding.

In section 4.3.3 we investigated the effect altering the parameters of the Gay-Berne and dipole-dipole pair potentials had on the parameter values of the $d\phi$ model, Figure 4.11. We now look at what effect this has on the dynamic behaviour of the model. In Figure 4.16 an electric field was applied with $\psi = -\frac{\pi}{2}$ for various voltages V and pulse lengths τ . The base state of the model was the steady state spread $d\phi$ and the surface anchoring orientation $\bar{\phi} = 0$. The Figure shows the voltage and pulse length it is necessary to apply for the bulk average azimuth orientation to switch to $\bar{\phi} = \pi$. A different molecular parameter is varied in each plot with the remaining parameter values taken from the base set ($\kappa = 3, \kappa' =$

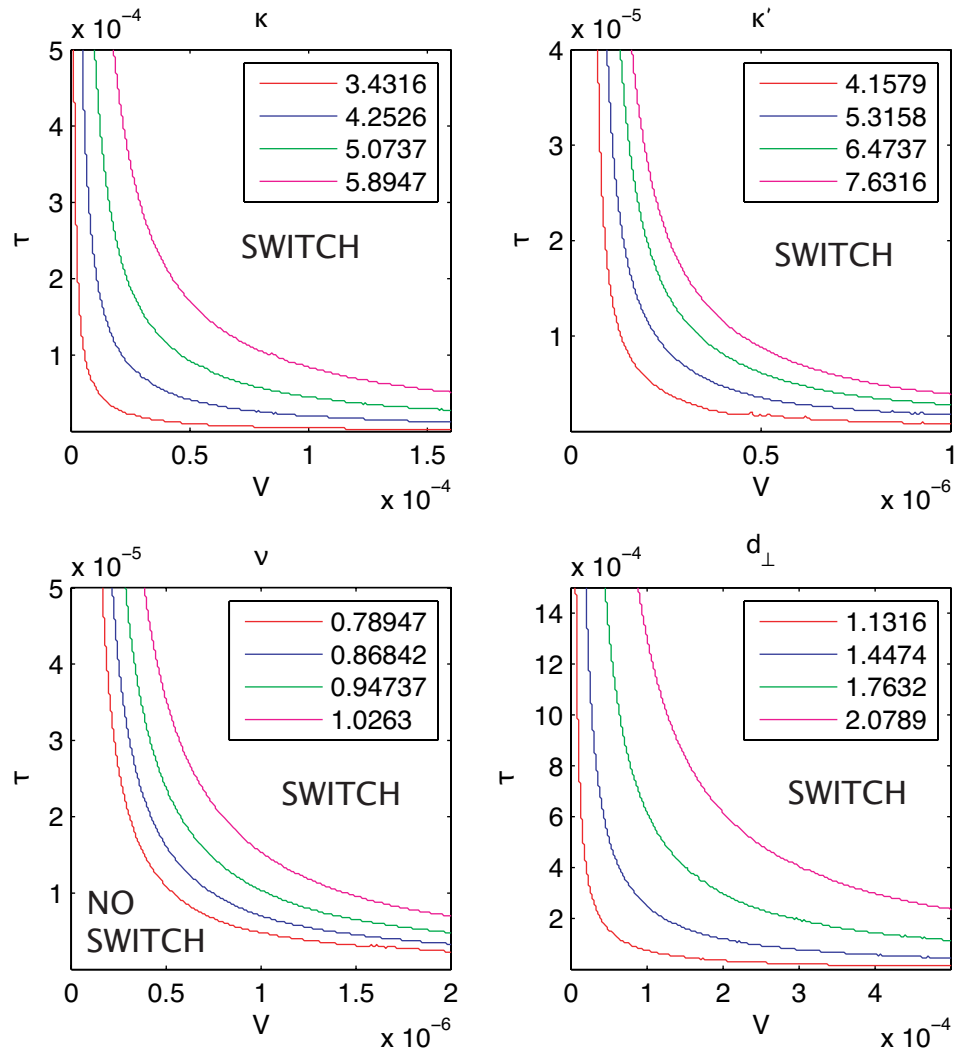


Figure 4.16: τV -plots showing the effect of varying molecular parameters: κ length-breadth ratio, κ' side-side to end-end well depth ratio, ν dipole location and d_{\perp} dipole strength. The boundary of the switching region is shown for each variation of the tested parameter. Only small variation in τV -plots are exhibited for κ' and ν . The most significant variations are for κ and ν .

5, $\nu = 0.6$, $d_{\perp} = 0.5$). The temperature in each graph was chosen as $T = 0.97T_{MS}$ when the first parameter of the set was used. The largest variation in switching came from varying κ and d_{\perp} . Increasing κ and d_{\perp} makes it harder to switch from one state to the other. We calculated in Figure 4.15 that the rotational

viscosity had a greater dependence on κ and d_{\perp} , which would obviously reduce switching for those parameters as they increase. Finally, we know that the optic axis and birefringence increase, more greatly for a fixed temperature, when κ and d_{\perp} increase as opposed to κ' and ν . This means that the degree of order present in the system varies more when we vary κ and d_{\perp} than when we vary κ' and ν . It seems sensible to assume that the more ordered a system is, the more difficult it is to create disorder.

4.5 Summary

In this Chapter, we used a Landau - de Gennes theory to model the thermotropic phase transition of Sm A to Sm C. The order parameter was dependent on the spread of the molecules on the Sm cone. The distribution of molecules in the model was described by a uniform distribution of the azimuthal angle. The free energy included terms describing the self-interaction and the interaction with an external field of the spontaneous polarisation. We were able to calculate the optic axis and birefringence of the model as surfaces over temperature and applied electric field. The surfaces of the optical quantities were then fitted to the corresponding surfaces calculated using the free energy of the previous Chapter. We derived two fitting schemes, one which fit model parameters systematically, and one which fit all model parameters concurrently. After some testing we chose the latter method to perform the investigation into the effect of molecular parameters in Chapter 2.

Finally, we carried out switching studies looking at the dynamic behaviour of a bistable liquid crystal cell when varying the molecular parameters of the Gay-Berne and dipole-dipole potentials. The rotational viscosities of the dynamic equations

were found to depend on the order parameters in Chapter 3. We solved the dynamic equations using a forward Euler numerical method and employed an adaptive time-stepping algorithm to speed up the process. The results were displayed using τV -plots. We see significant variation in the switching regions of the τV -plots by varying the molecular parameters.

5 Conclusions

In this thesis, we have modelled de Vries type ferroelectric liquid crystals at various length-scales and various degrees of complexity, and are able to map physical molecular properties to the existence and optical characteristics of various states of the liquid crystals.

At the smallest length-scale we investigated potentials that could account for short and long range forces between two rod-like molecules. These were the Gay-Berne and dipole-dipole intermolecular interaction pair potentials. The Gay-Berne potential modelled the steric effect of the molecules and the van der Waals dispersion force, while the dipole-dipole potential modelled the long range force of dipole interactions. We investigated how intermolecular position and relative molecular orientation affect the standard GB(3, 5, 2, 1) potential and an arbitrary dipole-dipole potential ($\nu = 0.6$, $d_{\perp} = 0.5$). We then investigated the effect of the molecular parameters (κ , κ' , ν , d_{\perp}) after the potentials were integrated over the intermolecular vector so that the energy depended only on the relative orientation of the molecules. An analytic form of the potentials that depended only on the relative molecular orientation was found using Fourier decomposition. We compared the Fourier coefficients from the general decomposition to one using the Maier-Saupe form. We found that the Maier-Saupe potential was capable of being a reasonable approximation to the combination of the Gay-Berne and dipole-dipole potentials. The Fourier approximation of this combined potential would allow us to calculate coefficients of the Maier-Saupe model from the Gay-Berne and dipole-dipole potentials.

At the mesoscopic level the free energy is calculated using the Maier-Saupe pair potential and the mean-field theory. The mean-field theory allows us to approximate the numerous intermolecular interactions in the bulk of a liquid crystal material with a molecule interacting with an average energy. The phase behaviour of the model is described by the order parameters V and B , representing tilt and biaxiality respectively. The optical axis and birefringence were calculated using the order parameters. The temperature dependence of the order parameters, optical axis and birefringence can be displayed using phase diagrams. This meant that we have the capability to vary the parameters of the intermolecular potential and see the effect on the optoelectrical properties of the bulk of the material. In this way we have managed to link the two length-scales, allowing us to alter the molecular properties of our molecules and see what effect they have on the physical observables, of the bulk material, namely the optic axis and birefringence.

Next we described a simple model that allowed us to investigate device applications of a material. This phenomenological model used a Landau - de Gennes theory to model the thermotropic phase transition of smectic A to smectic C. The order parameter described the spread of the molecules on the smectic cone. A uniform distribution of the molecule's azimuthal angle was used. The free energy included terms describing the self-interaction and the interaction with an external field of the spontaneous polarization. We were able to calculate the optic axis and birefringence of the model as surfaces over temperature and applied electric field. The surfaces of the optical quantities were then fitted to the corresponding surfaces calculated using the free energy of Chapter 3. We derived two fitting schemes, one which fit model parameters systematically, and one which fit all model parameters concurrently. After some testing we chose the latter method to investigate the

effect of molecular parameters of the molecular interaction potentials.

Finally, using the phenomenological model we examined the switching characteristics of a ferroelectric liquid crystal cell when varying the molecular parameters of the Gay-Berne and dipole-dipole potentials. The rotational viscosities of the dynamic equations were found to depend on the order parameters of the Maier-Saupe potential. We solved the dynamic equations using a forward Euler numerical method and employed an adaptive time-stepping algorithm to speed up the process. The results were displayed using τV -plots, which display regions of no switching and switching.

The largest variation in switching region came from varying the molecular length, κ , and dipole strength, d_{\perp} . Increasing these parameters makes it harder to switch from one state to the other. We have shown that the rotational viscosity increased more greatly when we increased κ and d_{\perp} , which would obviously reduce switching for those parameters. Finally, we know that the optic axis and birefringence increases, at a given temperature, more greatly when κ and d_{\perp} increase as opposed to κ' and ν , see Figures 3.9, and 3.10. This means that the degree of order present in the system varies more when we vary κ and d_{\perp} than when we vary κ' and ν .

Regarding areas for improvement and further work, we could remove the restrictions we place on the geometry of our model. At present in both the Maier-Saupe free energy and the Landau - de Gennes free energy we prescribed a fixed tilt angle of the smectic cone and model only a single smectic layer with the molecules c.o.m. lying in the xy plane. We also chose a uniform distribution for the phenomenological model. We could investigate the implementation of a more complex distribution for the molecular azimuthal angles. Finally, we could expand our de-

vice model to two dimensions and investigate how different initial molecular states are affected by the location and shape of electric pulses.

Even though we have made many assumptions and used simple models, we have shown, in principle, that it is possible to vary molecular model parameters and be able to see how device properties change as a consequence.

A Calculating the Maier-Saupe pair potential

The Maier-Saupe effective interaction potential is a function of molecules ($\mathbf{a}_1, \mathbf{a}_2$) and the displacement vector between the centres-of-mass (c.o.m) of the two molecules (\mathbf{r}_{12}).

$$U_{eff}(\mathbf{a}_1, \mathbf{a}_2, \mathbf{r}_{12}) = J_0 - J_1(\mathbf{a}_1 \cdot \mathbf{a}_2)^2 + 2J_2(\mathbf{a}_1 \cdot \mathbf{a}_2)(\mathbf{a}_1 \cdot \mathbf{r}_{12})(\mathbf{a}_2 \cdot \mathbf{r}_{12}) - J_3(\mathbf{a}_1 \cdot \mathbf{r}_{12})^2(\mathbf{a}_2 \cdot \mathbf{r}_{12})^2 - J_{12}^2(\mathbf{a}_1 \cdot \mathbf{r}_{12})^2 - J_{21}^2(\mathbf{a}_2 \cdot \mathbf{r}_{12})^2, \quad (\text{A.1})$$

where, as stated previously (3.7) and (3.8),

$$\mathbf{a}_i = (\sin \theta_0 \cos \phi_i, \sin \theta_0 \sin \phi_i, \tau_i \cos \theta_0),$$

$$\mathbf{r}_{12} = (\cos \psi, \sin \psi, 0),$$

and we have assumed that all molecules lie on a cone with angle θ_0 .

To calculate the pair potential, depending only on the orientations of \mathbf{a}_i , we integrate the two particle potential over \mathbf{r}_{12} . Due to the form of (A.1) we can do this term by term. Before we integrate we will separate the brackets of the integrands. To reduce working we will refer to the three vectors: \mathbf{a}_1 , \mathbf{a}_2 , and \mathbf{r}_{12} by their (x, y, z) components. The terms that depend on \mathbf{r}_{12} and will be integrated

are:

$$\begin{aligned}
\mathbf{a}_i \cdot \mathbf{r}_{12} &= a_{ix}r_x + a_{iy}r_y, \\
(\mathbf{a}_i \cdot \mathbf{r}_{12})^2 &= a_{ix}^2r_x^2 + a_{iy}^2r_y^2 + 2a_{ix}a_{iy}r_xr_y, \\
(\mathbf{a}_1 \cdot \mathbf{r}_{12})(\mathbf{a}_2 \cdot \mathbf{r}_{12}) &= a_{1x}a_{2x}r_x^2 + a_{1y}a_{2y}r_y^2 + (a_{1x}a_{2y} + a_{1y}a_{2x})r_xr_y, \\
(\mathbf{a}_1 \cdot \mathbf{r}_{12})^2(\mathbf{a}_2 \cdot \mathbf{r}_{12})^2 &= a_{1x}^2a_{2x}^2r_x^4 + a_{1y}^2a_{2y}^2r_y^4 + 2(a_{1x}^2a_{2x}a_{2y} + a_{2x}^2a_{1x}a_{1y})r_x^3r_y \\
&\quad + 2(a_{1y}^2a_{2x}a_{2y} + a_{2y}^2a_{1x}a_{1y})r_xr_y^3 \\
&\quad + (a_{1x}^2a_{2y}^2 + a_{1y}^2a_{2x}^2 + 4a_{1x}a_{1y}a_{2x}a_{2y})r_x^2r_y^2.
\end{aligned}$$

We can now integrate all the terms of (r_x, r_y) over ψ :

$$\begin{aligned}
\int_{-\pi}^{\pi} r_x^2 d\psi &= \int_{-\pi}^{\pi} \cos^2 \psi d\psi = \pi, \\
\int_{-\pi}^{\pi} r_y^2 d\psi &= \int_{-\pi}^{\pi} \sin^2 \psi d\psi = \pi, \\
\int_{-\pi}^{\pi} r_x r_y d\psi &= \int_{-\pi}^{\pi} \cos \psi \sin \psi d\psi = 0, \\
\int_{-\pi}^{\pi} r_x^3 r_y d\psi &= \int_{-\pi}^{\pi} \cos^3 \psi \sin \psi d\psi = 0, \\
\int_{-\pi}^{\pi} r_x r_y^3 d\psi &= \int_{-\pi}^{\pi} \cos \psi \sin^3 \psi d\psi = 0, \\
\int_{-\pi}^{\pi} r_x^2 r_y^2 d\psi &= \int_{-\pi}^{\pi} \cos^2 \psi \sin^2 \psi d\psi = \frac{\pi}{4}, \\
\int_{-\pi}^{\pi} r_x^4 d\psi &= \int_{-\pi}^{\pi} \cos^4 \psi d\psi = \frac{3}{4}\pi, \\
\int_{-\pi}^{\pi} r_y^4 d\psi &= \int_{-\pi}^{\pi} \sin^4 \psi d\psi = \frac{3}{4}\pi.
\end{aligned}$$

The form of the pair-potential (A.1), after integrating over \mathbf{r}_{12} , is thus,

$$\begin{aligned}
U(\mathbf{a}_1, \mathbf{a}_2) &= \int_{-\pi}^{\pi} U_{eff}(\mathbf{a}_1, \mathbf{a}_2, \mathbf{r}_{12}) d\psi \\
&= 2\pi J_0 - 2\pi J_1 (\mathbf{a}_1 \cdot \mathbf{a}_2)^2 + 2\pi J_2 (\mathbf{a}_1 \cdot \mathbf{a}_2) (a_{1x}a_{2x} + a_{1y}a_{2y}) \\
&\quad - \frac{\pi}{4} J_3 (3a_{1x}^2 a_{2x}^2 + 3a_{1y}^2 a_{2y}^2 + a_{1x}^2 a_{2y}^2 + a_{1y}^2 a_{2x}^2 + 4a_{1x}a_{2x}a_{1y}a_{2y}) \\
&\quad - \pi J_{12}^2 (a_{1x}^2 + a_{1y}^2) - \pi J_{21}^2 (a_{2x}^2 + a_{2y}^2). \tag{A.2}
\end{aligned}$$

Now we expand the remaining brackets before writing the energy as a function of $(\phi_1, \phi_2, \theta_0)$. The remaining scalar products are

$$\begin{aligned}
(\mathbf{a}_1 \cdot \mathbf{a}_2)^2 &= a_{1x}^2 a_{2x}^2 + a_{1y}^2 a_{2y}^2 + a_{1z}^2 a_{2z}^2 + 2a_{1x}a_{2x}a_{1y}a_{2y} + 2a_{1x}a_{2x}a_{1z}a_{2z} \\
&\quad + 2a_{1y}a_{2y}a_{1z}a_{2z} \\
&= \cos^4 \theta_0 + \sin^4 \theta_0 \cos^2(\phi_1 - \phi_2) + \frac{1}{2} \tau_1 \tau_2 \sin^2 2\theta_0 \cos(\phi_1 - \phi_2), \\
(\mathbf{a}_1 \cdot \mathbf{a}_2) &= a_{1x}a_{2x} + a_{1y}a_{2y} + a_{1z}a_{2z} \\
&= \sin^2 \theta_0 \cos(\phi_1 - \phi_2) + \tau_1 \tau_2 \cos^2 \theta_0.
\end{aligned}$$

The J_2 term of (A.2) is

$$\begin{aligned}
(\mathbf{a}_1 \cdot \mathbf{a}_2) (a_{1x}a_{2x} + a_{1y}a_{2y}) &= (\mathbf{a}_1 \cdot \mathbf{a}_2) \sin^2 \theta (\cos \phi_1 \cos \phi_2 + \sin \phi_1 \sin \phi_2) \\
&= \sin^4 \theta_0 \cos^2(\phi_1 - \phi_2) + \frac{1}{4} \tau_1 \tau_2 \sin^2 2\theta_0 \cos(\phi_1 - \phi_2).
\end{aligned}$$

The J_3 term of (A.2) is

$$\begin{aligned}
&(3a_{1x}^2 a_{2x}^2 + 3a_{1y}^2 a_{2y}^2 + a_{1x}^2 a_{2y}^2 + a_{1y}^2 a_{2x}^2 + 4a_{1x}a_{2x}a_{1y}a_{2y}) \\
&= 3 \sin^4 \theta_0 \cos^2(\phi_1 - \phi_2) + \sin^4 \theta_0 \sin^2(\phi_1 - \phi_2).
\end{aligned}$$

The J_{12} and J_{21} terms of (A.2) are

$$(a_{ix}^2 + a_{iy}^2) = \sin^2 \theta_0 (\cos^2 \phi_i + \sin^2 \phi_i) = \sin^2 \theta_0.$$

We can now rewrite (A.2) in terms of $(\phi_1, \phi_2, \theta_0)$. We expand $\cos^2(\phi_1 - \phi_2)$ and collected like terms:

$$\begin{aligned} U(\mathbf{a}_1, \mathbf{a}_2) &= 2\pi J_0 - \pi J_1 + \pi J_2 - \frac{\pi}{2} J_3 - \pi (J_{12}^2 + J_{21}^2) \\ &\quad + \pi \cos^2 \theta_0 [2J_1 - 2J_2 + J_3 + (J_{12}^2 + J_{21}^2)] \\ &\quad + \frac{\pi}{2} \cos^4 \theta_0 [-6J_1 + 2J_2 - J_3] \\ &\quad + \frac{\pi}{2} \cos(\phi_1 - \phi_2) \sin^2 2\theta_0 \tau_1 \tau_2 [-2J_1 + J_2] \\ &\quad + \frac{\pi}{4} \cos 2(\phi_1 - \phi_2) \sin^4 \theta_0 [-4J_1 + 4J_2 - J_3]. \end{aligned} \quad (\text{A.3})$$

Defining the coefficients of the trigonometric functions as

$$\begin{aligned} b_0 &= \frac{\pi}{2} [4J_0 - 2J_1 + 2J_2 - J_3 - 2(J_{12}^2 + J_{21}^2)], \\ b_1 &= \pi [2J_1 - 2J_2 + J_3 + (J_{12}^2 + J_{21}^2)], \\ b_2 &= \frac{\pi}{2} [-6J_1 + 2J_2 - J_3], \\ b_3 &= \frac{\pi}{2} [-2J_1 + J_2], \\ b_4 &= \frac{\pi}{4} [-4J_1 + 4J_2 - J_3], \end{aligned} \quad (\text{A.4})$$

we can rewrite (A.3) as

$$\begin{aligned} U_{MS}(\mathbf{a}_1, \mathbf{a}_2) &= b_0 + b_1 \cos^2 \theta_0 + b_2 \cos^4 \theta_0 + b_3 \tau_1 \tau_2 \sin^2 2\theta_0 \cos(\phi_1 - \phi_2) \\ &\quad + b_4 \sin^4 \theta_0 \cos 2(\phi_1 - \phi_2). \end{aligned} \quad (\text{A.5})$$

References

- [1] F. Reinitzer. Contributions to the knowledge of cholesterol. *Liquid Crystals*, 5(1):7–18, 1989.
- [2] H. Kelker. History of liquid crystals. *Molecular Crystals and Liquid Crystals*, 21(1-2):1–48, 1973.
- [3] R.B. Meyer, L. Liebert, L. Strezelecki, and P. Keller. Ferroelectric liquid crystals. *Journal de Physique Lettres*, 36(3):L69–L71, 1975.
- [4] R.B. Meyer. Ferroelectric liquid crystals - Review. *Molecular Crystals and Liquid Crystals*, 40(1-4):33–48, 1977.
- [5] N.A. Clark and S.T. Lagerwall. Submicrosecond bistable electro-optic switching in liquid crystals. *Applied Physics Letters*, 36(11):899–901, 1980.
- [6] S. Garoff and R.B. Meyer. Electro-clinic effect at AC phase-change in a chiral smectic liquid crystal. *Physical Review Letters*, 38(15):848–851, 1977.
- [7] T.P. Rieker, N.A. Clark, G.S. Smith, D.S. Parmar, E.B. Sirota, and C.R. Safinya. Chevron local layer structure in surface-stabilized ferroelectric smectic C cells. *Physical Review Letters*, 59(23):2658–2661, 1987.
- [8] S. Diele, H. Sackmann, and P. Brand. X-ray-diffraction and polymorphism of smectic liquid crystals. *Molecular Crystals and Liquid Crystals*, 16(1-2):105, 1972.
- [9] A. de Vries, A. Ekachai, and N. Spielberg. Why the molecules are tilted in all smectic A phases, and how the layer thickness can be used to measure

- orientational disorder. *Molecular Crystals and Liquid Crystals*, 49(5):143–152, 1979.
- [10] A. de Vries. Experimental evidence concerning two different kinds of smectic C to smectic A transitions. *Molecular Crystals and Liquid Crystals*, 41(2): 27–31, 1977.
- [11] B.R. Ratna, R. Shashidhar, G.G. Nair, S.K. Prasad, C. Bahr, and G. Heppke. Evidence of a 1st-order smectic A-smectic C* transition and its approach to tricritical behavior. *Physical Review A*, 37(5):1824–1826, 1988.
- [12] F. Giesselmann, P. Zugenmaier, I. Dierking, S.T. Lagerwall, B. Stebler, M. Kaspar, V. Hamplova, and M. Glogarova. Smectic A*-smectic C* transition in a ferroelectric liquid crystal without smectic layer shrinkage. *Physical Review E*, 60(1):598–602, 1999.
- [13] Y.P. Panarin, V. Panov, O.E. Kalinovskaya, and J.K. Vij. Observation of a possible random ferroelectric liquid crystal phase. *Journal of Materials Chemistry*, 9(12):2967–2969, 1999.
- [14] M.D. Radcliffe, M.L. Brostrom, K.A. Epstein, A.G. Rappaport, B.N. Thomas, R.F. Shao, and N.A. Clark. Smectic A and C materials with novel director tilt and layer thickness behaviour. *Liquid Crystals*, 26(6):789–794, 1999.
- [15] M.S. Spector, P.A. Heiney, J. Naciri, B.T. Weslowski, D.B. Holt, and R. Shashidhar. Electroclinic liquid crystals with large induced tilt angle and small layer contraction. *Physical Review E*, 61(2):1579–1584, 2000.
- [16] A. de Vries. X-Ray photographic studies of liquid crystals: II. apparent

- molecular length and thickness in three phases of Ethyl-p-ethoxybenzal-p-aminobenzoate. *Molecular Crystals and Liquid Crystals*, 11:361–383, 1970.
- [17] A. de Vries. The description of the smectic A and C phases and the smectic AC phase transition of TCOOB with a diffuse-cone model. *J. Chem. Phys.*, 71:25–31, 1979.
- [18] A.J. Leadbetter and E.K. Norris. Distribution functions in 3 liquid crystals from x-ray-diffraction measurements. *Molecular Physics*, 38(3):669–686, 1979.
- [19] K. Saunders, D. Hernandez, S. Pearson, and J. Toner. Disorder to order: de Vries behavior from a Landau theory for smectic phases. *Physical Review Letters*, 98(19):197801–197804, 2007.
- [20] K. Saunders. de Vries behavior in smectic liquid crystals near a biaxiality-induced smectic A-smectic C tricritical point. *Physical Review E*, 77(6):061708–061720, 2008.
- [21] M.V. Gorkunov, F. Giesselmann, J.P.F. Lagerwall, T.J. Sluckin, and M.A. Osipov. Molecular model for de Vries type smectic A-smectic C phase transition in liquid crystals. *Physical Review E*, 75(6):060701–060704, 2007.
- [22] M.V. Gorkunov, M.A. Osipov, J.P.F. Lagerwall, and F. Giesselmann. Order-disorder molecular model of the smectic A-smectic C phase transition in materials with conventional and anomalously weak layer contraction. *Physical Review E*, 76(5):051706–051721, 2007.
- [23] M.A. Osipov and M.V. Gorkunov. Ferroelectric ordering in chiral smectic C* liquid crystals determined by nonchiral intermolecular interactions. *Physical Review E*, 77(3):031701–031713, 2008.

-
- [24] M.A. Osipov, M.V. Gorkunov, H.F. Gleeson, and S. Jaradat. Molecular models for ferroelectric liquid crystals with conventional and anomalously weak layer contraction. *European Physical Journal E*, 26(4):395–404, 2008.
- [25] M.V. Gorkunov and M.A. Osipov. Molecular models for the smectic A-smectic C phase transition in a system of biaxial molecules. *Journal of Physics A-Mathematical and Theoretical*, 41(29):295001, 2008.
- [26] M.V. Gorkunov and M.A. Osipov. Molecular theory of layer contraction in smectic liquid crystals. *Journal of Physics-Condensed Matter*, 20(46):465101, 2008.
- [27] A.V. Emelyanenko, A. Fukuda, and J.K. Vij. Theory of the intermediate tilted smectic phases and their helical rotation. *Physical Review E*, 74(1):011705, 2006.
- [28] A.V. Emelyanenko. Molecular-statistical approach to a behavior of ferroelectric, antiferroelectric and ferrielectric smectic phases in the electric field. *European Physical Journal E*, 28(4):441–455, 2009.
- [29] G.R. Luckhurst. The Gay-Berne mesogen: a paradigm shift? *Liquid Crystals*, 33(11-12):1389–1395, 2006.
- [30] L.F. Rull. Phase diagram of a liquid crystal model- a computer-simulation study. *Physica A*, 220(1-2):113–138, 1995.
- [31] C. Zannoni. Molecular design and computer simulations of novel mesophases. *Journal of Materials Chemistry*, 11(11):2637–2646, 2001.
- [32] J.E. Lennard-Jones. Cohesion. *Proceedings of the Physical Society*, 43(5):461, 1931.

- [33] B.J. Berne and P. Pechukas. Gaussian model potentials for molecular-interactions. *Journal of Chemical Physics*, 56(8):4213, 1972.
- [34] J.G. Gay and B.J. Berne. Modification of the overlap potential to mimic a linear site-site potential. *Journal of Chemical Physics*, 74(6):3316–3319, 1981.
- [35] A.J. Stone. *The molecular physics of liquid crystals*, chapter 2. Academic Press: New York, 1979.
- [36] M.A. Bates and G.R. Luckhurst. Computer simulation studies of anisotropic systems. XXX. The phase behavior and structure of a Gay-Berne mesogen. *Journal of Chemical Physics*, 110(14):7087–7108, 1999.
- [37] D.J. Adams, G.R. Luckhurst, and R.W. Phippen. Computer-simulation studies of anisotropic systems.17. The Gay-Berne model nematogen. *Molecular Physics*, 61(6):1575–1580, 1987.
- [38] G.R. Luckhurst, R.A. Stephens, and R.W. Phippen. Computer-simulation studies of anisotropic systems .19. Mesophases formed by the Gay-Berne model mesogen. *Liquid Crystals*, 8(4):451–464, 1990.
- [39] W. Maier and A. Saupe. Eine einfache molekulare theorie des nematischen kristallinflussigen zustandes. *Z. Naturforsch A*, 13:564, 1958.
- [40] W. Maier and A. Saupe. Eine einfache molekular-statistische theorie der nematischen kristallinflussigen phase .1. *Z. Naturforsch A*, 14:882, 1959.
- [41] W. Maier and A. Saupe. Eine einfache molekular-statistische theorie der nematischen kristallinflussigen phase .2. *Z. Naturforsch A*, 15:287, 1960.
- [42] B.W. Van der Meer and G. Vertogen. Molecular theory of the chiral smectic C phase. *Physics Letters A*, 74(3-4):239–241, 1979.

- [43] B.W. Van der Meer. *Molecular models for cholesteric and smectic liquid crystals. Ph.D thesis.* University of Groningen, 1979.
- [44] D. Demus, J. Goodby, G. W. Gray, H.-W. Spiess, and V. Vill. *Molecular Theories of Liquid Crystals*, pages 40–71. Wiley-VCH Verlag GmbH, 2008.
- [45] N.A. Clark, T. Bellini, R.F. Shao, D. Coleman, S. Bardon, D.R. Link, J.E. Maclennan, X.H. Chen, M.D. Wand, D.M. Walba, P. Rudquist, and S.T. Lagerwall. Electro-optic characteristics of de Vries tilted smectic liquid crystals: Analog behavior in the smectic A* and smectic C* phases. *Applied Physics Letters*, 80(22):4097–4099, 2002.
- [46] P.G. de Gennes and J. Prost. *The Physics of liquid crystals (international series of monographs on physics)*. Oxford University Press, USA, 1995.
- [47] J.W. Goodby, R. Blinc, N.A. Clark, S.T. Lagerwall, M.A. Osipov, S.A. Pikin, T. Sakurai, K. Yoshino, B. Zeks, R.A. Stephens, and R.W. Phippen. *Ferroelectric liquid crystals: principles, properties and applications*. Gordon and Breach Science Publishers, 1991.
- [48] T.F. Coleman and Y.Y. Li. An interior trust region approach for nonlinear minimization subject to bounds. *SIAM Journal on Optimization*, 6(2):418–445, 1996.
- [49] N.J. Mottram and S.J. Elston. Order Parameter Theory for Switching in Antiferroelectric Liquid Crystals. *Molecular Crystals and Liquid Crystals*, 330:557–564, 1999.
- [50] E. Hairer, S.P. Nørsett, and G. Wanner. *Solving ordinary differential equations*. Springer, 1999. 167-168 pp.

-
- [51] S.T. Lagerwall. *Ferroelectric and antiferroelectric liquid crystals*. Wiley-VCH, 1999.
- [52] M.A. Osipov, T.J. Sluckin, and E.M. Terentjev. Viscosity coefficients of smectics-C. *Liquid Crystals*, 19(2):197–205, 1995.